SUB-METRE POSITIONING WITH SMARTPHONE GLOBAL NAVIGATION SATELLITE SYSTEM MEASUREMENTS IN USER ENVIRONMENTS

JIAHUAN HU

A DISSERTATION SUBMITTED TO THE FACULTY OF GRADUATE STUDIES IN PARTIAL FULFILLMENT OF THE REQUIREMENTS FOR THE DEGREE OF DOCTOR OF PHILOSOPHY

GRADUATE PROGRAMME IN EARTH AND SPACE SCIENCE
YORK UNIVERSITY

TORONTO, ONTARIO

AUGUST 2024

ABSTRACT

The ubiquity of smartphones catalyzes various smartphone-based Internet of Things (IoT) applications, among which smartphone positioning that uses Global Navigation Satellite System (GNSS) observations to provide user position plays an important role. The noisy smartphone GNSS measurements from signal obstructed environments and embedded antennas prevent users from obtaining reliable and accurate positioning solutions. With a correct understanding of the measurement characteristics and advanced positioning techniques such as Real-Time Kinematic (RTK), Precise Point Positioning (PPP), and PPP-RTK, this dissertation aims to achieve sub-metre- or decimetre-level positioning accuracy with smartphone GNSS measurements in realistic environments. In this dissertation, a novel smartphone range error derivation method is proposed, as well as an improved cycle slip (CS) detection method. New stochastic modelling and measurement outlier detection methods are developed. And smartphone ambiguity resolution (AR) is conducted with a newly proposed candidate selecting strategy.

Smartphone measurements exhibit significantly higher noise levels as compared to those from geodetic hardware, in which the range errors are more correlated with the carrier-to-noise density ratio (C/N_0). Moreover, range errors are environment-dependent, and they behave differently when, e.g., the smartphone is mounted on the vehicle roof versus the dashboard. Considering that the conventional Doppler CS detection method is sometimes not applicable due to inconsistent time-differenced carrier phase (TDCP) and Doppler clocks, a novel modified Doppler method is proposed and validated with simulated cycle slips. With proposed Doppler cycle slip detection method, all simulated cycle slip combinations are detected. In terms of quality control methods, the improved stochastic model and novel outlier detection method outperform the conventional C/N_0-based weighting and a fixed residual rejection threshold, showing a percentage improvement from 38% to 54% for PPP horizontal positioning errors within 1 metre. A novel smartphone RTK wide-lane (WL) partial AR strategy is proposed, for which the static results show an improvement of 83% in horizontal when WL AR is conducted compared to the underlying float solution, and the positioning accuracies can reach 6.8, 2.9, and 11.5 cm in E, N, and U, respectively. The proposed algorithm is validated with kinematic datasets collected in real-life environments, in which the time series of horizontal positioning errors exhibit less variation than the float solutions, represented by smaller positioning errors. Moreover, with fixing WL ambiguities, the horizontal positioning performance has improvements ranging from several centimetres to up to 8 decimetres depending on the related environments. the biggest improvement of 0.79 m is noticed for 95th percentile horizontal positioning errors under suburban environments. Improvements on the above-mentioned aspects show potential on achieving decimetre-level positioning performance with smartphone embedded antennas in realistic environments.

Improvements on the above-mentioned aspects show potential on achieving decimetre-level positioning performance with smartphone embedded antennas in realistic environments. Further research work based on this dissertation is recommended, including in-depth signal characterization, cycle slip detection combination and further optimization, environment-related stochastic modelling, and ambiguity resolution optimization.

Keywords: Global Positioning System, Precise Point Positioning, Real-Time Kinematic, smartphone positioning, suburban navigation, range errors, cycle slip, quality control, ambiguity resolution

DEDICATION

To

Mom and Dad

ACKNOWLEDGEMENTS

I always remember the first time I met with Professor Sunil Bisnath when he visited Wuhan in 2019. It was my pleasure to be his tour guide, and we talked a lot about life and research in Toronto. I am very grateful that Professor Sunil Bisnath gave me the opportunity to pursue my Ph.D. degree at York University. Not only his patience, rigorousness, and diligence in research, but also kindness and humour in daily life deeply impressed me, and I believe I will benefit from him for the rest of my life.

I would also like to thank Dr. Jianguo Wang and Dr. Garrett Seepersad for being my supervisor committee members. Their research comments and suggestions have been really helpful, and without these suggestions, I would have been able to finish my dissertation.

In addition, I want to express my gratitude to the members in York GNSS Lab. Life with them has provided me with different views from different cultures, and research discussions have helped me to improve my contributions. Thanks for Sudha, Nacer, Anurag, Ding, Sihan, Soroush, Sandesh, Pragati, Ben, Sogand, and Narin, I will always miss you all.

Moreover, I also express my appreciation to Professor Xiaohong Zhang and Dr. Pan Li for their insightful suggestions they have given about life and research. Also, many thanks to my friends and colleagues for discussions about research ideas and potential solutions.

My warm gratitude also goes to my family who give me the confidence to continue my academic path. Without their strong support, I would not be able to be where I am now. Whenever I felt life is hard, their voices are there to encourage me.

TABLE OF CONTENTS

LIST OF TABLES

LIST OF FIGURES

LIST OF ACRONYMS

AC	Analysis Centre
AI	Artificial Intelligence
APC	Antenna Phase Centre
AR	Ambiguity Resolution
BDS	BeiDou Satellite Navigation System
BIE	Best Integer Equivariant
CDF	Cumulative Distribution Function
CS	Cycle Slip
CMP	Code-Minus-Phase
CMN	Code Multipath and Noise
C/N_0	Carrier-to-Noise Density Ratio
CoM	Centre of Mass
DCB	Differential Code Bias
DD	Double-Differencing
ECEF	Earth-Centred-Earth-Fixed
EKF	Extended Kalman Filter
GF	Geometry-Free
GNSS	Global Navigation Satellite System
GSDC	Google Smartphone Decimetre Challenge
IE	Inertial Explore
IF	Ionospheric-Free
IGS	International GNSS Service

IMU	Inertial Measurement Unit
IPB	Initial Phase Bias
LAMBDA	Least-squares AMBiguity Decorrelation Adjustment
LBS	Location-Based Service
LOS	Line-Of-Sight
LS	Least Squares
MGEX	Multi-GNSS Experiment
MOFC	Modified Optimal Fitting Coefficient
MW	Melbourne-Wübbena
NL	Narrow-Lane
NLOS	Non-Line-Of-Sight
MF	Mapping Function
OMC	Observation-Minus-Calculation
PAR	Partial Ambiguity Resolution
PC	Personal Computer
PCE	Precise Clock Estimation
PCO	Phase Centre Offset
PCV	Phase Centre Variation
PNT	Positioning, Navigation, and Timing
POD	Precise Orbit Determination
PPK	Post-Processed Kinematic
PPP	Precise Point Positioning
PVA	Position, Velocity, and Acceleration
QC	Quality Control

RF	Radio Frequency
RINEX	Receiver Independent Exchange Format
RMS	Root Mean Square
RTK	Real-Time Kinematic
SD	Single-Differencing
SLS	Sequential Least Squares
SNR	Signal-to-Noise Ratio
SoD	Second of the Day
SPP	Standard Point Positioning
SR	Success Rate
Std Dev	Standard Derivation
STEC	Slant Total Electron Content
TD	Time-Differencing
TDCP	Time-Differenced Carrier Phase
TTFF	Time To First Fix
UAV	Unmanned Aerial Vehicle
UDUC	Un-Differenced and Un-Combined
WL	Wide-Lane
ZHD	Zenith Hydrostatic Delay
ZWD	Zenith Wet Delay

1 INTRODUCTION

The construction and modernization of Global Navigation Satellite Systems (GNSSs), as well as ground- and satellite-based augmentation systems, have enabled worldwide positioning, navigation, and timing (PNT) services. Since the 1980s, GNSS-based positioning technologies have attracted lots of attentions in both military fields and civilian applications. Depending on various user demands, GNSS is capable of providing ten metre-level to millimetre-level positioning performance with different grades of receivers and processing. For instance, geodetic-grade receivers are typically used in applications such as deformation monitoring, time transferring, and atmospheric science, in which high-quality GNSS measurements are required for further data processing. However, for applications such as unmanned aerial vehicles (UAVs), self-driving cars, and water transportation, low-cost receivers satisfy most user cases despite the relatively noisier GNSS measurements compared to geodetic receivers. Smartphones, being one of the most ubiquitous devices in daily life, have the capability to receiver GNSS signals, thereby enabling them to provide location-based services (LBSs) for mass-market users. Hence, this dissertation concentrates on making use of smartphone GNSS measurements to provide precise positioning performances in actual user environments -rather than in simulated or benign test environments. To be specific, not only positioning performance under open sky environments are evaluated, but also regions such as vegetated areas, overpasses, and suburban environments are included.

1.1 Overview of smartphone GNSS positioning

A new era of smartphone GNSS positioning began with Google's release of the Android 7.0 operating system in 2016 (Malkos 2016), from which users gained access to raw GNSS observations received by smartphones. Since then, the ubiquity of smartphones has catalyzed the development of mass-market location-based applications, including pedestrian positioning and vehicle navigation. However, noisy smartphone GNSS measurements are a significant limitation in obtaining satisfactory positioning results, especially in suburban and urban areas. Therefore, research has been conducted in areas of smartphone

GNSS measurement quality assessment, positioning performance evaluation, stochastic modelling, and quality control optimization.

Smartphones use linearly polarized antennas which produce noisy and multipath-proned GNSS measurements, posing a challenge to incorporate these measurements in data processing. Since 2016, there have been numerous investigations into smartphone GNSS measurement quality. Compared to decimetre-level pseudorange observation noise and millimetre-level carrier phase measurement precisions in a geodetic receiver, smartphone measurements are approximately ten times noisier. Robustelli et al. (2019) found that code multipath errors for a Xiaomi Mi8 phone are estimated to be around 6 m and 2 m for GPS L1 and L5 signals, respectively, in open sky areas. In obstructed environments, Liu et al. (2019) found that the pseudorange noise can reach tens of metres, and the a posteriori code residuals are reported to be more than 5 m in urban canyon environments with PPP. Moreover, GLONASS code residuals are significantly larger than those of GPS, Galileo, and BeiDou Satellite Navigation System (BDS) (Seepersad et al. 2021). The noisy pseudorange measurements lead to ten-metre-level positioning accuracy with Standard Point Positioning (SPP) using code observations (Sikirica et al. 2017; Paziewski et al. 2020).

With advanced precise positioning techniques which include carrier phase measurements in data processing, e.g., Real-Time Kinematic (RTK), Precise Point Positioning (PPP), and PPP-RTK, smartphone positioning performance is reported to be capable of achieving sub-metre level in open sky areas and metre-level in realistic environments (Miao et al. 2022; Tao et al. 2023). RTK makes use of observations from a reference station to eliminate most of the common errors, and the position vector between the user and reference station is estimated. In contrast, PPP uses precise satellite clock and orbit products generated by, e.g., International GNSS Service (IGS) analysis centres (ACs), and well-modelled error source corrections, to obtain the user position with a single receiver. Combining PPP and RTK techniques, PPP-RTK aims to provide the user with RTK-quality solutions through PPP processing, in which regional atmospheric corrections are applied to enhance the solution. The detailed introduction of these three methods will be provided in Chapter 2.

Early research focused on smartphone positioning under optimal environments. In a static short baseline experiment, Realini et al. (2017) reported decimetre-level accuracy with smartphone RTK, and Laurichesse et al. (2017) achieved sub-metre-level performance with a Samsung S8 phone. Similarly, smartphone PPP can also reach sub-metre-level accuracy in static environments after convergence (Wu et al. 2019; Wang et al. 2021). However, smartphones in mass-market applications are usually under complex environments, in which GNSS measurements suffer frequent cycle slips (CS), severe multipath, and frequent signal loss.

With the Google Smartphone Decimetre Challenge (GSDC) competition launched since 2021, users get access to large sets of open-sourced automotive-based smartphone GNSS datasets, indicating that smartphone precise positioning in challenging conditions is attracting attention from both academic and industrial communities. Seepersad et al. (2021) found that the cross-track errors were less than 3 m for 55%, 94%, and 35% of the datasets mainly collected under highway, vegetation, and urban canyon environments, respectively. Moreover, with a Xiaomi Mi8 phone under realistic environment, the 95th percentile horizontal errors were 3.2 m and 2.4 m with RTK and PPP, respectively (Seepersad et al. 2022). When applying ionospheric constraints, a 57% improvement in horizontal root mean square positioning accuracy is observed in the first 20 minutes of data collection (Yi et al. 2021). With processing Google smartphone datasets, Everett et al. (2022) obtained the 95th horizontal positioning accuracies of 2.2 m, 4.5 m, and 24.1 m for datasets under highway, street, and urban canyon, respectively. Despite the significant progress made in smartphone GNSS positioning, the current performance, especially when under obstructed environments, cannot satisfy user applications such as vehicle navigation, in which a higher positioning performance (e.g., sub-metre or decimetre-level under suburban environments) is required.

1.2 Problem statement

To further improve smartphone positioning performance, key aspects such as pre-fit (aka pre-processed measurement misclosure) and post-fit quality control (QC), cycle slip detection, missing measurements, stochastic modelling, optimal estimation, and carrier phase ambiguity resolution (AR), need to be further addressed and optimized (Bisnath and Aggrey, 2024). To be specific, the following research topics and questions require more investigation, as shown in Figure 1.1, as well as the following research topics 1-4.

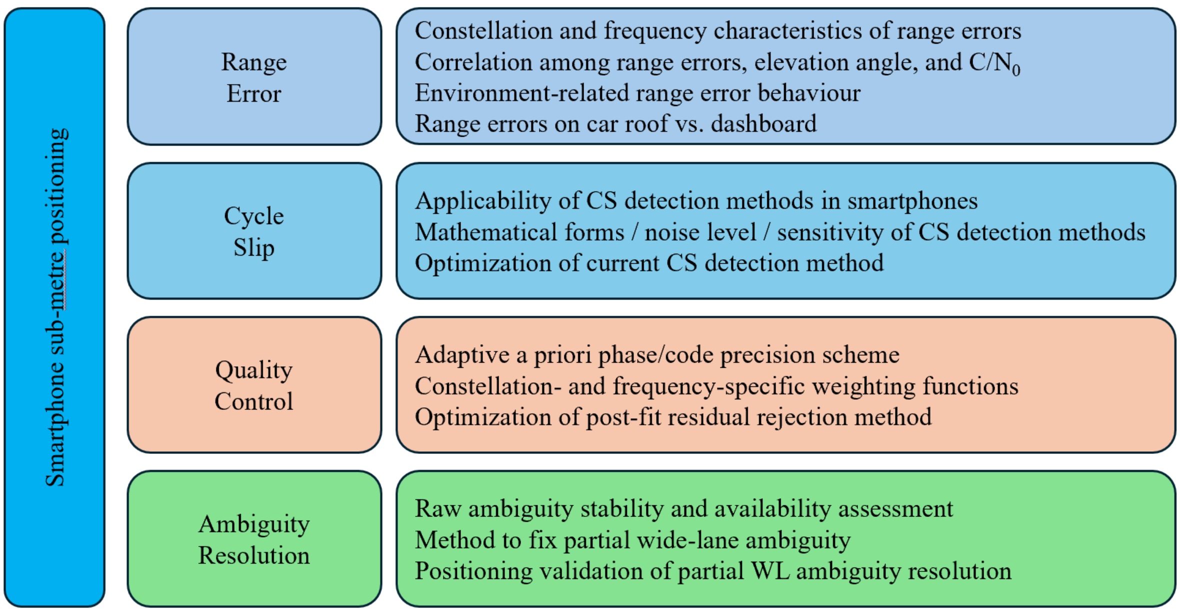

Figure 1.1 Illustration of research topics in this dissertation which contains range error, cycle slip, quality control, and ambiguity resolution.

Research Topic 1: Comprehensive assessment of smartphone range errors in realistic environments. Existing research usually extracts GNSS multipath (Hauschild et al. 2012; Zheng et al. 2019) or forms zero-baseline measurements to extract the smartphone residuals to further indicate measurement quality. However, these methods are not applicable in realistic environments where smartphones are moving, using poor quality signals, being blocked by the environment and are frequently missing GNSS measurements. Therefore, the key research questions are:

(1) How does the smartphone range error distribution behave on different signal frequencies and constellations?

(2) Is there any correlation between range errors and satellite elevation angles, and are range errors and SNR values correlated?

(3) How does range error vary under different multipath profiles in real driving environments? Do any differences exist among different mounting locations?

(4) Is there any correlation between smartphone pre-fit residuals and range errors? And are the correlations on P1 and P5 similar?

Research Topic 2: Smartphone cycle slip detection improvement. There are several commonly used pre-processing cycle slip detection methods, which include, the Melbourne-Wübbena (MW) combination, the geometry-free (GF) combination, code-minus-phase (CMP) measurement, and the Doppler cycle slip detection method. Whether they are applicable and how these methods perform in smartphone data processing need to be assessed. The key research questions are:

(1) Are commonly used cycle slip detection methods applicable to smartphones? And what are the mathematical forms of their test values (to compare with the noise level and determine the thresholds of different cycle slip detection methods)?

(2) What are the noise levels of different cycle slip detection methods? How sensitive they are for smartphone measurements?

(3) If existing cycle slip detection methods are not applicable, what is the solution, and how does the improved method perform?

Research Topic 3: Smartphone GNSS stochastic modelling and residual rejection optimization. Most of existing QC work focuses on improving the weighting scheme functions, in which the most commonly used is carrier-to-noise density ratio (C/N_0)-based weighting. However, the conventional weighting function may not reflect the true correlation between the range errors and signal-to-noise ratio (SNR) values under realistic user environments. Moreover, how does the precision ratio between code and phase measurements affect the results has not been evaluated in the literature. For outlier detection, in existing literature, hypothesis testing is usually employed, and outliers are usually detected using a fixed threshold. Besides, the investigation of a posteriori residual rejection has not been detailed discussed in smartphones in the literature. Considering the above aspects, the key research questions are:

(1) How does the measurement precision ratio between carrier phase and pseudorange affect the solution?

(2) Whether the weighting scheme based on range errors perform better than conventional SNR-based weighting scheme, and what is the corresponding improvement?

(3) How does post-fit residual rejection contribute to the solution? Is a fixed rejection threshold value better than an adaptive threshold?

Research Topic 4: Smartphone ambiguity resolution. Recovering the integer property of ambiguities in phase measurements has been a challenge in smartphones due to the noisy measurements. It is reported that, with external antenna and open-sky environments, smartphone phase ambiguities can be fixed to integers. But what is the ambiguity characteristic and whether it is possible to be fixed with embedded antennas in a realistic environment needs more investigation. The key research questions are:

(1) Whether the dual- or single-frequency phase measurements are available, and how do the time series of estimated raw ambiguities vary in realistic driving environments? Do they vary with different positioning methods?

(2) Are the raw ambiguity estimates stable enough to be fixed? And if the raw ambiguities are hard to be fixed, what about the wide-lane (WL) ambiguities?

(3) What ambiguity resolution methods are more suitable in fixing smartphone ambiguities? Are there differences in AR strategies for smartphones compared to geodetic-grade receivers?

(4) How accurate are the solutions when fixing ambiguities compared to float solutions?

1.3 Dissertation motivation

The demands for low-cost LBS services in mass-market applications catalyzes the development of smartphone precise positioning technologies. Incorporating smartphone GNSS measurements allows users to obtain spatial information, while it also raises the difficulty in dealing with the noisy measurements. Considering the location-based-service demand for mass-market smartphone users, the motivation of this dissertation is to enhance smartphone GNSS solutions to sub-metre or decimetre-level horizontal positioning accuracy in realistic environments by improving quality control methods and conducting ambiguity resolution with embedded smartphone antennas. The premise of reaching this goal is to obtain comprehensive knowledge of the smartphone measurement characteristics. With sub-metre to decimetre-level positioning performance, this dissertation breaks the barrier in smartphone applications for lane-level navigation. Moreover, the proposed algorithms may also potentially benefit the low-cost GNSS fields such as UAV and self-driving cars.

1.4 Contributions and significance

The effort of this research is to achieve sub-metre to decimetre-level GNSS positioning accuracy with embedded smartphone antennas, which not only depends on the understanding of smartphone range errors, but also relies on the improvement of quality control methods and realization of ambiguity resolution. By addressing the research questions proposed in Section 1.2, the contributions of this research are as follows:

(1) Comprehensive analysis of smartphone range errors under realistic environments, with assessment of range error characteristics and the correlations with SNR, elevation angle, and pre-fit residuals.

(2) Performance evaluation of different cycle slip detection methods, including MW combination, GF combination, CMP method, and Doppler cycle slip detection method, on smartphone GNSS data processing. Special modification on Doppler cycle slip detection method is proposed and validated.

(3) PPP performance comparison between conventional C/N_0-based weighting scheme and proposed range error-based weighting scheme. Validation of a new a posteriori residual rejection method which considers the range error distribution and rejected number of measurements.

(4) Assessment of availability and stability of raw ambiguities estimated by PPP, RTK, and PPP-RTK. Positioning performance comparison with RTK WL partial ambiguity resolution (PAR) and float solution.

Amongst all of these contributions, the novelties of this research are:

(1) Different from existing literature which use zero-baseline or positioning post-fit residuals to extract smartphone measurement noise, this research proposes to derive actual range errors with a nearby geodetic receiver and pre-measured lever-arm correction. The range errors under different environments and comparison of range errors when smartphones are mounted on car dashboard and roof are for the first time carried out.

(2) A new Doppler cycle slip detection method is proposed to deal with the inconsistent carrier phase and Doppler receiver clock drifts for a Xiaomi Mi8 phone GNSS measurements, prior to which the conventional Doppler cycle slip detection method was not applicable for such chipsets.

(3) A novel stochastic model is proposed, which is a combination of a priori code/phase precision ratio and measurement weighting function. The over-optimistic issue with GPS L5 and Galileo E5a is specifically discussed, to be specific, the weights on these two frequencies are too optimal compared to L1 measurements. Moreover, a new outlier diagnosis method is proposed, in which an adaptive residual rejection threshold function is formulized.

(4) For the first time, smartphone RTK wide-lane partial ambiguity resolution strategy is proposed and validated with both static and kinematic datasets.

Peer-reviewed portions of the research in this dissertation have been submitted or published as journal and conference proceedings publications. The first-authored publications/submissions are:

(1) Hu J, Li P, Feng J, Zhou F, Yi D, Bisnath S (2024) Enhancing smartphone relative positioning with partial wide-lane ambiguity resolution: path to real-time, decimetre-level positioning in user environments. (*submitted to IEEE Internet of Things Journal*)

(2) Hu J, Li P, Bisnath S (2024) Enhancing smartphone precise point positioning to sub-meter accuracy in suburban environments: a new stochastic model and outlier diagnosis. *GPS Solutions*, 28, 112.

(3) Hu J (2024) Why some cycle slip detection methods do not work for smartphones: Investigation, explanation and solutions. (*ION GNSS+ 2024 student award winner*)

(4) Hu J, Bisnath S (2023) Preliminary Assessment of Improved Smartphone GNSS Quality Control Methods Based on Range Errors. *Proc. ION GNSS 2023*, Institute of Navigation, Denver, Colorado, USA, 11-15 Sept, 85-98.

(5) Hu J, Li P, Bisnath S (2023) Towards GNSS Ambiguity Resolution for Smartphones in Realistic Environments: Characterization of Smartphone Ambiguities with RTK, PPP, and

PPP-RTK. *Proc. ION GNSS 2023*, Institute of Navigation, Denver, Colorado, USA, 11-15 Sept, 2698-2711.

(6) Hu J, Yi D, Bisnath S (2023) A Comprehensive Analysis of Smartphone GNSS Range Errors in Realistic Environments. *Sensors*, 23(3), 1631.

(7) Hu J, Cui B, Li P, Bisnath S, Zheng K (2023) Exploring the Role of PPP-RTK Network Configuration: A Balance of Server Budget and User Performance. *GPS Solutions*, 27, 184.

Additionally, co-authored or related publications are:

(1) Yi D, Hu J, Bisnath S (2024) Improving PPP smartphone processing with adaptive quality control method in obstructed environments when carrier-phase measurements are missing. *GPS Solutions*, 28, 56. https://doi.org/10.1007/s10291-023-01596-1.

(2) Hu J, Li P, Zhang X, Bisnath S, Pan L (2022) Precise point positioning with BDS-2 and BDS-3 constellations: Ambiguity resolution and positioning comparison. *Advances in Space Research*, 70(7), 1830-1846.

(3) Li P, Cui B, Hu J, Liu X, Zhang X, Ge M, Schuh H (2022) PPP-RTK considering the ionosphere uncertainty with cross-validation. *Satellite navigation*, 3(1), 1-13.

(4) Seepersad G, Hu J, Yang S, Yi D, Bisnath S (2022) Performance Assessment of Tightly Coupled Smartphone Sensors with Legacy and State Space Corrections. *Proc. ION GNSS 2022*, Institute of Navigation, Denver, Colorado, USA, 19-23 Sept, pp 2235-2255.

(5) Seepersad G, Hu J, Yang S, Yi D, Bisnath S (2021) Changing Lanes with Smartphones Technology. *Proc. ION GNSS 2021*, Institute of Navigation, St. Louis, Missouri, USA, 20-24 Sept, pp 3021-3036.

1.5 Dissertation outline

Chapter 2 starts with the introduction of mathematical models for RTK, PPP, and PPP-RTK, respectively. Then, the key parameter processing strategies are discussed and summarized, which include satellite orbit and clock, ionospheric and tropospheric refractions, receiver coordinates and clocks, as well as ambiguity parameters. Basic principles of three estimators are briefly described, which are least squares (LS), sequential least squares (SLS), and extended Kalman filter (EKF).

Chapter 3 concentrates on smartphone range errors. The derivation of range errors with consideration of lever arm is detailed formulated. With datasets collected in and around York University, the smartphone range errors are comprehensively assessed and compared with geodetic receivers. Frequency and constellation-specific range errors are analyzed, followed by the correlation assessment among range errors, SNR values, and elevation angles. Range error characteristics under various environments are evaluated, followed by a comparison of range errors derived from smartphones mounted on a car dashboard and car roof.

Chapter 4 focuses on evaluation and validation of proposed smartphone cycle slip detection method. Four conventional cycle slip detection methods are first introduced in detail, including MW combination, GF combination, CMP method, as well as Doppler cycle slip detection method. With the mathematical forms of different methods, the sensitivity of the four methods is analyzed principally. Considering the inconsistency between phase clock and Doppler clock drift, a new cycle slip detection method is proposed, in which the test values are treated as a mean shift model that follows normal distribution, with median constellation and frequency-specific test values the means of the Gaussian distribution. Ten sets of simulated cycle slips are used to assess different cycle slip detection methods and validate the proposed method.

Chapter 5 is constituted of a novel stochastic model and a new outlier diagnosis method. The effect of phase/code precision ratio on positioning performance is analyzed, motivated in the proposed adaptive a priori phase/code precision ratio. Based on the range errors derived in Chapter 3, a new weighting scheme function is built, with specially consideration of an over-optimistic issue on fitted functions of GPS L5 and Galileo E5a. A new residual rejection method is proposed to identify measurement outliers, considering both SNR and the number of rejected measurements. Moreover, the proposed algorithms are validated and assessed with datasets collected in suburban environments.

Chapter 6 is the most challenging part of this dissertation, as it conducts smartphone ambiguity resolution with embedded antenna. The availability and stability of raw ambiguities are assessed, which further indicates that fixing WL ambiguities would be more realistic in smartphones. Therefore, the detailed methods of deriving WL ambiguities are described, followed by the introduction of three ambiguity resolution methods: rounding, the least-squares ambiguity decorrelation adjustment (LAMBDA), and best integer equivariant (BIE). The PAR strategy is introduced in detail, and a novel state updating strategy is proposed. With both static and kinematic datasets, smartphone RTK WL PAR is conducted, and the positioning results are analyzed and compared with float solutions.

Chapter 7 provides summary of the dissertation work and recommendations for future research. Based on the works in this dissertation, extended works, e.g., in-depth signal characterization, cycle slip detection combination and further optimization, environment-related stochastic modelling, and ambiguity resolution optimization, can be conducted in future research.

2 GNSS PRECISE POSITIONING TECHNIQUES AND MAJOR ERROR SOURCES

Depending on using different types of measurements, GNSS-based smartphone positioning can reach ten-metre-level positioning accuracy with pseudorange measurements, and metre-level positioning performance when including carrier phase measurements. The motivation of this dissertation is to achieve high-accuracy positioning performance with smartphone GNSS measurements. Therefore, precise positioning methods with carrier phase measurements are introduced, which are RTK, PPP, and PPP-RTK. All of these methods utilize both pseudorange and carrier phase measurements to estimate user position. The difference among these three methods is in the way of dealing the error sources. Hence, this chapter starts with the introduction of mathematic model of RTK, PPP, and PPP-RTK, followed by the summary of processing strategies of different error sources, including satellite clock and orbit, atmospheric refractions, receiver coordinates and clock, and ambiguity. Furthermore, a brief description of three commonly used filters is provided, which are least squares, sequential least squares, and the extended Kalman filter.

2.1 GNSS Precise Positioning mathematic models

The raw GNSS measurements of satellite s on frequency j can be given as Equation (2.1).

$$\begin{cases} P_j^s = \rho^s + c(dt_r - dt^s) + \gamma_j I_1^s + T^s + b_j^s + b_{r,j} + \varepsilon_j^s \\ L_j^s = \rho^s + c(dt_r - dt^s) - \gamma_j I_1^s + T^s + \lambda_j (N_j^s + B_j^s + B_{r,j}) + \xi_j^s \end{cases} \tag{2.1}$$

where P and L are pseudorange and carrier phase measurements in units of metres, respectively. ρ is geometrical range from satellite to receiver. c is the speed of light, dt_r is receiver clock offset at time of arrival, and dt^s is satellite clock offset at time of transmission. γ_j is the ionospheric frequency coefficient on the *j*th frequency, and $\gamma_j = f_j / f_1$, where f denotes the frequency. I_1^s is the slant ionospheric effect on the first frequency, and T^s refers the slant tropospheric delay. λ_j is the wavelength, and N_j^s is the integer ambiguity. b_j^s, $b_{r,j}$, B_j^s, and $B_{r,j}$ are code and phase hardware biases for satellite and receiver, respectively. ε_j^s and ξ_j^s are code and phase observation noise coupled with multipath and unmodelled errors.

2.1.1 Relative Kinematic Positioning

When there is a nearby base station close to users, GNSS observations from base station can be used to form double-differenced equations. For user station r and base station b, the between-receiver differenced measurements can be formulated as Equation (2.3).

$$\begin{cases} \nabla P_{br,j}^s = \nabla \rho_{br}^s + c\nabla dt_{br} + \gamma_j \nabla I_{br,1}^s + \nabla T_{br}^s + b_{br,j} + \nabla \varepsilon_{br,j}^s \\ \nabla L_{br,j}^s = \nabla \rho_{br}^s + c\nabla dt_{br} - \gamma_j \nabla I_{br,1}^s + \nabla T_{br}^s + \lambda_j (\nabla N_{br,j}^s + \nabla B_{br,j}) + \nabla \xi_{br,j}^s \end{cases} \tag{2.3}$$

where ∇ is between-receiver differencing operator ($\nabla(\bullet)_{br} = (\bullet)_b - (\bullet)_r$). With between-receiver differencing, the satellite clock offset and satellite-related hardware delays are eliminated. Moreover, the satellite orbit offset and atmospheric refractions are mitigated due to the spatial correlation. When choosing a reference satellite k from the same constellation, based on Equation (2.3), a further between-satellite between-receiver double-differenced measurement can be obtained, as:

$$\begin{cases} \nabla\Delta P_{br,j}^{sk} = \nabla\Delta \rho_{br}^{sk} + \gamma_j \nabla\Delta I_{br,1}^{sk} + \nabla\Delta T_{br}^{sk} + \nabla\Delta \varepsilon_{br,j}^{sk} \\ \nabla\Delta L_{br,j}^{sk} = \nabla\Delta \rho_{br}^{sk} - \gamma_j \nabla\Delta I_{br,1}^{sk} + \nabla\Delta T_{br}^{sk} + \lambda_j (\nabla\Delta N_{br,j}^{sk}) + \nabla\Delta \xi_{br,j}^{sk} \end{cases} \tag{2.4}$$

where Δ is between-satellite differencing operator ($\Delta(\bullet)^{sk} = (\bullet)^s - (\bullet)^k$). Equation (2.4) is the commonly used double-differenced measurement, from which it can be noticed that the receiver-related hardware biases and receiver clock offset are eliminated. What remains in the equation are baseline vector, double-differenced atmospheric residuals, double-differenced ambiguities, and corresponding noise. The noise level of double-differenced measurements has been amplified by approximately two times according to error propagation law. Due to the high spatial correlation in atmosphere within a small region (e.g., baseline distance of tens of kilometres), the double-differenced ionospheric and tropospheric effect can be small enough to be ignored. For smartphone applications, the distance between user and base station is usually within tens of kilometres, therefore, the smartphone RTK mathematic model is as Equation (2.5).

$$\begin{bmatrix} \nabla\Delta\hat{P}^{sk}_{br,j} \\ \nabla\Delta\hat{L}^{sk}_{br,j} \end{bmatrix} = \begin{bmatrix} \nabla\Delta e^{sk}_{br,x} & \nabla\Delta e^{sk}_{br,y} & \nabla\Delta e^{sk}_{br,z} & 0 \\ \nabla\Delta e^{sk}_{br,x} & \nabla\Delta e^{sk}_{br,y} & \nabla\Delta e^{sk}_{br,z} & \lambda_j \end{bmatrix} [dX \quad dY \quad dZ \quad \nabla\Delta N^{sk}_{br,j}]^T \tag{2.5}$$

2.1.2 Precise Point Positioning

The un-differenced and un-combined (UDUC) PPP model is usually applied in smartphone PPP data processing to accommodate single/dual-mixed frequency GNSS measurements. The UDUC PPP mathematic model can be represented as Equation (2.2).

$$\begin{bmatrix} \hat{P}^s_j \\ \hat{L}^s_j \end{bmatrix} = \begin{bmatrix} e^s_x & e^s_y & e^s_z & 1 & mf^s_w & \gamma_j & 0 \\ e^s_x & e^s_y & e^s_z & 1 & mf^s_w & -\gamma_j & \lambda_j \end{bmatrix} \begin{bmatrix} dX & dY & dZ & \tilde{dt}_r & ZWD & \tilde{I}^s_1 & \tilde{N}^s_j \end{bmatrix}^T \tag{2.2}$$

where $\hat{P}$ and $\hat{L}$ are the pseudorange and phase measurement misclosure, and can be calculated with raw observation and a priori state information. e^s_x, e^s_y, and e^s_z are line-of-sight unit direction vectors from satellite to receiver, mf^s_w is the wet mapping function (MF) of tropospheric zenith wet delays (ZWD). The tilde markers on the estimates infer that the parameters have biases. dX, dY, and dZ are the corrections to the given a priori initial approximate coordinates under earth-centred-earth-fixed (ECEF) coordinate system, $\tilde{dt}_r$ is estimated as a function of receiver clock and receiver hardware delays, ZWD is the tropospheric zenith wet delay. $\tilde{I}_1$ denotes a combination of ionospheric delays on the first frequency and satellite differential code bias (DCB). $\tilde{N}$ is the float ambiguity which absorbed the hardware phase delays and unmodelled errors. The corrected model errors in $\hat{P}$ and $\hat{L}$ are satellite phase centre offset (PCO) and phase centre variation (PCV), phase windup, tidal loading, and relativistic effect. For smartphone processing, no receiver PCO and PCV is applied, but they should be corrected in higher grade receivers.

2.1.3 PPP-RTK

PPP usually suffers from a long initial convergence time to reach high accuracy positioning performance. Introducing satellite phase biases and atmosphere corrections to conventional PPP processing enables PPP-RTK technology to have faster initial solution convergence compared to PPP, benefiting various application fields, especially for real-time cases. Normally, a two-dimension processing strategy is applied to generate atmosphere corrections at the server side and to conduct PPP-RTK at the user side, as shown in Figure 2.1.

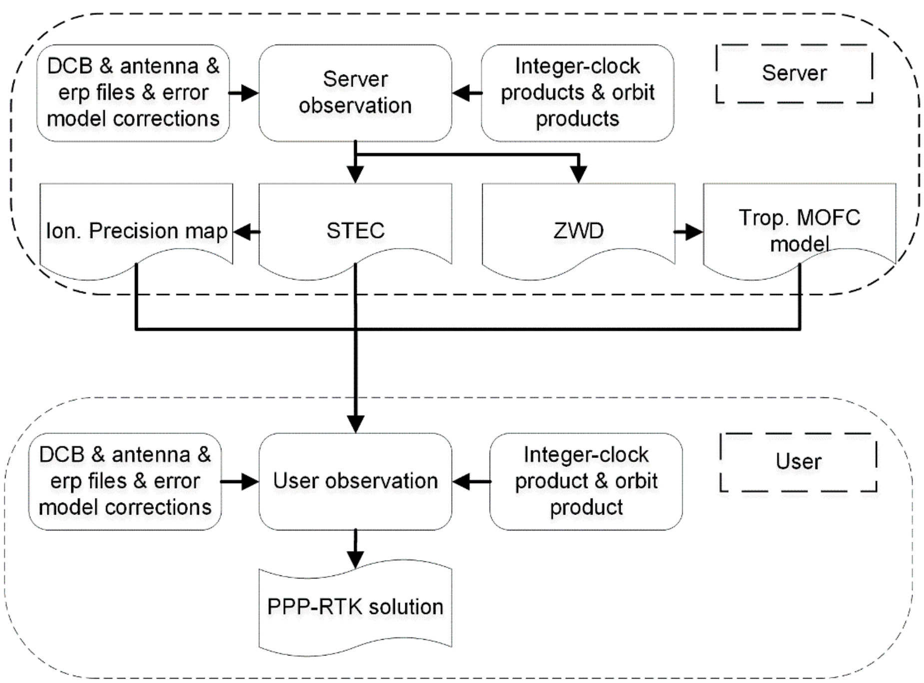

Figure 2.1 Example of simplified PPP-RTK flowchart at the server and the user. The server side (upper) contains generation of correction products, and the user side (bottom) utilizes these corrections for PPP-RTK.

The UDUC PPP model is highly suitable for the PPP-RTK server, as the raw GNSS measurements can be used to directly estimate both slant ionospheric and zenith tropospheric wet delays. To ensure high precision atmospheric corrections, ambiguity resolution is conducted for the reference station network. Station-by-station UDUC PPP AR is performed, and the regional tropospheric corrections are modelled using, e.g., the modified optimal fitting coefficients (MOFC) model (Cui et al. 2022), with model coefficients and the modelling precision factor broadcasted to the user.

For PPP-RTK users, the derived slant ionospheric corrections of all reference stations and the tropospheric delay model coefficients are transmitted. Users can interpolate corrections from nearby reference stations and apply them to their locations. For instance, one method of calculating interpolated slant ionospheric correction is represented in Equation (2.6) (Hu et al. 2023d).

$$stec_{corr}^{s} = \frac{\sum_{1}^{3}(stec_i^s / dis_i^{\,2})}{\sum_{1}^{3}(1/dis_i^{\,2})} \tag{2.6}$$

where $stec_i^s$ is the slant ionospheric information for satellite s and server station i, dis_i is the distance from the server station to the user. It should be noted that server-derived slant total electron content (STEC) is grouped with the receiver differential code bias. Therefore, to eliminate the influence of receiver DCB in the correction, a reference satellite is selected to form single-differenced STEC correction for users when applying the ionospheric corrections. With interpolated STEC corrections and calculated tropospheric model value, the tropospheric constraints ($\tilde{T}$) and between-satellite differenced STEC with respect to reference satellite k ($\tilde{I}^1 - \tilde{I}^k, \cdots, \tilde{I}^s - \tilde{I}^k$) can be applied as virtual observations when appended to the raw UDUC PPP mathematic model (Equation (2.2)), With ς representing the residuals, the virtual observation is as Equation (2.7), and the final design matrix for PPP-RTK is as Equation (2.8).

$$
\begin{bmatrix} \tilde{T} \\ \tilde{I}^1 - \tilde{I}^k \\ \vdots \\ \tilde{I}^s - \tilde{I}^k \end{bmatrix} = \begin{bmatrix} 1 & 0 & \cdots & 0 & \cdots & 0 \\ 0 & 1 & \cdots & -1 & \cdots & 0 \\ & & & \ddots & & \\ 0 & 0 & \cdots & -1 & \cdots & 1 \end{bmatrix} \begin{bmatrix} T \\ I^1 \\ \vdots \\ I^k \\ \vdots \\ I^s \end{bmatrix} + \begin{bmatrix} \varsigma T \\ \varsigma I^1 - \varsigma I^k \\ \vdots \\ \varsigma I^s - \varsigma I^k \end{bmatrix} \tag{2.7}
$$

$$
A = \begin{bmatrix} e_x^1 & e_y^1 & e_z^1 & 1 & mf^1 & \gamma_j & \cdots & 0 & 0 & \cdots & 0 \\ e_x^1 & e_y^1 & e_z^1 & 1 & mf^1 & \gamma_j & \cdots & 0 & \lambda_j & \cdots & 0 \\ & & & & & & \vdots & & & & \\ e_x^s & e_y^s & e_z^s & 1 & mf^s & 0 & \cdots & \gamma_j & 0 & \cdots & 0 \\ e_x^s & e_y^s & e_z^s & 1 & mf^s & 0 & \cdots & \gamma_j & 0 & \cdots & \lambda_j \\ 0 & 0 & 0 & 0 & 1 & 0 & \cdots & 0 & 0 & \cdots & 0 \\ 0 & 0 & 0 & 0 & 0 & 1 & \cdots & 0 & 0 & \cdots & 0 \\ & & & & & & \vdots & & & & \\ 0 & 0 & 0 & 0 & 0 & 0 & \cdots & 1 & 0 & \cdots & 0 \end{bmatrix} \tag{2.8}
$$

2.2 Estimation and correction strategies

The estimation and correction strategies of the parameters differ in different positioning techniques. Therefore, this section gives a brief introduction on the strategies in relative positioning, PPP, and PPP-RTK, respectively.

Satellite orbit and clock: satellite orbit and clock can be obtained from either broadcast ephemeris or precise products from analysis centres (Montenbruck et al. 2018). For RTK users, the broadcast ephemeris is usually used, as most of the satellite orbit and clock errors would be eliminated by double-differencing (DD) process. For PPP and PPP-RTK users, the precise orbit and clock corrections are provided by ACs. With current precise orbit determination (POD) and precise clock estimation (PCE) strategies, IGS final satellite orbit and clock products are achieving accuracy of several centimetres and better than 0.1 ns, respectively, which could satisfy most of the users. When using precise orbit product, it should be noted that satellite PCO and PCV should be applied to switch the centre of mass (CoM) to antenna phase centre (APC) (Schmid et al. 2005).

Tropospheric refraction: Tropospheric refraction is usually divided into wet and hydrostatic components, where the hydrostatic part is impacted by temperature and pressure, and is relatively stable compared to wet component (Thomas and Norbert 2017). Therefore, the hydrostatic part can be precisely modelled and corrected. For RTK users, the tropospheric refraction can be mostly eliminated by DD, especially for a short baseline. For PPP users and PPP-RTK users, the hydrostatic component can be calculated with empirical zenith hydrostatic delay (ZHD) model (e.g., Saastamoinen model) and corresponding mapping function, while the wet component should be either estimated or constrained with precisely modelled zenith wet delay model. There are three commonly used troposphere mapping functions in GNSS filed, e.g., Niell mapping function (NMF) (Niell 1996), global mapping function (GMF) (Boehm et al. 2006), and Vienna mapping function (VMF) (Kouba 2008). NMF and GMF are empirical models, while VMF is built based on the atmosphere monitoring and observation.

Ionospheric refraction: Ionospheric refraction is a frequency-dependent effect, and low-orders can be eliminated through GNSS ionospheric-free (IF) combination (Zumberge et al. 1997; Kouba and Héroux 2001). Considering UDUC model is applied in this dissertation, the ionospheric refraction needs to be considered. Similar to tropospheric refraction, it can be eliminated with DD measurements in RTK. For PPP users, the slant ionospheric delay at the first frequency is estimated for each satellite, while it is constrained in PPP-RTK with ionospheric corrections. It is worth mentioning that for smartphone UDUC PPP processing, some smartphone GNSS chipsets only record single-frequency measurements for some constellations, e.g., Xiaomi Mi8 GLONASS and BDS measurements are all single-frequency when collecting in and around York University. In this case, if the slant ionospheric delays and ambiguities are estimated simultaneously, there would be a rank deficiency in the mathematical model. The solution to this issue in this dissertation is to constraint it with Klobuchar model (Klobuchar 1987).

Receiver coordinates: For most users, their positions are of the most interest, and the estimation of receiver position relies on the dynamics of the receiver. For a static receiver, the user position is regarded as unchanged in time, which means no velocity is estimated, and no processing noise is applied. When the receiver is moving, there are different ways to model the receiver coordinates. A simplified method is to model the receiver coordinates as white noise, which is to apply a large variance on the approximate initial position. Another method is to use a position, velocity, and acceleration (PVA) estimator and apply processing noise to these parameters according to different receiver dynamics (e.g., large processing noise for high-dynamic situations such as aircraft, medium processing noise for car, and low processing noise for pedestrians).

Receiver clock: The satellite contains high-precision and stable oscillators, while the user receiver has a low-grade oscillator, indicating difficulty in precisely modelling receiver clock offset. In RTK processing, the receiver clock offset can be eliminated with DD. However, in PPP and PPP-RTK, the receiver clock error needs to be modelled as white noise. Moreover, considering the different receiver hardware delays for different constellations, receiver clock error parameters should be estimated for each GNSS constellation.

Ambiguity: Carrier phase ambiguities are usually estimated as float values in GNSS data processing due to the measurement noise and unmodelled errors. In principle, it should be an integer account of wavelengths. In RTK, the DD ambiguities are estimated, and in PPP and PPP-RTK, un-differenced ambiguities are estimated. In data processing strategy, ambiguities are usually modelled as constant or random walk process with a small processing noise.

Error corrections: In addition to the parameters mentioned above, which are either estimated in the estimator or eliminated through measurement-differencing, there are other errors which need to be carefully corrected in advance. These corrections are based on existing models or by public products and are usually corrected in PPP and PPP-RTK. For instance, sagnac effect, antenna phase wind-up (Wu et al. 1993), antenna PCO/PCV, solid earth tides, and ocean loading (Kouba 2009).

In summary, Table 2.1 provides the common parameter processing strategies used in this dissertation unless otherwise specified. For RTK, it should be noted that when the baseline length is long (e.g., longer than 100 km), or when the ionosphere is active (e.g., during solar activities), double-differencing cannot perfectly eliminate all the common errors.

Table 2.1 Common parameter estimation and correction strategies used in this dissertation

Parameters	RTK	PPP	PPP-RTK
Coordinates	White noise	White noise	White noise
Receiver clock	DD eliminated	White noise	White noise
ZWD	DD eliminated	Estimated	Estimated and constraint
ZHD	DD eliminated	Saastamoinen model	Saastamoinen model
Trop. mapping function	-	NMF	NMF
Ionospheric effect	DD eliminated	Corrected using Klobuchar model and estimate the residuals	Corrected using model value and estimate the residuals
Satellite orbit/clock	Broadcast ephemeris	Products from AC	Products from AC
Code bias	DD eliminated	Products from AC	Products from AC
Phase bias	DD eliminated	Products from AC	Products from AC

2.3 State vector estimation

Different filters are usually used in parameter estimation. Normally, least-squares is applied for standard point positioning or single-epoch precise positioning, which means that the estimated parameters are epoch-independent. In precise positioning, previous filtered information can be utilized to provide a priori information for current epoch, thereby sequential least squares and EKF are commonly applied in state estimation. It should be noticed that Equation (2.1) is a non-linear function, indicating that it should be linearized first using Taylor series expansion.

2.3.1 Least squares

The observation equation can be given as Equation (2.9), where Z is the observation, and V is the measurement noise.

$$Z = h(x) + V \tag{2.9}$$

In GNSS measurements, $h(x)$ is a nonlinear function which contains geometrical range between satellite and receiver positions. The linearized observation equations can be derived as:

$$z = Z - h_0 = HX + V \tag{2.10}$$

where H is the design matrix, h_0 can be calculated with approximate a priori states. With a given measurement weighting matrix W, the LS solution ($\hat{X}$) and corresponding variance-covariance matrix ($Q_{\hat{X}}$) can be derived as Equations (2.11) and (2.12):

$$\hat{X} = (H^T W H)^{-1} H^T W z \tag{2.11}$$

$$Q_{\hat{X}} = (H^T W H)^{-1} \tag{2.12}$$

where superscript T denotes the transpose of the matrix. With the LS estimates, a posteriori residuals and the standard deviation of unit weight can be calculated as Equations (2.13) and (2.14).

$$v = H\hat{X} - z \tag{2.13}$$

$$\sigma_{ls}^2 = \frac{v^T W v}{l - n} \tag{2.14}$$

where $l-n$ is the degree of freedom. Normally, for a nonlinear observation function, iteration of LS is applied to reduce the error from linearization, as:

$$\hat{X}_{LS} = X_0 + x_{LS1} + x_{LS2} + \cdots + x_{LSk} \tag{2.15}$$

2.3.2 Sequential least squares

Error equation at epoch $t+1$ can be given as:

$$z_{t+1} = h_{t+1} X_{t+1} + v_{t+1} \tag{2.16}$$

Utilizing observations from previous epochs, the estimates and corresponding variance-covariance matrix of epoch t is used in updating the current solution, and the sequential least square solution is:

$$\hat{X}_{t+1} = \hat{X}_t + K_{t+1} \Delta z_{t+1} \tag{2.17}$$

$$\begin{aligned} K_{t+1} &= Q_{\hat{X}_{t+1}} h_{t+1}^T w_{t+1} \\ &= (Q_{\hat{X}_{t+1}}^{-1} + h_{t+1}^T w_{t+1} h_{t+1})^{-1} h_{t+1}^T w_{t+1} \end{aligned} \tag{2.18}$$

$$\Delta z_{t+1} = z_{t+1} - h_{t+1} \hat{X}_t \tag{2.19}$$

where Δz_{t+1} is the observation-minus-calculation (OMC) misclosure vector with approximate estimate values from $\hat{X}_t$. w_{t+1} is the measurement weighting vector at epoch $t+1$. The a posteriori unit weight variance can be derived as:

$$\sigma_{sls,t+1}^2 = \frac{v_{t+1}^T W_{t+1} v_{t+1}}{l_{t+1} - n} \tag{2.20}$$

2.3.3 Extended Kalman filter

For a linear model, Kalman filter is the optimal estimation, however, due to the nonlinear mathematical model of GNSS measurements, extend Kalman filter is usually applied. The linearized observation equation at epoch t is as Equation (2.10), and the state equation is as Equation (2.21).

$$X_t = \Phi_{t,t-1} X_{t-1} + \Lambda_{t,t-1} \partial_{t-1} \tag{2.21}$$

where $\Phi_{t,t-1}$ is the state transition matrix from epoch $t-1$ to t, Λ is the system noise transition matrix, and ∂ is the system noise vector. With EKF, the predicted state parameter vector ($\hat{X}_{t,t-1}$) and predicted variance-covariance matrix ($\hat{P}_{t,t-1}$) are as Equations (2.22) and (2.23), and the estimate vector ($\hat{X}_t$) and corresponding variance-covariance matrix ($\hat{P}_t$) can be updated as Equations (2.26) and (2.27).

$$\hat{X}_{t,t-1} = \Phi_{t,t-1} \hat{X}_{t-1} \tag{2.22}$$

$$\hat{P}_{t,t-1} = \Phi_{t,t-1} \hat{P}_{t-1} \Phi_{t,t-1}^T + \Lambda_{t,t-1} Q_{\partial-1} \Lambda_{t,t-1}^T \tag{2.23}$$

$$K_t = \hat{P}_{t,t-1} H_t^T (H_t \hat{P}_{t,t-1} H_t^T + R_t)^{-1} \tag{2.24}$$

$$V_{z,t} = Z_t - h_t(\hat{X}_{t,t-1}) \tag{2.25}$$

$$\hat{X}_t = \hat{X}_{t,t-1} + K_t V_{z,t} \tag{2.26}$$

$$\hat{P}_t = (I - K_t H_t) \hat{P}_{t,t-1} \tag{2.27}$$

where R_t is the variance of the observations. Similarly, the a posteriori unit weight variance can be derived as:

$$\sigma^2_{ekf,t} = \frac{(H_t \hat{X}_t)_t^T W_t (H_t \hat{X}_t)}{l_t - n} \tag{2.28}$$

3 RANGE ERROR: UNDERSTAND SMARTPHONE MEASUREMENTS IN REALISTIC ENVIRONMENTS

This chapter focuses on smartphone range error derivation and characterization in realistic driving environments, aiming to provide in-depth insight to smartphone measurement quality in typical use. The range error derivation method is first introduced, in which special consideration of lever-arm compensation has been taken into account. Three datasets were collected to characterize smartphone range errors under different environments, at the same time, range errors for one pair of geodetic datasets were also calculated for comparison. Constellation- and frequency-specific smartphone range errors are first assessed, followed by an investigation of the correlation among range errors, elevation angles, and C/N_0 values. To understand how the surrounding environments affect smartphone range errors, range errors under different environments are evaluated, which contains suburban, open-sky, and vegetated areas. The correlation between range errors and RTK pre-fit residuals are analyzed. And finally, considering a more realistic smartphone application in which the smartphone is mounted in the car, smartphone range errors are derived from datasets collected on the car roof and dashboard and their characteristics are compared. The work in this chapter has been published in Hu et al. (2023a).

3.1 Introduction and motivation

Currently, the major limitation preventing smartphone-based precise applications are the noisy and frequent missing measurements due mainly to the poor linearly polarized antenna and multipath contamination. Therefore, several studies have been carried out to investigate smartphone signal strength, stochastic modelling, observation noise characterization, and measurement optimization strategies. It is generally agreed in the literature that C/N_0-based weighting schemes are more appropriate for smartphone positioning compared to elevation-based weighting schemes (Shinghal and Bisnath 2021; Banville et al. 2019; Zhang et al. 2018a). To mitigate the negative impacts of native smartphone antennas, Riley et al. (2017) revealed that smart devices with different grades of GNSS antennas are likely to perform significantly better in localization and provided insight into GNSS antenna replacement. Subsequent contributions confirm that smartphone centimetre-level solutions are achievable with an external geodetic antenna through relative positioning (Geng et al. 2018) and PPP-AR (Wen et al. 2020).

As unexpected smartphone measurement noise may reach dozens of metres (Paziewksi 2020; Liu et al. 2019; Zhang et al. 2018a; Li and Geng 2019), smartphone observation quality assessment has received considerable attention from researchers. Lachapelle et al. (2018) evaluated the pseudorange quality from Huawei P10 through code and phase measurements difference, and results illustrate that smartphone code measurements are ten times noisier than geodetic GNSS receivers. Similar conclusions can be drawn from Zhang et al. (2018b), Paziewski et al. (2019), and Wanninger and Heßelbarth (2020). Moreover, Liu et al. (2019) adopted a short baseline and the single-difference approach between the reference station and smartphone observations to assess the pseudorange residuals including multipath errors and observation noise, and this study showed that there are 10-30 m gross errors existing in smartphone code measurements compared to geodetic receivers, and vary between different constellations. Furthermore, by utilizing the multipath combination algorithm (Robustelli and Pugliano 2019; Robustelli et al. 2019), it is confirmed that L5/E5a signals are significantly less influenced by the multipath effect compared to L1/E1 signals, owing to their higher transmission power level.

It is well recognized that receiver noise and multipath effects significantly limit smartphone precise positioning and, therefore, its applications. However, in view of all the work mentioned, few studies focus on smartphone data quality analysis in realistic, e.g., driving environments; many experiments are stabilized on open rooftops or vehicle roofs, which do not correspond to consumer habits in daily life. To improve understanding of smartphone measurement behaviour and further enhance the stochastic modelling and estimation processes, this chapter provides a detailed assessment of the actual smartphone range errors under different driving scenarios. No publications have explored the relationship between range errors with satellite geometry, signal strength, as well as pre-fit residuals under multiple multipath profiles, nor the range errors and their distribution differences caused by different smartphone mounting location. Therefore, the main contributions of this work are to answer the following questions: (1) How does the smartphone range error distribution behave based on different signal frequencies and constellations? (2) What is the relationship among range errors, satellite elevation angles, and SNR values? (3) How does range error vary under different multipath profiles in real driving environments? Do any differences exist with different mounting locations? (4) What is the correlation between smartphone pre-fit residuals and range errors? The novelties of this chapter are in analyzing the range errors under different environments, investigating the correlation between pre-fit residuals and range errors, and also comparing the range errors for smartphones mounted on a car roof and dashboard.

3.2 Range error derivation

To calculate the range errors for the smartphone, a collocated geodetic-grade receiver is needed as a reference, for which the range errors can be neglected compared to the noisier smartphone measurements. Figure 3.1 illustrates the receiver sets (*A* and *B*) mounted on the car with the tracked satellites *m* and *n*. The range errors can then be generated using measurement-differenced or state-differenced methods. In the measurement-differenced method, double-differencing is conducted with raw observations from two close receivers with consideration of the antenna lever arm correction, while in the state-differenced method, the state terms such as slant ionospheric effect, zenith troposphere delay are derived using the UDUC PPP model from the reference receiver and applied to the smartphone as “true” values, and then single-differenced state residuals are computed to eliminate receiver-related terms, and hence the range errors are obtained. It should be noted that, due to the differencing procedure, the calculated range errors would be enlarged correspondingly through error propagation.

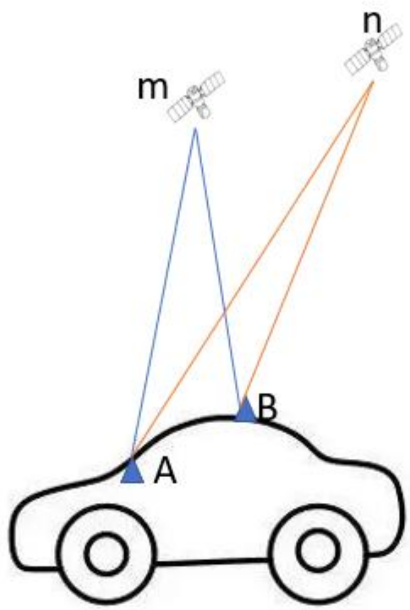

Figure 3.1 Illustration of receiver suits on a car (Receiver A on the dashboard and B on the car roof) and the tracked satellites (satellite *m* and *n*)

With smartphone *A* and collocated receiver *B*, the double-differenced pseudorange measurement between receiver *A* and *B* and satellite *m* and *n* on j^{th} frequency can be given as Equation (3.1):

$$\nabla\Delta P = (\rho_A^m - \rho_A^n) - (\rho_B^m - \rho_B^n) + \delta I + \delta T + (\varepsilon_A^m - \varepsilon_A^n) - (\varepsilon_B^m - \varepsilon_B^m) \tag{3.1}$$

where δI and δT are the ionosphere and troposphere residuals after double-differencing, respectively. For two close receivers whose lever-arm is within several metres, the atmospheric delays can be eliminated by performing double-differencing, thus δI and δT can be ignored.

With two assumptions, that (*i*) the range errors for geodetic-grade receiver *A* can be ignored compared to those of smartphone *B*, and (*ii*) the satellite with the highest elevation angle which is chosen as reference satellite when performing between-satellite differencing has significantly lower range errors compared to lower-elevation satellites, the measurement-differenced range errors can therefore be derived as Equation (3.2):

$$rangeerror = \nabla\Delta P - (\rho_A^m - \rho_A^n) + (\rho_B^m - \rho_B^n) \tag{3.2}$$

where the geometry distance ρ^m can be given as a function of receiver position (x, y, z) for satellite m (x^m, y^m, z^m) as Equation (3.3):

$$f(x,y,z) = \rho^m = ((x-x^m)^2 + (y-y^m)^2 + (z-z^m)^2)^{1/2} \tag{3.3}$$

In a realistic environment, the lever arm between A and B is constant in the vehicle body coordinate system, and can be transformed to the epoch-wised ECEF coordinate system using the approximate position of vehicles. Take one specific epoch for example, with the coordinates of receiver A (X_A, Y_A, Z_A), satellite m (x^m, y^m, z^m) and the lever arm (X_0, Y_0, Z_0), Taylor's formula can be applied to ρ_B^m at the approximate position of A as Equation (3.4):

$$\rho_B^m \left|_{(x,y,z)=(X_A,Y_A,Z_A)} = \rho_A^m + f^{'}(x,y,z) \cdot (X_0,Y_0,Z_0) + f^{''}(x,y,z) \cdot \frac{(X_0,Y_0,Z_0)}{2} + \cdots \right. \tag{3.4}$$

The second order term of Equation (3.4) can then be derived as $\frac{1}{2}(\frac{X_0}{\rho_A^m} + \frac{Y_0}{\rho_A^m} + \frac{Z_0}{\rho_A^m})$ and can be ignored because of the metre-level lever arm parameters. In this way, only the first order term of Equation (3.4) is taken into consideration, and hence Equation (3.2) can be further reparametrized as Equation (3.5):

$$\begin{aligned} rangeerror = \nabla\Delta P - ((& \frac{X_A - x^m}{\rho_A^m} X_0 + \frac{Y_A - y^m}{\rho_A^m} Y_0 + \frac{Z_A - y^m}{\rho_A^m} Z_0) \\ & - (\frac{X_A - x^n}{\rho_A^n} X_0 + \frac{Y_A - y^n}{\rho_A^n} Y_0 + \frac{Z_A - y^n}{\rho_A^n} Z_0)) \end{aligned} \tag{3.5}$$

It can be noted from Equation (3.5) that the coefficients of the lever-arm values are the line-of-sight (LOS) unit vector values from receiver A to satellites, and corresponding coefficients can be determined reliably even with a ten-metre-accuracy approximate position. Table 3.1 provides an example of the coefficients calculated from rover and base stations with baseline distance of ~2 metres, where the observed satellite elevation angle is 6°. It is shown that even for a low elevation satellite, the differences for the coefficients are only at $\sim 10^{-6}$ level, and the corresponding influence on the calculated range errors using Equation (3.5) would be less than one millimetre. Therefore, the measurement-differenced range errors can be derived with only the pseudorange measurements and the fixed lever arm.

Table 3.1 Example of line-of-sight unit vector values (e_x, e_y, e_z) from a satellite with an elevation angle of 6° observed by rover and base stations

	e_x	e_y	e_z
Rover	0.6576667	0.6470226	0.3857928
Base	0.6576668	0.6470225	0.3857929

Aside from the measurement-differenced method, there is another straightforward approach to estimate range errors through pseudorange residual differencing between satellites. This state-differenced method can better show the estimated state characteristics than the measurement-differenced method. Correspondingly, all receiver-dependent states are eliminated with the relative range errors remaining, and the state-differenced or PPP-based range errors can be expressed as Equation (3.7):

$$\Delta P = P_{A,j}^{m} - P_{A,j}^{n} = (\rho_A^m - \rho_A^n) + (I_{A,j}^m - I_{A,j}^n) + (T_A^m - T_A^n) + (\varepsilon_A^m - \varepsilon_A^n) \tag{3.7}$$

Compared to the aforementioned measurement-differenced range errors, the calculated range errors noise is only amplified once from the differencing. However, it requires accurate satellite-dependent states such as geometric ranges, ionospheric delays, as well as tropospheric delays during computation. Furthermore, other terms such as relativity corrections, Sagnac corrections, solid tide corrections, and satellite antenna corrections need to be taken into consideration in state-differenced method.

3.3 Measurement campaigns and experimental setup

The data for the analysis were collected in and around York University, Toronto, Canada. York University and adjoining areas cover all the aspects of multiple multipath profiles needed for the experiment. The profiles include highways, parking lots, suburban with vegetation, overpasses, and open sky environments, each having a unique multipath characteristic and contributing to better appreciate the range error behaviours. Figure 3.2 shows the aerial and detailed street view photos of these measurement campaigns, and blue arrows indicate the direction.

(a) (b)

(c) (d)

Figure 3.2 Illustration of data collection trajectory (a) and different environments contains open-sky parking lots (b), suburban road (c), and short underpass (d)

As shown in Figure 3.3, the experimental setup contains two sensor suites. The first contains two geodetic GNSS receivers to provide position trajectory references for tested smartphone. One NovAtel OEM7 receiver was mounted on a rooftop as a reference station within a 5 km baseline, whilst the other receiver was connected with a geodetic antenna and mounted inside the vehicle experimental box (Figure 3.3 (a)). The second sensor suite includes Xiaomi Mi 8 phone, which was fixed with holders and mounted on the vehicle dashboard to mimic real-life applications (Figure 3.3 (b)). In addition, it was feasible to mount Mi 8 on the top of the experimental box for in-depth comparison and further analysis. The lever arm between the smartphone and the referenced centre has been carefully measured.

(a) (b)

Figure 3.3 Photos of experimental setup. (a) experimental vehicle and setup, (b) experimental smartphones

Table 3.2 highlights three datasets used in this study, including the test number, collections date, time duration, as well as phone mounted points. Road tests were carried out on two separate days with identical route and different traffic conditions, and the time durations for each test are 31, 28, and 29 min, respectively. These datasets are used and analyzed in the following section.

Table 3.2 Overview of collection dates, duration, and mounted areas of 3 smartphone kinematic datasets used in range error derivation

Test #	Collected date	Duration (UTC hour)	Mounted areas
1	2020-09-08	22:29-23:00	roof
2	2021-08-08	01:14-01:42	roof
3	2021-08-08	01:50-02:19	dashboard

3.4 Range error characteristics

The key to further improving the smartphone positioning performance is to understand the smartphone GNSS measurement characteristics. Therefore, analysis regarding range errors on different frequencies and the relationship between SNR values or elevation angles with range errors is first carried out, followed by the assessment of correlations between range errors and pre-fit residuals, range errors under different environments, and comparison of range errors when the smartphone is mounted on the car dashboard and roof. The smartphone data processing strategies have the assumption that the measurement errors should follow a similar distribution as geodetic receivers; therefore, the zero baseline ZIM2-ZIM3 multi-GNSS experiment (MGEX) stations are processed as a reference to provide a clear view of the characteristics of smartphone range errors compared with geodetic receivers. It is worth mentioning that the first (L1 for GPS and GLONASS, E1 for Galileo, and B1 for BDS) and third (L5 for GPS, and E5a for Galileo) frequencies are used in this analysis for both smartphone and geodetic receiver assessments. Hereafter, P1 and P5 are used to denote the first and third frequencies, respectively. SNR in this Chapter denotes the corresponding signal-to-noise density ratio recorded in the RINEX observation files. In the results analysis, dataset 1 is used in Sections 3.4.1-3.4.4, and datasets 2 and 3 are used in Section 3.4.5.

3.4.1 Distribution of range errors

The distribution of range errors on the first and third frequencies is first analyzed. As shown in Figure 3.4, the upper subplots show the distribution of range errors for the smartphone, while the lower panel gives the results for MGEX stations (ZIM2).

(a)

(b)

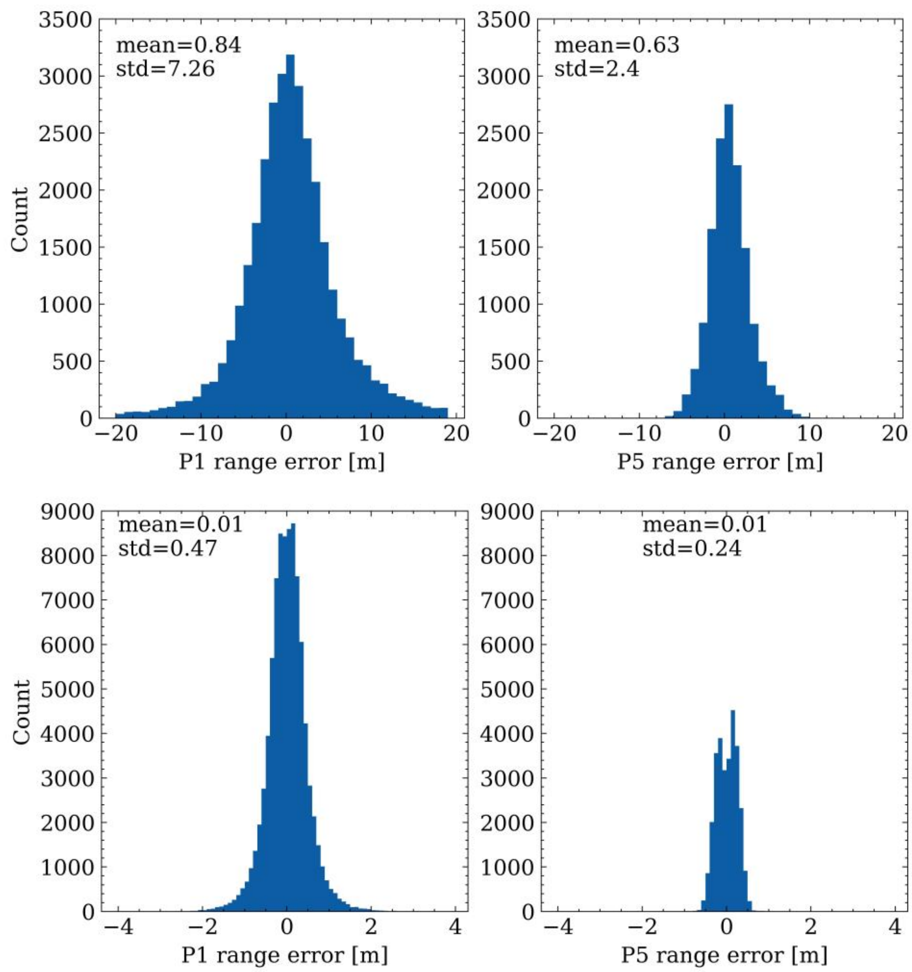

Figure 3.4 Distribution of range errors on P1 and P5 collected by different grades of receivers. (a) distribution of range errors from smartphones; (b) distribution of range errors from MGEX stations

It can be observed that, for both smartphone and geodetic receivers, the standard derivation (Std Dev) for the third frequency is smaller than the first frequency, with values of 7.3 m on P1 and 2.4 m on P5 for smartphones, and 0.5 m and 0.2 m for those of geodetic receivers, respectively, which indicates that the observation precision on the third frequency is higher. This difference may be due to the fact that the bandwidth of L5 is larger and the transmitted power of L5 is higher than the first frequency.

Therefore, the ability of avoid interference and noise may also be significantly improved for L5. The range errors for the geodetic receivers are obeying a nearly zero-mean distribution, while for smartphones, the mean values are not zero, but rather 0.8 m and 0.6 m for the first and third frequencies, respectively. When further investigating the range errors, the Std Dev of range errors for the geodetic receiver on P1 is 0.5 m, considering that the double-differenced measurements are formed when calculating the range errors, the original code precision should be 2 times smaller than the range errors by applying the error propagating law, which is 0.2-0.3 m. This value is consistent with the code precision used in MGEX data processing as in Hu et al. (2022), which demonstrates the validity of the proposed range error derivation method.

To provide a clear view of the characteristics of range errors for different constellations, Figure 3.5 illustrates the mean values and standard deviations of each constellation for smartphone and geodetic receivers. There are only a few GLONASS observations for ZIM2 and ZIM3. It can be concluded from Figure 3.5 that, among the four constellations, the GLONASS pseudorange measurements have the largest standard deviations, with values of 11.8 m and 0.7 m for smartphone and geodetic receivers. Therefore, in the GNSS data processing procedure, GLONASS pseudorange measurements are usually down weighted by a factor of 2, and these results on the first frequency are similar to what has been found in Liu et al. (2019). With the four constellations, except for Galileo, the standard deviations on P5 are nearly 2 times smaller than on P1, which infers that more weight can be put on the third frequency. For this smartphone dataset, the standard deviations are more than ten times larger compared to the corresponding constellations for geodetic receivers, and hence, for the analysis for range errors on different frequencies of different constellations, the stochastic models of the smartphone observation noise can be adjusted accordingly in the future research.

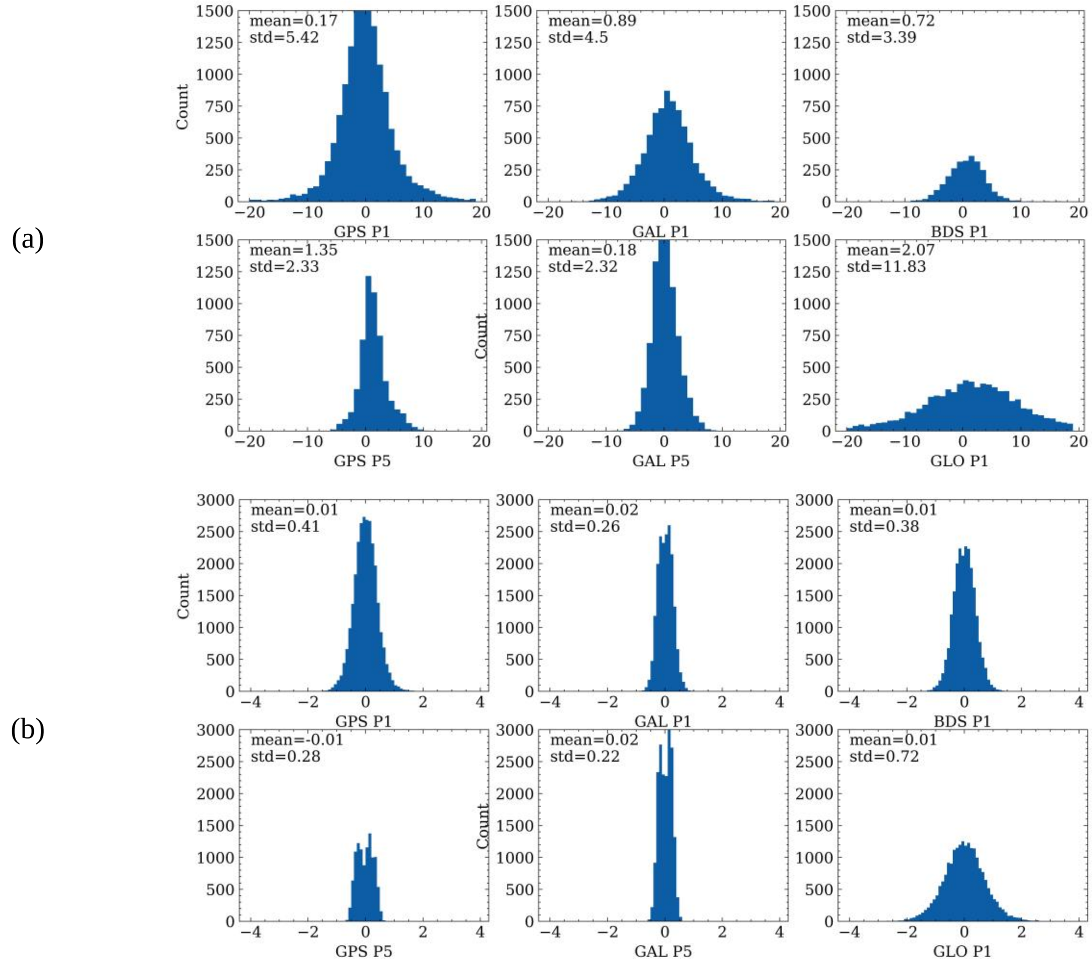

Figure 3.5 Distribution of range errors from different constellations and frequencies for (a) smartphone and (b) ZIM2 (units: m)

3.4.2 Range error correlation with elevation angle and C/N$_0$

Two common weighting schemes are applied to smartphone and geodetic receiver observations, namely C/N$_0$-based and elevation angle-based weighting, respectively. These two weighting schemes indicate that measurement quality is highly related to the C/N$_0$ and elevation angles. Therefore, in this subsection, the relationship between range errors, elevation angle, as well as C/N$_0$ values, is assessed. Figure 3.6 depicts the temporal characteristics of range errors and the corresponding relationship with C/N$_0$ and elevation angles, and different colours represent different satellites. In the correlation illustration, to provide a clear trend, the absolute value of the range errors are taken.

(a)

(b)

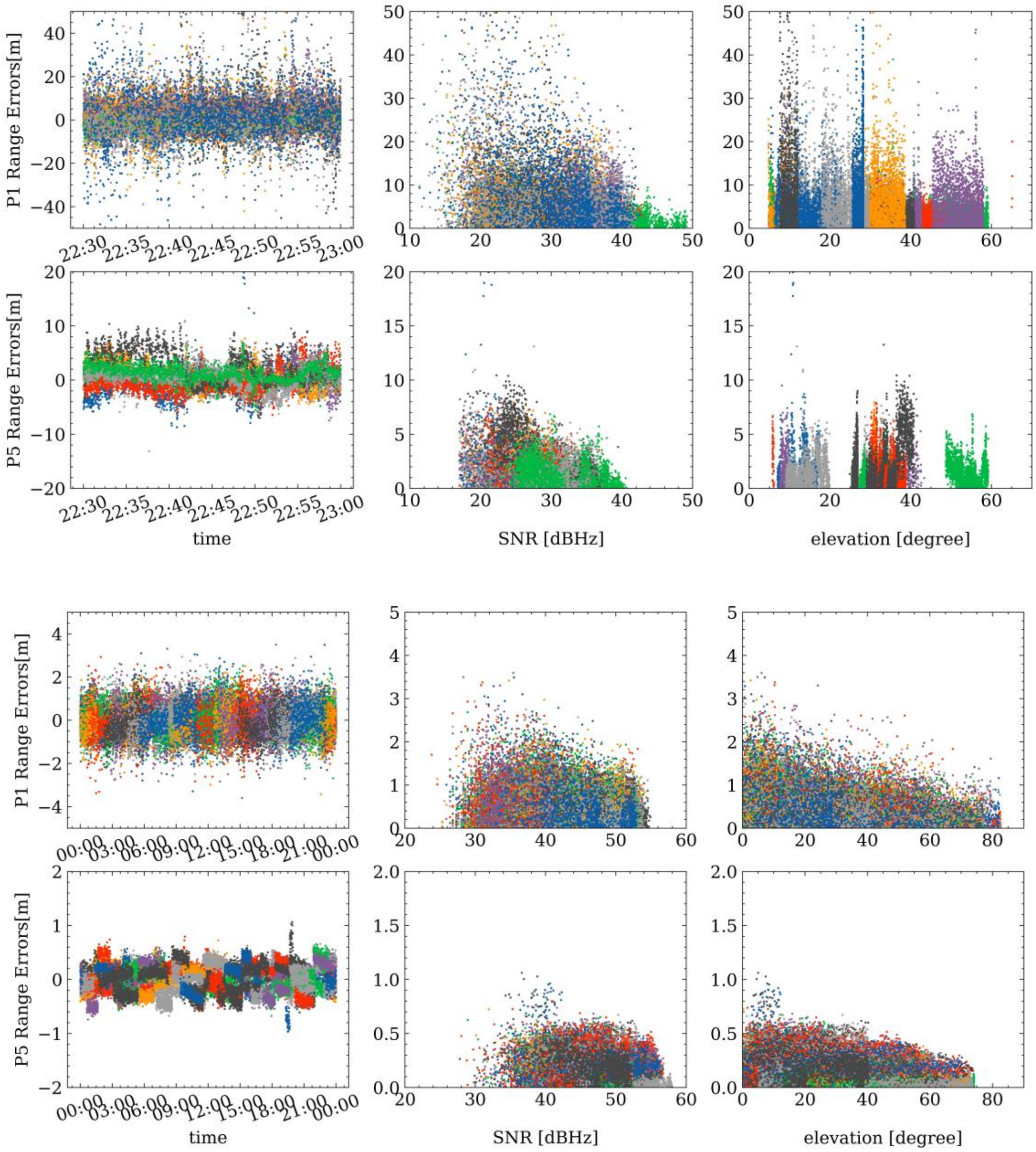

Figure 3.6 Time series of range errors (left), correlation between absolute range errors and C/N$_0$ (middle), and correlation between absolute range errors and elevation angles (right) for smartphone (a) and ZIM2 (b), respectively. Different colours represent different satellites

It can be noted again that the range errors on the first frequency are larger than those on the third frequency from the left panel which shows the time series of the range errors. In addition, there is a significant decreasing trend when the C/N$_0$ increases for smartphone data both for P1 and P5, and a similar situation can be observed when comparing the relationship between range error and elevation angle for geodetic receivers. Due to the relatively short observation time for the smartphone data (only

30 min), elevation angles are not fully distributed from 0-90 degrees. However, it can also be concluded that, when a satellite tracked by a smartphone is newly rising or setting, the range errors will increase slightly, and therefore the elevation cut-off angle should be set reasonably, e.g., cut-off angle of 10 is usually applied to reject the low elevation angle satellites. For the test ZIM2 observation, no correlation between range errors and C/N_0 can be found. The reason for this behaviour is that the geodetic receiver is under an open-sky observation environment, and the C/N_0 values are at a high level, which affects the range errors less.

To further investigate range error correlations, error bars are plotted in Figure 3.7 to show the mean values and standard deviations of the range errors at different SNR values and elevation angles. The dots and lines denote the mean values and standard deviations of range errors for all satellites, respectively. As shown in Figure 3.7, it can be clearly observed that there is a significant correlation between smartphone range errors and SNR values, especially on the first frequency. Concurrently, a small correlation on the P1 range errors for geodetic receivers can be observed, which is similar to the results in de Ponte Müller et al. (2013). The small standard deviation for geodetic receivers at low SNR values (around 25 dBHz) is due mainly to the limited observations with low SNRs. On the other hand, there is a decreasing standard deviation trend on P1 for the geodetic receiver when the elevation angles are increasing, while the mean values and standard deviations seem to be stable for P5, which have not been mentioned in the previous research.

In view of the existing literature, the SNR cut-off strategy is widely adopted to screen out satellites that are supposed to contain noisy measurements. However, in this work, it is interesting to identify that sometimes these measurements with lower SNR values are even less noisy and may be beneficial for positioning. This finding can be further used in an improved stochastic model. Furthermore, range error trends vary with different signal frequencies, indicating that weighting schemes need to be tuned and adjusted when applied to different signals. Meanwhile, the elevation angle-based weighting scheme is usually used for geodetic data processing, which might be well suited to the first frequency. However, there is also a potential weighting scheme that can be proposed in future research, to consider both elevation angle and SNR values or to apply different weighting schemes for different frequencies, and this is the scope of Chapter 5 in this dissertation.

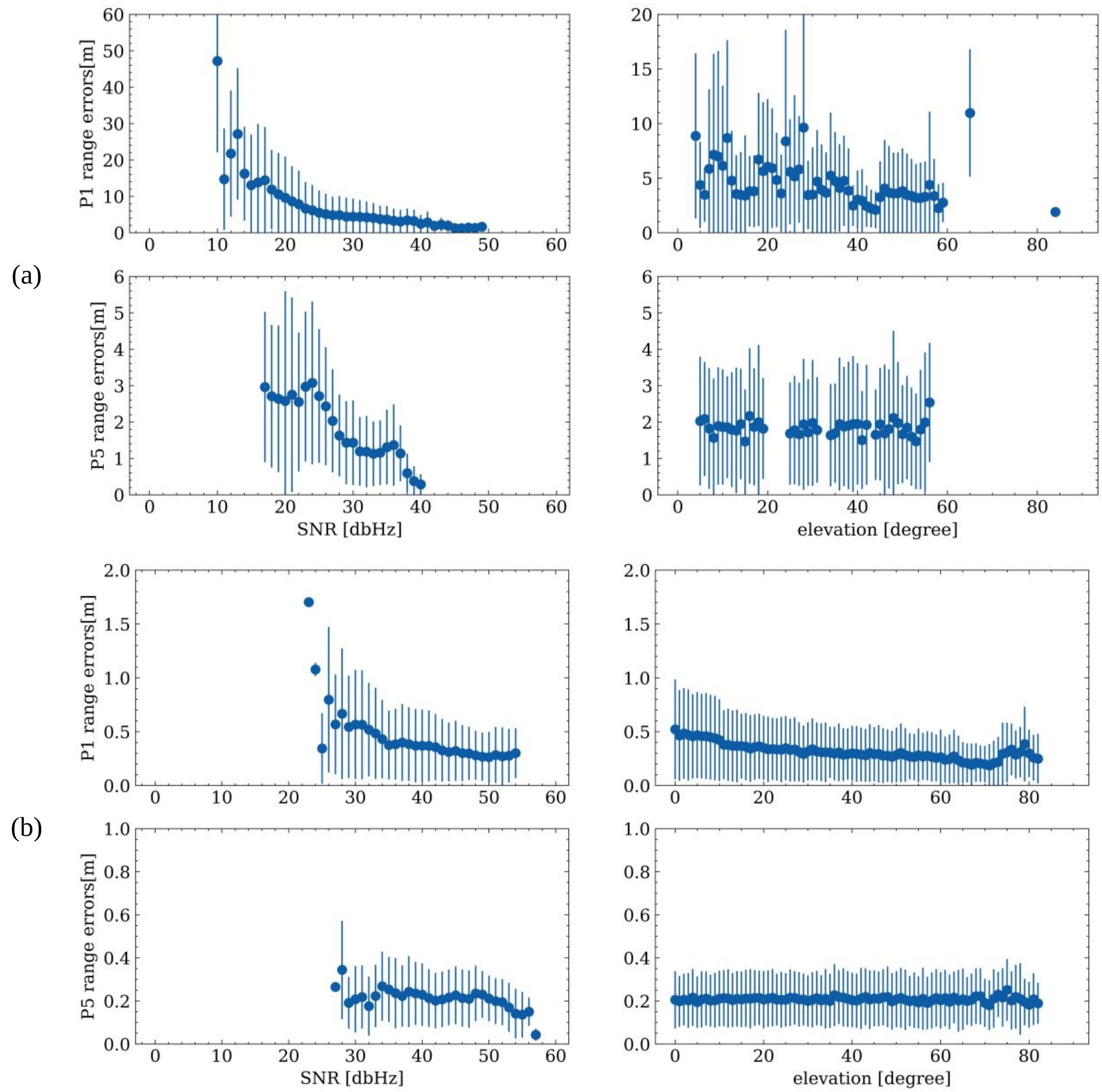

Figure 3.7 Error bars of range errors changing with SNR (left) and elevation angles (right) for smartphone (a) and ZIM2 (b). The dots and lines denote the mean values and standard deviations of range errors for all satellites, respectively

3.4.3 Environment-related range errors

GNSS measurements under environments such as urban canyons, overpasses and vegetation usually suffer from poor signal reception, low gain, large multipath errors, and noises, which result in variation and increases in range errors. To investigate this issue, the range errors under three scenarios are analyzed in this subsection to understand the impact of environment on them.

As shown in Figure 3.8, three typical epochs are selected for detailed analysis: (a) in a parking lot, and can be regarded as an open sky area; (b) in a suburban area, where the car was driving close to tall buildings; (c) in a vegetated area, where the car was close to trees on one side of the road. The sky plots on the right show the corresponding epoch, the second of the day (SoD), and range errors for different satellites are presented by different colours. It can be seen from Figure 3.8 that, owing to nearby buildings and trees limiting sky visibility, GNSS signals were blocked significantly, reducing satellite visibility. As expected, the range errors are at a low level when driving in the parking lot, except for satellite R17, whose elevation angle is under 5°. In contrast, range errors increase significantly when the vehicle was in the suburban area, even for signal azimuths without building blockage. While driving in the vegetation area, it appears that the signal blockage by the tree has limited impacts on the range errors of other tracked satellites.

To better understand the range errors under different environments, the whole trajectory of the smartphone data is classified into three scenarios, namely open sky, vegetation, and suburban, Table 3.3 summarizes the overall statistics of the range errors. It can be noted that, in the suburban environment, the mean values of range errors and corresponding standard deviations for P1 and P5 are significantly larger than that in open sky and vegetation, which is expected because of the signal blockage and higher-level multipath in the suburban. Under the vegetation environment, the range errors are slightly larger than those in the open sky and are consistent with the analysis above, for which the vegetation does not have a significant impact on range errors in comparison to suburban environment.

(a)

(b)

(c)

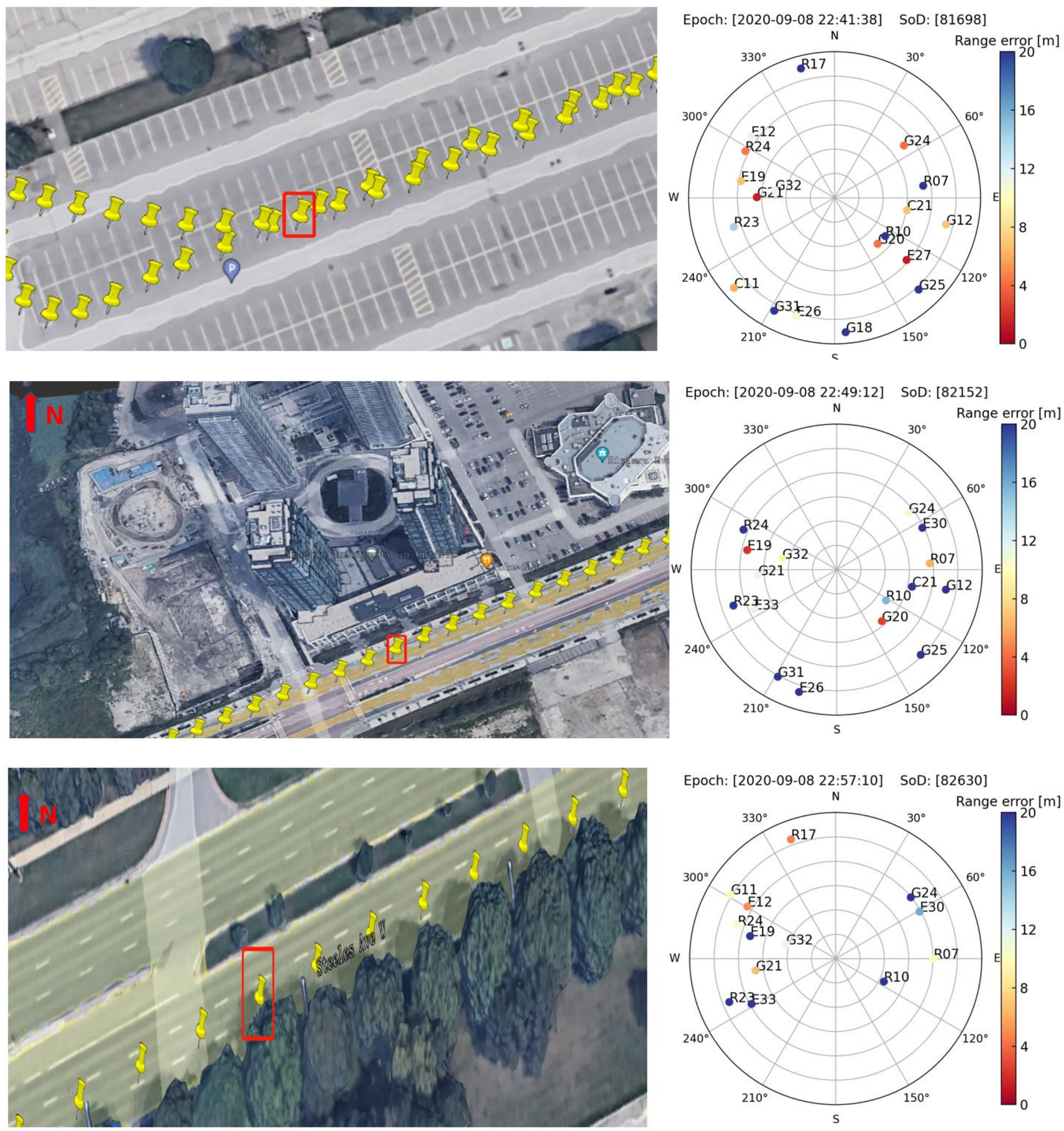

Figure 3.8 Sky plots of satellite range errors under (a) open sky, (b) suburban, and (c) vegetated environments.

Table 3.3 Frequency-specific statistics for satellite absolute range errors under open sky, suburban, and vegetation for all satellites (units: metre)

	P1				P5			
	Mean	Std Dev	95th percentile	Number	Mean	Std Dev	95th percentile	Number
Open sky	0.8	7.3	14.5	32267	0.9	2.4	5.1	14198
Suburban	2.2	9.4	18.2	1443	1.2	3.8	5.9	658
Vegetation	1.5	7.5	17.1	354	1.4	1.9	3.9	176

3.4.4 Correlation between range errors and pre-fit residuals

In smartphone GNSS data processing, quality control is vital and more challenging compared to geodetic data. Pre-fit outlier rejection is one effective quality control method. Therefore, in this subsection, the correlation between ranger errors and pre-fit residuals is assessed. As shown in Figure 3.9, different colours represent different satellites. It can be concluded that the range errors and pre-fit residuals for P1 have a higher correlation than P5, while the range errors and pre-fit residuals for P5 are at a lower level compared with P1. The reason for a higher correlation in P1 could be that the smartphone antenna is designed for the first frequency, and may not be optimized for other frequencies. Another reason might be that the correlation in P5 is hidden in the noise due to the same level of noise and pre-fit residuals. To further evaluate the correlation satellite-by-satellite, Figure 3.10 illustrates the relationship among correlation coefficient, elevation angle, and SNR, where each dot represents one satellite and different colours denote the corresponding SNR values. The correlation coefficients in Figure 3.10 are Pearson product-moment correlation coefficients, and are calculated satellite-by-satellite. With a lower elevation angle, the correlation coefficients tend to be smaller. Usually, GLONASS satellites have the highest correlation coefficients despite larger range errors. One possible reason is that, for other constellations, due to the high noise level itself for smartphones, the correlation between range errors and pre-fit residuals can be easily hidden within the noise; while there is a larger range error for GLONASS satellites, so the correlation can be more conspicuous. The results indicate that pre-fit residual rejection/de-weighting is worth further investigation and may provide potential solution improvement in future research, as it reflects the range errors with a high confidence level (Yi et al. 2024).

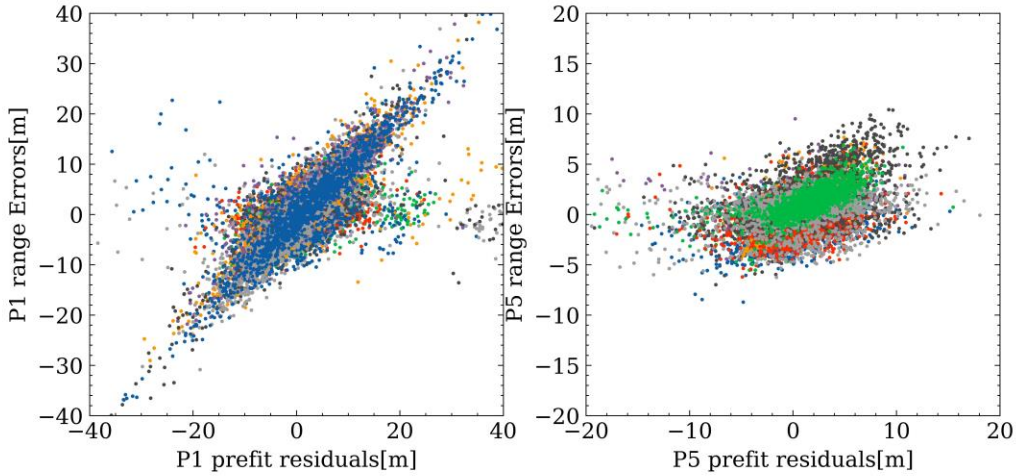

Figure 3.9 Correlation between range errors and pre-processed misclosures on P1 and P5. Different colours represent different satellites

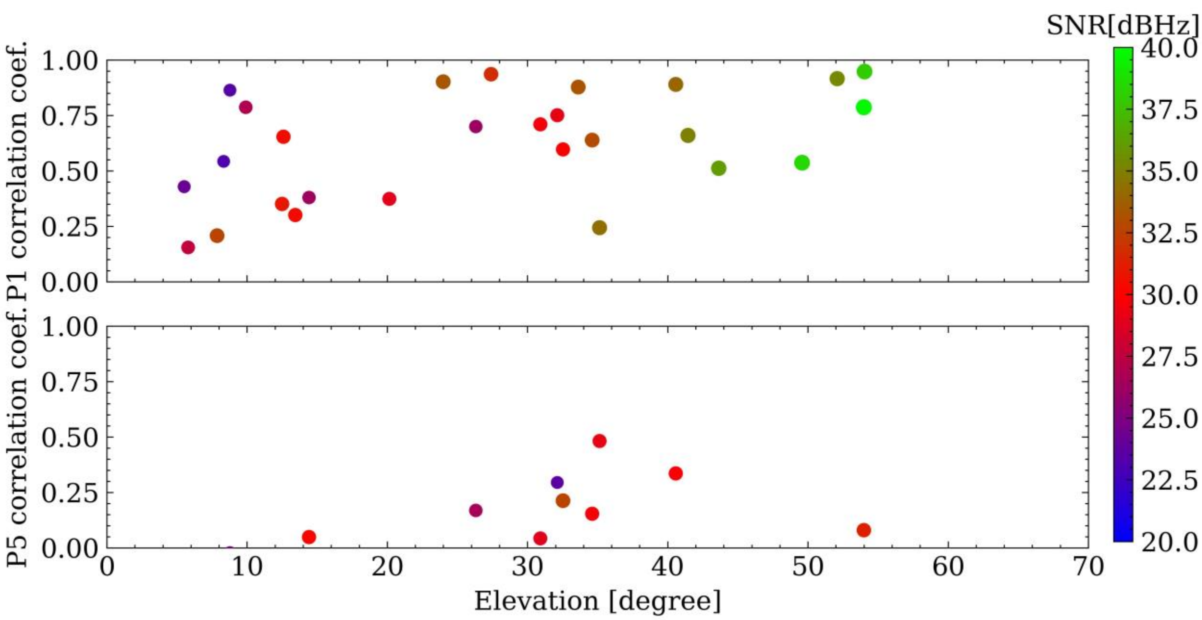

Figure 3.10 Correlation coefficients between range errors and prefit residuals, as well as the relationship among correlation coefficients, satellite elevation angle, and SNR values

3.4.5 Range error comparison on car dashboard and roof

In realistic application of smartphone positioning, drivers usually mount their devices on the dashboard for navigation or chatting purposes. However, much of the published research conducted experiments under open-sky environments or mounted smartphones on car roofs. Considering that the car roof may also influence the GNSS observation quality, this subsection assesses how the distribution of range errors will be affected when the smartphone is placed on the car roof compared to the car dashboard. Figure 3.11 depicts the probability distribution of range errors, in which the blue and green bins denote the range errors on the roof and dashboard, respectively. The standard deviation values of range errors on the car roof are 5.1 m and 5.3 m on the dashboard for P1, while they are 2.2 m and 2.4 m for P5, respectively. A more standard normal distribution for the range errors on the roof is observed compared to those on the dashboard from Figure 3.11, which infers that the GNSS observation quality is slightly better when the phone is placed on the car roof, and different code precisions may need to be applied when the smartphones are in different places of the car in the data processing. Normally, in user environments, it is not realistic to place the smartphone on the car roof. Therefore, when placing the smartphone in the car, the GNSS measurement processing strategy needs to be improved compared to the roof datasets.

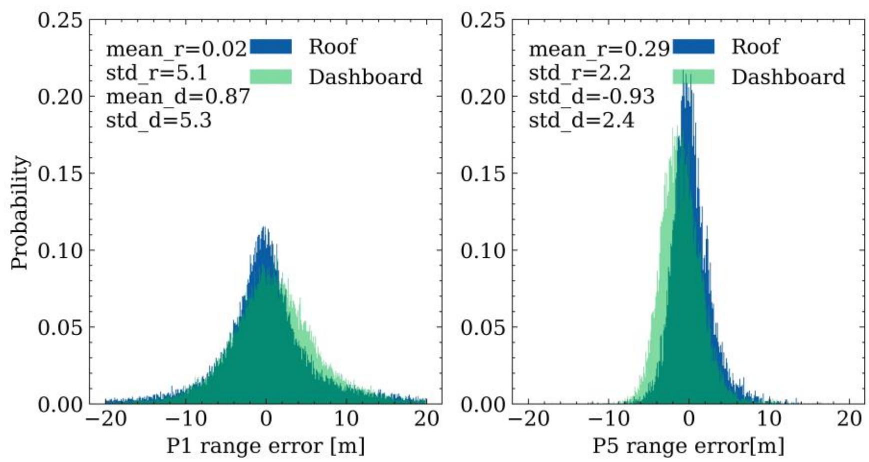

Figure 3.11 Range error distribution comparison for P1 and P5 when the smartphone is placed on the dashboard and roof

3.5 Summary

This chapter proposes a differencing method between a geodetic grade receiver and a smartphone with consideration of the lever arm, aiming to derive the actual range errors for smartphones under realistic usage. The methodology of the observation differencing was first introduced, along with several datasets collected, with the smartphone mounted on the car dashboard and roof. A comprehensive investigation and analysis are presented.

Firstly, question (1) proposed in Section 3.1 is addressed by assessing the distribution of the range errors and range error characteristics for the different constellations, and it is found that the range errors of smartphones on the first frequency are significantly larger than those of the third frequency, approximately ten times larger than a geodetic receiver/antenna. In addition, the range errors of GLONASS satellites have the largest standard deviation, with values of 11.8 m and 0.7 m for smartphone and geodetic receivers, respectively. For GPS, Galileo, and BDS, the smartphone standard deviation values of range errors are comparable.

Secondly, to answer question (2), the relationship among range errors, elevation angles, and SNR values is evaluated. Consistent with published research, the smartphone range errors are highly dependent on the SNR values, while the range errors of geodetic receivers are significantly correlated with satellite elevation angles. However, the trend on the third frequency is not as obvious as the first frequency, which is worth further investigation.

Thirdly, a vehicle trajectory is classified into different GNSS environments, namely open sky, suburban, and vegetation, to assess smartphone range error behaviors under different scenarios which is proposed in question (3). The results for the dataset analyzed indicate that range errors reach a peak in the suburban environment. While in the vegetated environment, the range errors are slightly larger compared to open-sky environments. Furthermore, for the data processed, the tree blockage seems to have little impact on affecting the measurement quality of other satellites.

Fourthly, a comparison between range errors and pre-fit residuals is carried out to address the question (4). A high correlation is found on the first frequency, while it is not significant for the third frequency. By computing correlation coefficient, it is observed that GLONASS measurements have larger correlation coefficients than others. The reason may be that, for other constellations, the correlation can be easily hidden in the observation noise, and it is similar when the third frequency appears to have a lower correlation. When evaluating the correlation satellite-by-satellite, lower elevation and lower SNR values can also cause a low correlation coefficient.

Finally, a range error comparison is conducted with the smartphone placed in different places. The results show that the standard deviation values of range errors for the first frequency are 5.1 m and 5.3 m on the roof and dashboard, respectively, and are 2.2 m and 2.4 m for the third frequency, indicating that GNSS signals are further suppressed and interfered when the smartphone is mounted on the dashboard.

This chapter provides a comprehensive assessment of the actual range errors for smartphones, and the results can further benefit the investigation on optimizing weighting schemes and quality control methods for future work, aiming for a higher level of smartphone positioning and application. The main purpose of this paper is to understand the actual range error distribution and characteristics; hence, some preliminary and commonly assessed performances are carried out first (e.g., relationship between range errors and SNR/elevation angle). However, the trends on different frequencies are slightly different, which can further be used to fit for the weighting schemes and residual rejection threshold functions. In addition, there are new and interesting findings for the range error characteristics under different environments and the correlations between range error and pre-fit residuals. These findings can potentially benefit smartphone positioning algorithm development. e.g., different code precision and different weight may be applied to different constellations and different frequencies based on the analysis, and the SNR mask and elevation cut-off angle can be adjusted with different datasets. In addition, regarding different range error behaviour under different environments, the weighting scheme considering different environments is worth investigating. Furthermore, the pre-fit residuals can partly reflect the range errors, different thresholds for pre-fit outlier rejection may be helpful according to this paper. Finally, different code precisions can also be applied when the smartphone is mounted in different places. The above-mentioned aspects are detailed developed in Chapter 5.

4 CYCLE SLIP DETECTION: IMPROVMENTS FOR SMARTPHONES

Due to the importance of cycle slip detection in GNSS data processing, this chapter investigates cycle slip detection methods using code-minus-phase, geometry-free, Melbourne-Wübbena combinations, and Doppler measurements. For smartphone applications, the limited dual-frequency measurements and metre-level pseudorange noise largely affect the performance of different cycle slip detection methods. For instance, the MW and GF methods are limited to dual-frequency measurements, and the CMP method is significantly affected by the noisy pseudorange measurements. To evaluate the performance of different cycle slip detection methods, the detailed derivations of the above four methods are provided first, and special modification is conducted based on the Doppler cycle slip detection method. The sensitivity of different cycle slip detection methods is analyzed with the error propagation law. With data collected in suburban environments, ten sets of cycle slips are simulated to assess cycle slip detection performance and to validate the proposed method. This work has been accepted for presentation at the *ION GNSS+ 2024* conference and it has won a best student paper award for the pending peer-reviewed proceedings.

4.1 Background and motivation

The key in processing phase measurements is the ambiguity parameter. To be specific, cycle slips are the main hurdle to fully exploiting the very precise carrier-phase measurements (Langley et al. 2017). A power loss, very low signal-to-noise ratio, failure of the receiver software, or malfunctioning satellite oscillator can each cause a cycle slip. And a cycle slip breaks the measurement continuity and causes a jump in the carrier-phase cycle count ambiguity, which manifested in the extended Kalman filter as the reset of an ambiguity variance. Therefore, an undetected cycle slip will result in an incorrect stochastic model in the EKF, and further degrades the solution. Fortunately, CS can be detected by application of the standard hypothesis testing theory.

The applicability of various cycle slip detection methods depends on receiver dynamics and measurement availability. For instance, polynomial fitting (Lichtenegger et al. 1990) and high-order differencing methods (Kleusberg et al. 1993) are usually used for static data, while methods such as the Melbourne-Wübbena and geometry-free combinations (Blewitt 1990) can be applied regardless of receiver dynamics (Bisnath 2000). CS detection algorithms have been adapted for smartphone measurements. Miao et al (2011) introduced an elevation-dependent weighting factor to the MW combination for a modified TurboEdit method, and Cai et al. (2013) used a combined sliding window to mitigate the influence of noisy code measurements. Xu et al (2020) utilized the time-differenced MW combination to estimate the smartphone position and clock change rates to detect cycle slips. However, the MW and GF methods require dual-frequency measurements, which are not available for some constellations (e.g., BDS and GLONASS for the Mi8 or S21 models) or are frequently lost in a real-world application. Therefore, single-frequency CS detection methods are commonly used for smartphone GNSS data. Two typical methods are the code-minus-phase and Doppler cycle slip detection methods (Li et al. 2022a). The Doppler cycle slip detection method compares the consistency of time-differenced carrier phase (TDCP) measurements and Doppler observations, and assumes consistent clocks for these two observables. Nevertheless, Zangenehnejad et al. (2022) used TDCP and Doppler measurements to estimate the clock drift and change rate, respectively. Results showed that for the Xiaomi Mi8 and Samsung S20 phones, the clock behaviours for TDCP and Doppler measurements are different. These results also indicate that the conventional Doppler cycle slip detection method cannot be used for these phones. The frequent loss of dual-frequency phase measurements prevents the use of the GF and MW methods. And the noisy smartphone pseudorange measurements will increase the noise level of CMP combination, which leads to insensitivity in detecting small cycle slips (e.g., less than 5 cycles in smartphone measurements.) which are below the noise level.

Due to the crucial role of cycle slip detection in smartphone positioning, especially for applications where smartphones are used within sky obstructed environments, it is necessary to investigate the applicability of cycle slip detection methods, as well as to find a solution to improve the conventional Doppler cycle slip detection method in smartphones. The contributions of this chapter are:

(1) Summarizing the commonly used cycle slip detection methods in smartphones, as well as analyzing the sensitivities of different cycle slip detection methods.
(2) While the conventional Doppler cycle slip detection method is not applicable for smartphones whose TDCP and Doppler measurements are inconsistent, this chapter proposes an improved Doppler cycle slip detection method to deal with the inconsistency problem.

4.2 Cycle slip detection methods

For cycle slip detection methods which only utilize raw GNSS measurements, the basic concept is to form combined measurements which contain the ambiguity parameters and other stable residuals. In this way, after time-differencing, the change in the combined measurements can indicate the occurrence of a cycle slip. In the rest of this section, the code-minus-phase method, geometry-free and MW combination methods, as well as Doppler cycle slip detection method are described, and the sensitivity of these methods is analyzed.

4.2.1 Code-minus-phase method

The code-minus-phase measurement is the differencing of pseudorange and carrier phase measurements on the same frequency, given by Equation (4.1):

$$CMP_j^s = P_j^s - L_j^s = 2\gamma_j I_1^s + (b_j^s + b_{r,j}) - \lambda_j (N_j^s + B_j^s + B_{r,j}) + \varepsilon_j^s - \xi_j^s \tag{4.1}$$

As shown in Equation (4.1), CMP measurements eliminate the geometry range and troposphere delay. It is usually used in single-frequency GNSS cycle slip detection. The time-differenced CMP measurement on the first frequency can be derived as:

$$\nabla_t CMP_1^s = 2\nabla_t I_1^s + \nabla_t (b_1^s + b_{r,1}) - \lambda_1 \nabla_t (N_1^s + B_1^s + B_{r,1}) + \Gamma_{CMP} \tag{4.2}$$

$$\Gamma_{CMP} = \nabla_t \varepsilon_1^s - \nabla_t \xi_1^s \tag{4.3}$$

where ∇_t denotes time-differencing, and Γ_{CMP} is the time-differenced noise of CMP measurement. What remains in the measurement is the ionospheric residuals and hardware biases, which are negligible especially for smartphone datasets with sampling rate of 1 Hz. The major limitation for application of the CMP method for smartphone GNSS measurements is the large code noise, which affects the detection performance when the cycle slip is small, e.g., several cycles.

4.2.2 MW method

The MW combination can form the wide-lane ambiguity using dual-frequency measurements without geometric range and atmospheric delays. Taking smartphone GPS L1 and L5 measurements as an example, the MW and time-differenced MW measurements can be derived as Equations (4.4)-(4.6).

$$MW_{15}^s = (f_1 L_1^s - f_5 L_5^s)/(f_1 - f_5) - (f_1 P_1^s + f_5 P_5^s)/(f_1 + f_5) \tag{4.4}$$

$$\nabla_t MW_{15}^s = \frac{c}{f_1 - f_5} \nabla_t (N_1^s + B_1^s + B_{r,1} - N_5^s - B_5^s - B_{r,5}) - \frac{f_1}{f_1 + f_5} \nabla_t (b_1^s + b_{r,1}) - \frac{f_5}{f_1 + f_5} \nabla_t (b_5^s + b_{r,5}) + \Gamma_{MW} \tag{4.5}$$

where Γ_{MW} is the time-differenced noise of MW combination, and

$$\Gamma_{MW} = \frac{f_1}{f_1 - f_5} \nabla_t \xi_1^s - \frac{f_5}{f_1 - f_5} \nabla_t \xi_5^s - \frac{f_1}{f_1 + f_5} \nabla_t \varepsilon_1^s - \frac{f_5}{f_1 + f_5} \nabla_t \varepsilon_5^s \tag{4.6}$$

The wide-lane wavelength for smartphones which is a combination of L1 and L5 is ~75 cm. Similarly, ignoring the temporal variability of phase and code hardware biases, the sensitivity of the MW method depends on the noise level of pseudorange noise. It is also worth noting that the MW method cannot detect cycle slips which are the same for both frequencies, e.g., five cycles on L1 and five cycles on L5.

4.2.3 Geometry-free method

To avoid the large noise of pseudorange measurements, the GF combination directly uses carrier phase measurements from two frequencies. For smartphone L1 and L5 dual-frequency data, the GF and time-differenced GF measurements are shown in Equations (4.7)-(4.9).

$$GF_{15}^{s} = L_1^s - L_5^s = (dt_{r1} - dt_{r5}) - (\gamma_1 - \gamma_5) I_1^s + (\lambda_1 N_1^s - \lambda_5 N_5^s) + (\xi_1^s - \xi_5^s) \tag{4.7}$$

$$\nabla_t GF_{15}^{s} = -(\gamma_1 - \gamma_5)\nabla_t I_1^s + \lambda_1 \nabla_t (N_1^s + B_1^s + B_{r,1}) - \lambda_5 \nabla_t (N_5^s + B_5^s + B_{r,5}) + \Gamma_{GF} \tag{4.8}$$

$$\Gamma_{GF} = \nabla_t (\xi_1^s - \xi_5^s) \tag{4.9}$$

Compared to CMP and MW measurements, the noise level of time-differenced GF measurements is significantly lower. The threshold of GF cycle slip detection is related to sampling rate due to the existence of time-differenced ionospheric effect parameter. One disadvantage of the GF method is its inability to detect certain cycle slip combinations, e.g., $\lambda_1 N_1^s = \lambda_5 N_5^s$.

4.2.4 Doppler cycle slip detection method

For cases where there is no available dual-frequency measurement, the time-differenced carrier phase and Doppler measurements are usually applied to detect cycle slip. The Doppler measurement can be presented as in Equation (4.10).

$$-\lambda_j D_j^s = \dot{\rho} + c(d\dot{t}_r - d\dot{t}^s) + \gamma_j \dot{I}_j^s + \dot{T}^s + \vartheta_j^s \tag{4.10}$$

where the dots signify time variability, i.e., time differentiation. The conventional Doppler cycle slip detection measurement is provided in Equation (4.11) and (4.12).

$$DopplerCS_j^s = \frac{\nabla_t L_j^s}{\lambda_j} + \frac{(D_j^s(t) + D_j^s(t-1))}{2} \cdot \Delta t = (\frac{c}{\lambda_j}\nabla_t dt_{r,j} + \nabla_t (N_j^s + B_j^s + B_{r,j})) - \frac{c}{\lambda_1} d\dot{t}_r + \Gamma_{dopplerCS} \tag{4.11}$$

$$\Gamma_{dopplerCS} = \frac{1}{\lambda_j}\nabla_t \xi_j^s + \frac{1}{2\lambda_j}\vartheta_j^s(t) + \frac{1}{2\lambda_j}\vartheta_j^s(t-1) \tag{4.12}$$

Normally, the time-differenced carrier-phase receiver clock offset should be synchronized with the Doppler clock drift, and therefore, the difference between TDCP and Doppler should be close to zero. However, it was found in Zangenehnejad et al. (2022) that the clocks on phase and Doppler measurements are not consistent for some smartphones (e.g., Xiaomi Mi8 and Samsung S21), as illustrated in Figure 4.1. For satellites G01, C34, E02, and R14, both TDCP (in blue and orange for L1 and L5, respectively) and Doppler (in green and red) measurements are plotted in Figure 4.1, and in principle, these two measurements on the same frequency should be overlapped, i.e., blue dots should be the same as green ones. However, it can be concluded from Figure 4.1 that, (i) for all constellations, the TDCP and Doppler clocks are not synchronized, resulting in the non-applicability of conventional Doppler methods for cycle slip detection, and (ii) for TDCP measurements, there are two significant segments (e.g., two blue and two orange lines) which are caused by frequent receiver clock jumps. The reason why they appear to look like two lines in Figure 4.1 is that the dots are used in the plotting instead of lines, as the lines would result in one big wide line which would make the results appear ambiguous.

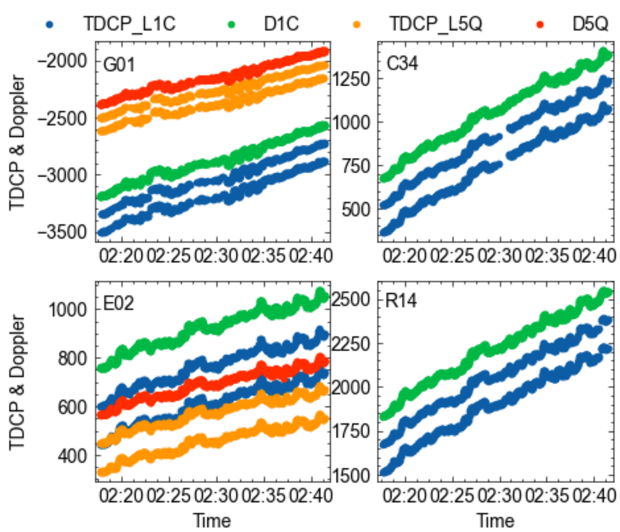

Figure 4.1 Time series of time-differenced carrier phase (blue and orange) and Doppler (green and red) measurements on L1 and L5 for satellite G01, C34, E02, and R14 collected by a Xiaomi Mi8 phone.

The solution to this issue is to mitigate the effect of receiver clock jumps and the inconsistency. The first possible solution is to form single-differenced Doppler cycle slip test values with Equation (4.11). However, it is hard to guarantee that there are no cycle slips on the selected reference satellite measurements, especially for single-frequency observations. In this study, for each constellation, the median values of Doppler test values on the same frequency are calculated first as the datum for cycle slip detection thresholds. The reason why the average value is not adopted is that it is easily affected by large values. Therefore, the modified Doppler cycle slip detection test values can be regarded as a mean shift model, as Equation (4.13), and the hypothesis test can be given as Equation (4.14).

$$E(DopplerCS_j^s) \sim N(median_j, \Gamma_{dopplerCS}) \tag{4.13}$$

$$\begin{aligned} H_0 &: abs(DopplerCS_j^s - median_j) \le k\Gamma_{dopplerCS} \\ H_1 &: abs(DopplerCS_j^s - median_j) > k\Gamma_{dopplerCS} \end{aligned} \tag{4.14}$$

where H_0 represents there is no cycle slip detected, and H_1 is the alternative hypothesis. k is the scale factor and can be calculated with a given confidence level (e.g., 2 for 95%, and 3 for 99.7%). $median_j$ is the constellation and frequency-specific median of $DopplerCS$ values. The reason for constellation-specific calculation is that it is stable within each constellation, and the detailed reason is provided in Section 4.4.1.

4.2.5 Sensitivity analysis for CS detection methods

Due to the residuals remaining in the cycle slip detection test values and the noise level differ for different methods, the sensitivity varies. Therefore, it is necessary to analyze the detection sensitivity in principle. For smartphone L1 and L5 measurements, cycle slips of 1 cycle for N_1 and N_5 will lead to different test value changes. Table 4.1 summarizes the changes of test values when there is 1 cycle of CS on L1 and L5, respectively, as well as the noise level. The detection thresholds used in this study is also provided. For the calculation of noise levels, the error propagation law is applied to Equations (4.3), (4.6), (4.9), and (4.12). σ_P, σ_L, and σ_D are the noise of pseudorange, carrier phase, and Doppler measurements, respectively. Typically, for smartphone datasets, σ_P is several metres, σ_L is around 1 cm, and σ_D is near 1 cycle, as the noise level for smartphone are usually several metres according to Chapter 3, and the phase precision is usually 1/100 of pseudorange measurements. According to Table 4.1, the CMP and MW methods are not able to detect small cycle slips when the pseudorange noise is large. On the contrary, GF and Doppler methods are sensitive to small cycle slips; however, the sensitivity is correlated with sampling rate because of the ionospheric residuals in ∇GF_{15}^{s} and Δt in $DopplerCS_{j}^{s}$.

Table 4.1 Sensitivity of one cycle jump on N1 and N5, as well as noise level for different cycle slip detection methods

	Test value change (1 cycle for N_1)	Test value change (1 cycle for N_5)	Noise Level	Thresholds
CMP	$\lambda_1 \approx 0.19$ m	$\lambda_5 \approx 0.255$ m	$\sqrt{2}\sigma_P$	10 m
MW	$\frac{c}{f_1 - f_5} \approx 0.751$ m	$\frac{c}{f_1 - f_5} \approx 0.751$ m	$0.714\sigma_P$	5 m
GF	$\lambda_1 \approx 0.19$ m	$\lambda_5 \approx 0.255$ m	$2\sigma_L$	0.1 m
Doppler	1 cycle	1 cycle	$\Delta t \sigma_D$	1 cycle

4.3 Dataset and experiment setting

To validate the cycle slip methods performance in a realistic driving situation, smartphone data collected in suburban environments are used. The data were collected in and around York University, Toronto, Canada on 8th, November 2022, with a Mi8 phone mounted on a car dashboard. The trajectory is illustrated in Figure 4.2.

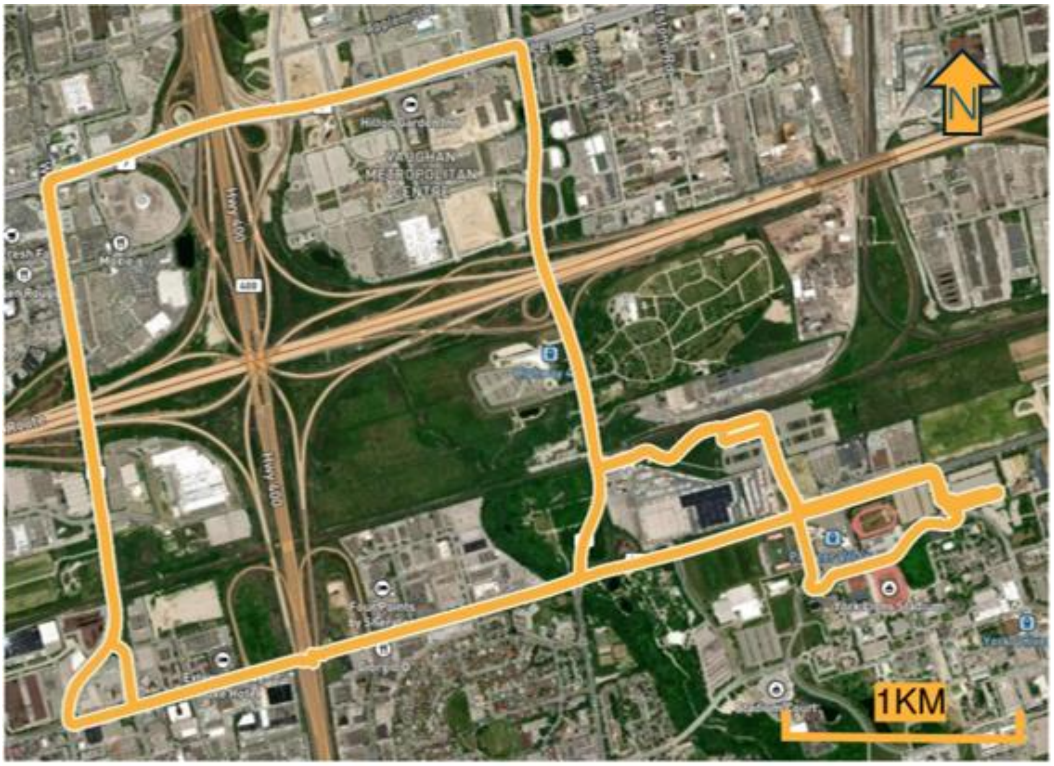

Figure 4.2 Smartphone data collection trajectory in and around York University, Toronto, Canada on 8th, November 2022, with a Mi8 phone mounted on a car dashboard.

An ideal way to assess different methods with various cycle slip scenarios is to simulate the cycle slips, in which the "true" cycle slip values and the occurrence can be used as reference. The premise is to select a period without cycle slip for one satellite, and manually "inject" cycle slips to the clean data. Figure 4.3 shows the time series of MW, CMP, and GF combinations for satellite E02. The dual-frequency phase availability indicators are also provided in the bottom sub-plot, where the dots indicate dual-frequency phase measurements gaps. Two significant jumps can be noticed for the MW and GF combination at around 02:23 and 02:27, which are cycle slips on either L1 or L5. From Figure 4.3 the time periods between 02:23 and 02:36 are selected as "clean" data for further analysis.

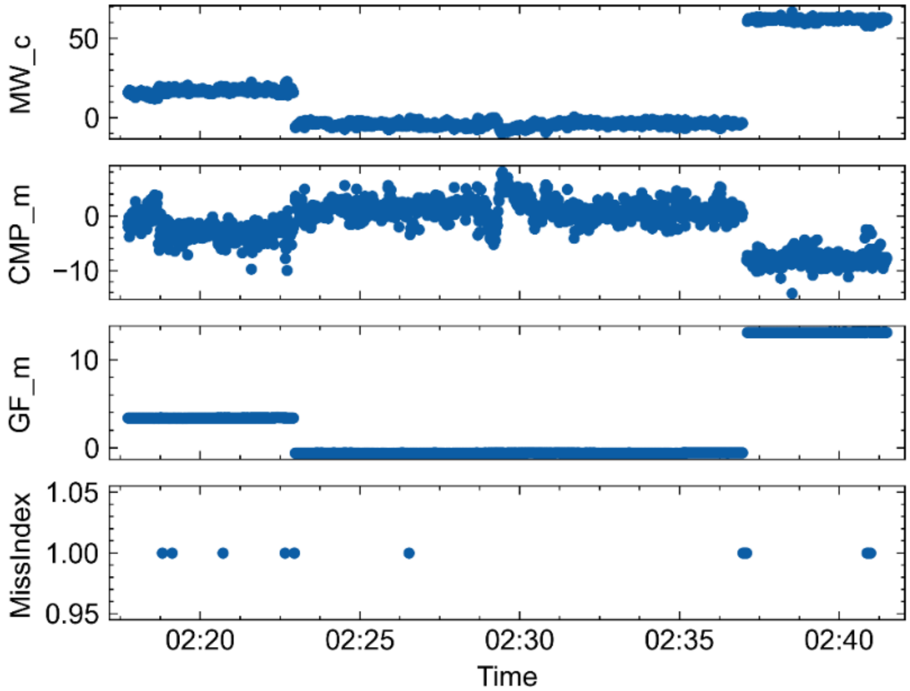

Figure 4.3 Time series of undifferenced MW, CMP, and GF cycle slip indicators for satellite E02

Table 4.2 Summary of simulated cycle slips for satellite E02 (units: cycle)

Index	Epoch	Simulated CS on L1	Simulated CS on L5
1	02:24:01	1	0
2	02:25:01	5	0
3	02:26:01	10	0
4	02:27:01	0	1
5	02:28:01	0	5
6	02:29:01	0	10
7	02:30:01	1	1
8	02:31:01	5	5
9	02:32:01	10	10
10	02:33:01	67	50

Ten different cycle slip sets are simulated in this study, as summarized in Table 4.2. The cycle slips are simulated every minute. Firstly, one/five/ten cycles are added to L1 and L5, respectively, to evaluate the sensitivity of different methods. Secondly, simultaneous jumps are injected, with a specific set of 67 and 50 cycles (exactly the ratio of wavelengths for L1/L5), to compare the performance of MW and GF methods. The simulated cycle slips were used to validate and test the algorithms rather than using real data, because with simulated cycle slips, more sources testing can be done and for specific cycle slip pairs can be formed, e.g., 67:50. And these simulated cycle slip combinations represent some of the most difficult combinations to detect.

4.4 Results

This section begins with the discussion on the conventional cycle slip detection methods, especially for the Doppler cycle slip detection. Also, an analysis of the inconsistencies between receiver clock jumps and Doppler clock drifts is carried out. The CMP values for only L1 are calculated, because if the dual-frequency phase measurements are available, the MW and GF methods are more reliable.

4.4.1 Cycle slip indicators for all satellites

With Equations (4.2), (4.5), (4.8), and (4.11), the cycle slip indicators for different methods can be calculated. Figure 4.4 shows the time series of test values for all satellites (absolute values for GF, MW, and CMP), and satellites are represented by different colours. Those with large test values are obvious cycle slips in Figure 4.4, and most of the time-differenced GF measurements are below 0.5 metres. While for TD MW measurements, they are at metre-level. With the introduction of pseudorange measurements, the TD CMP measurements are the noisiest among all test values. For conventional Doppler methods, for both L1 and L5 frequencies, there are two major lines, respectively, due to the frequent clock jumps in phase measurements, the detailed reason has been stated in Section 4.2.4. This result is consistent with the noise level derived in Table 4.1.

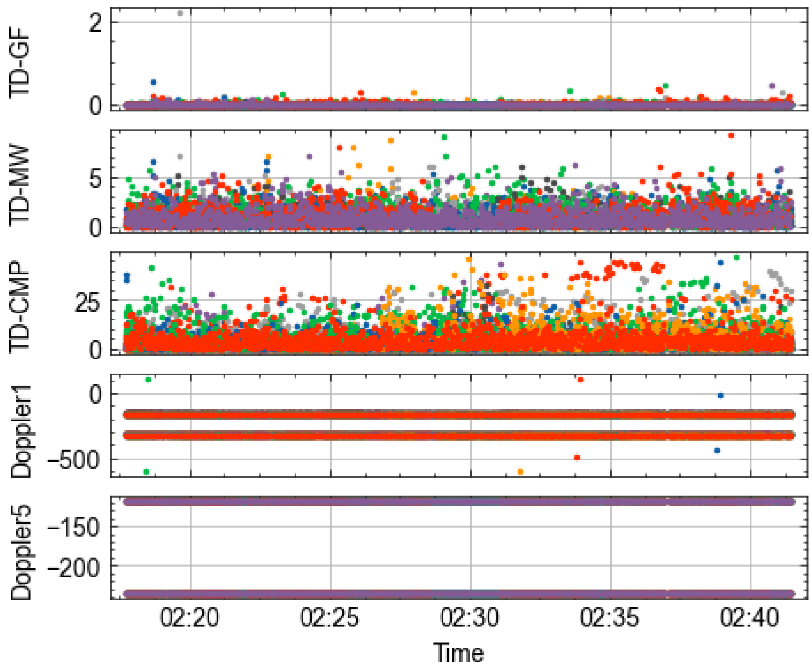

Figure 4.4 Time series of GF, MW, CMP, and conventional Doppler cycle slip absolute test values for all satellites. Different colours represent different satellites

However, it is important to mention that for the conventional Doppler cycle slip detection method shown in Figure 4.4, with a given threshold, e.g., 10 cycle, almost all of the epochs will be false detected as cycle slips, which will result in resetting of ambiguity parameter variances every epoch. With initialization per epoch, the solution will be degraded as a single-epoch solution and lead to a worse positioning performance. On the other hand, some smartphone users might choose to turn off the Doppler cycle slip detection, which might work well for dual-frequency measurements. Though, for single-frequency measurements, if only the CMP method is utilized, the large noise level infers insensitive detection for small cycle slips. Consequently, the undetected cycle slips will bias the solution.

To characterize the different clock behaviours for phase and Doppler measurements, Figure 4.5 provides zoom-in plots of TD Doppler cycle slip detection measurements on the first frequency for GPS, GLONASS, Galileo, and BDS, respectively. The ranges are set to (-162, -154) and (-320, -310) to have a clear view of the two major segments in Figure 4.4. The GPS and Galileo values are overlapped, and therefore, there is no orange line in Figure 4.5. Even though frequent clock jumps are observed for the phase measurements, the jump amplitudes seem to be stable. Moreover, the noise level of GLONASS satellites is higher than for other constellations. Results in Figure 4.5 indicate a constellation stability of the test values even with the jumps. Also, these results demonstrate the correctness of the proposed Doppler cycle slip detection method: the test values of Doppler cycle slip detection method for certain smartphone chipsets follow a mean shift normal distribution, and for each constellation and frequency, the corresponding median Doppler test values are the mean value of the normal distribution model.

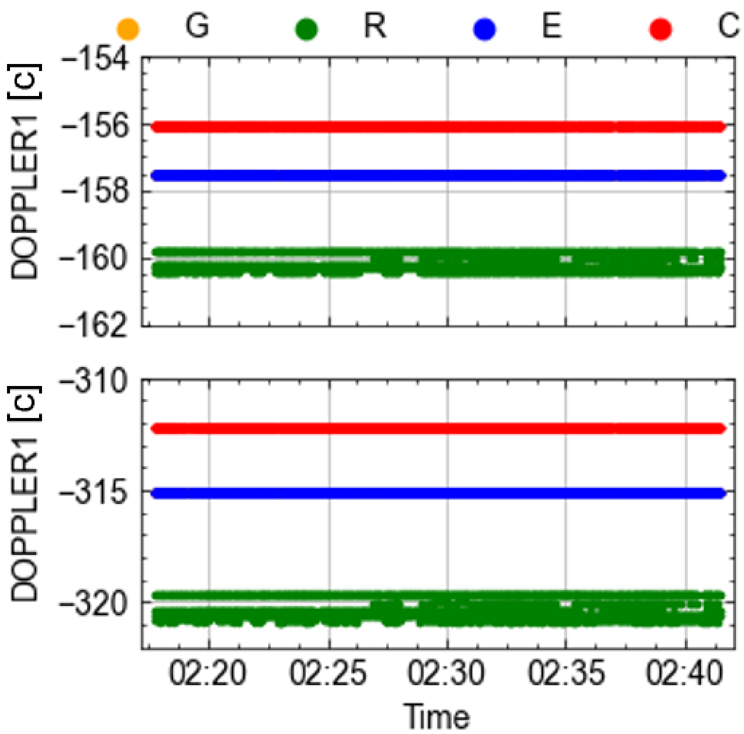

Figure 4.5 Time series of zoom-in Doppler cycle slip detection measurements on L1 for GPS, Galileo, GLONASS, and BDS. Each colour denotes a constellation, results for GPS and Galileo are overlapped

4.4.2 Validation of proposed Doppler cycle slip detection method

The assessment of the sensitivity and applicability of the GF, MW, CMP, and proposed Doppler cycle slip detection methods are carried out with the simulated cycle slips in Table 4.2. The time series of test values are provided in Figure 4.6. The red dash lines are the thresholds for cycle slip detection and the grey dash lines are the simulated epochs. For values beyond the dash lines, they are detected as cycle slips. The first conclusion from Figure 4.6 is that the proposed Doppler cycle slip detection method is effective in dealing with the inconsistent clocks for phase and Doppler measurements. The CMP method is only applied to L1, and therefore, any cycle slips on L5 cannot be detected with L1 CMP method.

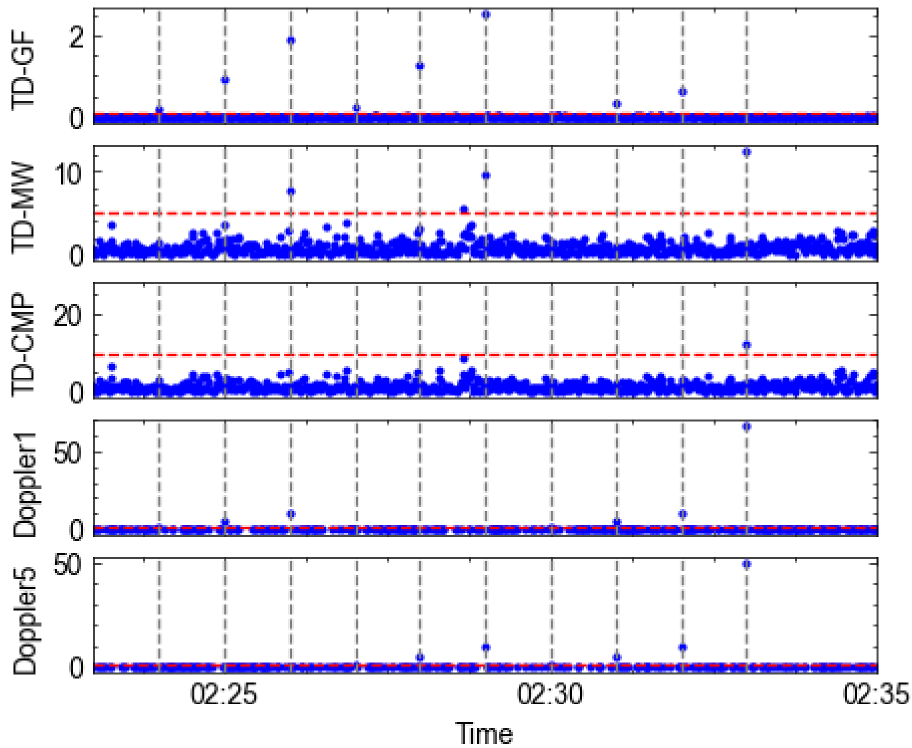

Figure 4.6 Time series of GF, MW, CMP, and modified Doppler cycle slip indicators after inserting simulated cycle slips. Grey dash lines are the labels of the epochs with simulated cycle slips, red dash lines are the thresholds for the cycle slip detection.

Due to the large, simulated cycle slips at 02:33:01, the scale for the Doppler methods in Figure 4.6 is too large to depict the smaller jumps. Hence, Figure 4.7 provides them with a smaller scale. From Figure 4.6 and Figure 4.7, the GF method and Doppler methods are the most sensitive, while for MW and CMP methods, due to the large noise of pseudorange measurements, small cycle slips cannot be detected. Moreover, the noisy code measurements will possibly lead to a false detection. e.g., during 02:28-02:29, there are two dots which are close to and even exceed the thresholds for the MW and CMP methods, respectively. This situation is likely caused by the big range error of the pseudorange on L1. For the proposed Doppler cycle slip detection method, all the simulated cycle slips are detected.

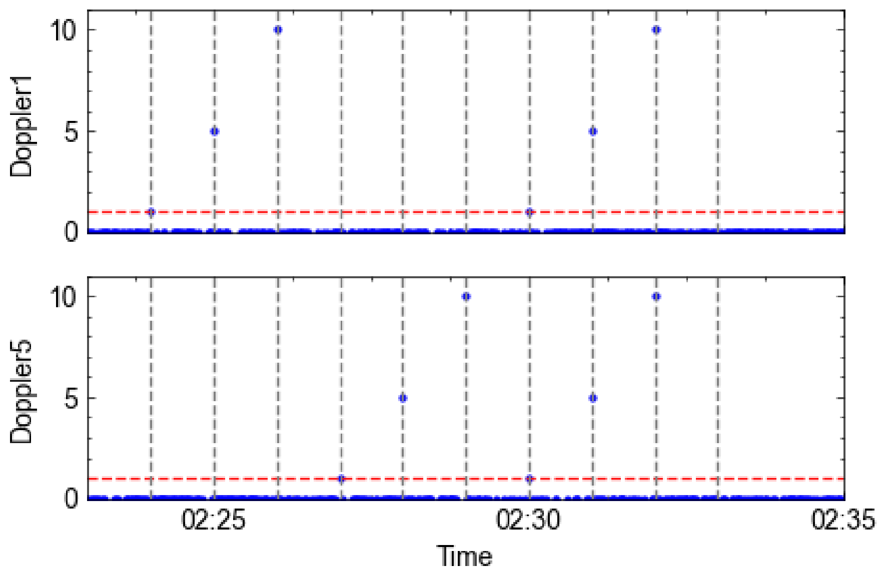

Figure 4.7 Time series of zoom-in modified Doppler cycle slip detection indicators on L1 and L5 after inserting simulated cycle slips

Figure 4.8 illustrates the detection performance of each simulated setting for different methods. A dot denotes that the simulated cycle slip is detected. Table 4.3 also summarizes the simulated cycle slip numbers and the detectability, with the √ denoting a detected cycle slip. For the CMP method (indices 4, 5, and 6 are not applicable due to the different frequencies), only index 10 is detected, which indicates that the CMP method is not able to detect cycle slips which are smaller than 10 cycles. For the GF method, cycle slip sets of (1, 1) and (67, 50) are not detected. The reason being that the cycle slip ratios are close or equal to the ratio of wavelengths for L1/L5, as discussed in Section 4.2.3. Using pseudorange measurements to form MW results in miss detecting cycle slips which are smaller than 5 cycles, but it is not applicable to the case where the cycle slips are the same on different frequencies. For dual-frequency measurements, a combination of the MW and GF methods can detect most of the cycle slips. Among all the methods, the proposed Doppler cycle slip detection method performs the best, with all the simulated cycle slips detected. In realistic smartphone data processing, the combination of these methods is recommended.

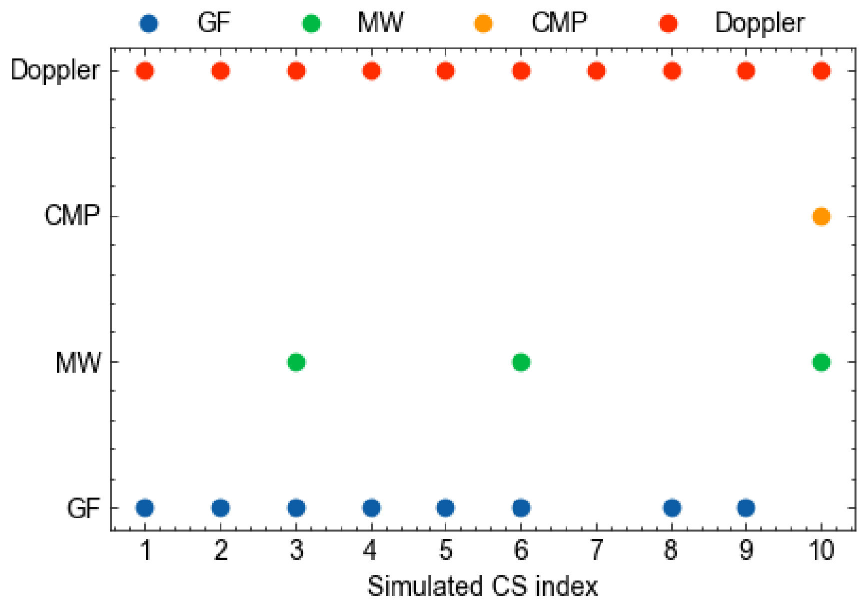

Figure 4.8 Cycle slip detection performance with different methods. A dot means a detected cycle slip, different colours are used to represent different methods

Table 4.3 Performance of detection performance of GF, MW, CMP, and modified Doppler cycle slip detection methods for ten sets of simulated cycle slips

Index	Time	Simulated CS on N1	Simulated CS on N5	GF	MW	CMP1	Doppler
1	02:24:01	1	0	√	×	×	√
2	02:25:01	5	0	√	×	×	√
3	02:26:01	10	0	√	√	×	√
4	02:27:01	0	1	√	×	×	√
5	02:28:01	0	5	√	×	×	√
6	02:29:01	0	10	√	√	×	√
7	02:30:01	1	1	×	×	×	√
8	02:31:01	5	5	√	×	×	√
9	02:32:01	10	10	√	×	×	√
10	02:33:01	67	50	×	√	√	√

4.5 Summary

The derivations of different cycle slip detection methods and the theoretical noise level corresponding to various methods have been provided. The time series of cycle slip indicators have been evaluated, and the results show that the noise level of CMP measurements is the highest, followed by the MW combination, and the GF combination is most sensitive to cycle slips. With conventional Doppler cycle slip detection method, there are two obvious segments caused by the clock inconsistency between TDCP and Doppler measurements and the frequent clock jump for phase measurements, and the inconsistencies varies for different constellation and frequencies. Consequently, the conventional Doppler cycle slip detection method cannot be used in such smartphone datasets.

With a selected “clean” data period for satellite E02, ten different cycle slips have been simulated and injected to the raw phase measurements. The CMP, GF, MW, and proposed modified Doppler cycle slip detection methods have been applied to detect these simulated cycle slips. Results show that for cycle slips smaller than 10 cycles, CMP method is not able to detect, while the MW method is partially sensitive to the cycle slips. However, due to the large noise on pseudorange measurements, the MW method miss-detects cycle slips smaller than 5 cycles. The GF method is sensitive to small cycle slips; however, cycle slip sets of (1, 1) and (67, 50) are not detected, the reason being that the cycle slip ratios are close or equal to the ratio of wavelengths for L1/L5. The proposed modified Doppler cycle slip detection method can detect all the simulated cycle slips, indicating it the best performer amongst the four methods. Theoretically, the proposed method could improve the smartphone positioning performance once the cycle slips are correctly detected, and may also contribute to smartphone ambiguity resolution.

Smartphone cycle slip detection remains a vital component in the filtered GNSS solution and needs to be continuously investigated and improved. Although the results in this chapter show that the proposed method has the best performance, it is not applicable to the situation where only one phase measurement is available for one constellation in one epoch. Moreover, the cycle slip detection thresholds are relatively small in this chapter, and in urban environments, the thresholds need to be adjusted. A larger threshold might lead to the miss-detection, while a smaller one would result in the false detection, the balance between the detection sensitivity and positioning performance would be an interesting research topic in future research. For instance, under complex environments, the noise level of phase measurements would increase with horizontal positioning accuracy of sub-metre-level. Whether there is a significant impact in position solutions when the cycle slips are small (e.g., less than 5 cycles) still needs to be investigated. If the position solutions are not sensitive to small cycle slips, then the thresholds for cycle slip detection methods can be set to a larger number.

5 QUALITY CONTROL: IMPROVED STOCHASTIC MODELLING AND OUTLIER DETECTION TO ENHANCE SMARTPHONE POSITIONING PERFORMANCE

So far in this dissertation, smartphone GNSS range errors and cycle slip detection methods have been developed. With the understanding of smartphone range errors, as discussed in Chapter 3, a more realistic weighting function can be formulated considering the correlation between range errors and SNR values. As part of quality control, stochastic modelling and outlier detection methods are discussed in this chapter. Aiming to achieve stable sub-metre-level horizontal positioning performance with smartphones, a GNSS stochastic model which contains a novel adaptive a priori phase/code ratio and weighting scheme is designed and tested. A new residual rejection method is proposed to identify measurement outliers, considering both SNR and the number of rejected measurements. The detailed mathematical model, stochastic model, and residual rejection approach are proposed, followed by a description of the dataset used and processing strategies. The effect of phase/code precision ratio on positioning performance is then analyzed. A discussion on the fitted weighting scheme functions is carried out, in which an over-optimistic issue is highlighted for the third frequency. With datasets collected in suburban environments, the proposed phase/code precision ratio scheme is validated. Dividing the datasets into training (for model building) and test (for algorithm validation) subsets, the fitted weighting scheme and proposed outlier detection method is assessed and validated step-by-step using the horizontal positioning errors. This work has been published in Hu et al. (2024).

5.1 Background and motivation

Regardless of the positioning methods used in smartphone positioning and navigation, the solution performance is highly dependent on stochastic model and quality control methods, especially in moderately urban or urban environments where GNSS signals are obstructed and prone to multipath interference. Regarding the stochastic model, appropriately assigning weights to each measurement in the filter is the premise for generating high-precision results. It primarily involves weighting the code and phase measurements from the same satellite and assigning weights to observations from different satellites using different indices. The investigation of stochastic models often focuses on weighting different satellites. Carrier-to-noise power density ratio has been identified as more correlated with smartphone multipath than elevation angles (Banville et al. 2019; Zangenehnejad and Gao 2021), and weighting schemes based on SNR have been proposed and optimized (Shinghal and Bisnath 2021). Sui et al. (2022) analyzed the pseudorange noise using code-minus-phase measurements and estimated coefficients in the conventional C/N_0-based weighting scheme, and the estimated coefficients were validated with SPP and RTK. By deriving code residuals with a short-baseline single-difference method (Zhang et al. 2018a), Wang et al. (2023) calculated smartphone-specific C/N_0-based function coefficients for each constellation. The fitted weighting scheme demonstrated sub-metre-level positioning accuracy with smartphones in a playground with atmospheric constraints, but there is a concern that the fitted function on L5 is over-optimistic compared to L1, i.e., far more weights may be put on L5 than L1 which is not realistic. Similarly, with the code multipath and noise (CMN) derived in an open sky area, Li et al. (2022b) found that CMN is correlated with both elevation angle and C/N_0. Consequently, they proposed a weighting scheme considering both indices, and the PPP results can be improved by 24% in open-sky area and 26% in a constrained visibility area. However, in a complex environment, the correlation between CMN and elevation angle is limited, leading to low applicability.

The relative weight between phase and code measurements is usually empirically determined as part of the stochastic model. The open-source RTKLib (https://www.rtklib.com/) GNSS measurement processing software adopts a precision ratio of 1:100 for code and phase, respectively, with a carrier phase error standard deviation of 3 mm for geodetic receivers. Moreover, the ratio on L5 is set to be smaller, representing a higher code precision on L5. However, for low-cost receivers and smartphones, the code error standard deviation is higher. Everett et al. (2022) suggested adjusting the ratio from 1:300

to 1:100 for L5 when the receiver grade changes from low-cost to smartphone. It is worth noting that the research on the code/phase precision ratio is still based on empirical values and needs further investigation.

In terms of quality control indicators, both a priori (aka pre-fit) and a posteriori (aka post-fit) residual rejection are normally applied in data processing to filter outliers. A priori residuals are highly related to the mathematical model used and a priori estimates. In contrast, the a posteriori residuals output from sequential least square or extended Kalman filter, are more correlated with code noise (Yi et al. 2024). Several statistical testing methods such as solution separation (SS) and detection, identification, and adaption (DIA) are commonly used in geodetic-grade receivers (Odijk and Verhagen 2007; Joerger M et al. 2016; Teunissen 2017). For multiple outliers, DIA can be applied in an iterative manner until no outliers are detected, and DIA procedures are normally adopted as standard outlier detection procedures. In most existing literature, a fixed threshold is applied in detecting possible outliers, which could limit the broad use of residual rejection in varied applications and environments (Bisnath and Aggrey 2024). Shinghal and Bisnath (2021) adopted an empirical value to reject measurements larger than the given threshold. For RTKLib PPP processing of smartphone data (Everette et al. 2022), residuals larger than four times the a posteriori variance will be rejected. Yi et al. (2024) proposed a smartphone residual rejection threshold scheme as a function of an adaptive factor and a constant value to accommodate the situation where phase measurements are missing. Moreover, a chi-square test is also widely performed on the test of residual statistics in GNSS fault detection (Brodie 2001).

With research in Chapter 3, actual smartphone range errors were estimated using a collocated geodetic receiver in suburban driving environments, providing an opportunity for an in-depth study to improve smartphone positioning performance further. Building on insights gained, this chapter contains an investigation in the feasibility of achieving sub-metre-level smartphone positioning accuracy with raw GNSS measurements in realistic driving environments. This performance will be achieved through (i) the optimization of the phase/code precision ratio, (ii) weighting scheme, and (iii) a posteriori residual rejection.

The novelty of this research can be concluded in the following aspects. (1) While most of existing research are focusing on improved stochastic modelling by proposing new weighting schemes, the current research proposes an adaptive phase/code precision ratio as a function of the observed number of epochs. (2) For fitted weighting scheme functions based on correlation between multipath/residual/range errors and C/N_0 values, this research finds that there is an over-optimistic issue on GPS L5 and Galileo E5a, and a scale factor is proposed to deal with this issue. (3) The third novelty lies in adaptively determining the threshold values for residual outlier detection according to the SNR values and number of rejected measurements, whereas a fixed or empirical rejection threshold is utilized in most of existing research. Despite similar procedures in DIA in which the outliers are first detected, and then identified, this contribution uniquely adopts an adaptive threshold in rejecting measurements.

5.2 Methodology

This section starts with a detailed description of the proposed stochastic model, which combines an a priori adaptive phase/code precision ratio and weighting schemes. An improved a posteriori residual rejection method is introduced. The mathematical model of UDUC PPP is given in Equation (2.2). The SNR in this Section means signal strength derived from RINEX observation files.

5.2.1 Smartphone PPP stochastic model

Assigning proper weights to different measurements is of vital importance in EKF. The stochastic model mainly comprises two aspects: one is to set the a priori precision ratio between pseudorange and phase observations, and the other is to weight the measurements among different satellites with a specific criterion, e.g., elevation angle or SNR value.

5.2.1.1 A priori adaptive phase/code precision ratio

Due to the carrier phase wavelength being shorter than the code chip length, the precision of phase measurement is generally much higher than that of the code, leading to a higher weight on the carrier phase. However, ambiguity parameters in the phase measurement are slowly converging in EKF state estimation. The equivalent ranges resolved from phase measurements become increasingly precise during this convergence period. Once the ambiguity standard deviations converge to the millimetre or centimetre level, the phase measurements can be regarded as pseudoranges with millimetre/centimetre-level precision. Figure 5.1 provides an example of the influence of phase/code ratios on horizontal positioning performance. The results are generated using dataset collected in and around York University. The precision ratio between phase and code measurements has a significant impact on the positioning error time series, highlighting the importance of improving the strategy of setting the ratio. A higher weight on the phase sometimes has larger positioning errors during convergence time, as seen during 02:23~02:26, where a larger ratio leads to larger positioning errors. In contrast, it performs better when the ambiguities converge, as observed after 02:26. Taking the blue line as an example, during the convergence, due to a higher ratio on pseudorange, the positioning error is the smallest. However, when the ambiguity terms converge to a higher precision along with the processing, the performance gets worse, and a higher weight on the phase measurements (other colour) outperforms the ratio of 100. Therefore, an adaptive phase/code precision ratio is proposed first in this study, aiming to combine the advantages of different ratios.

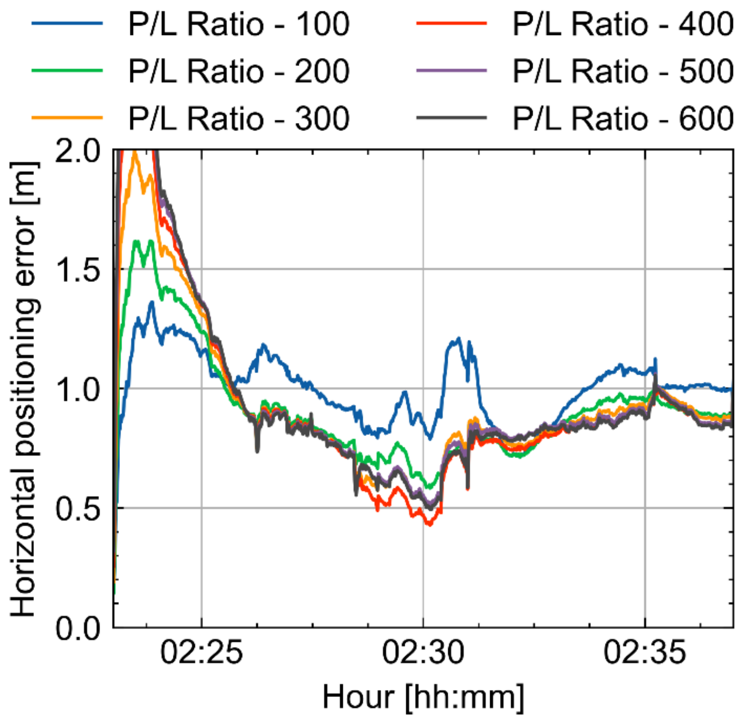

Figure 5.1 Example of influence of phase/code precision ratio on horizontal positioning errors. Different colours denote different phase/code ratios.

Starting from the commonly used ratio of 1:100, the weight on phase is increasing with the number of continuously observed epochs. An adaptive ratio as a function of continuously observed epochs is proposed as:

$$r_a = \begin{cases} \dfrac{1}{100 + (500 / arc_{\max}) \cdot n_{epo}} & , \quad 0 < n_{epo} \le arc_{\max} \\ \dfrac{1}{600} & , \quad n_{epo} > arc_{\max} \end{cases} \tag{5.1}$$

Considering a smartphone code precision of 3.5 m (Hu et al. 2023b) used in this study and an optimal phase precision two times that of a geodetic-grade receiver (3 mm for geodetic-grade receiver), the ratio cut-off is set to 0.006/3.5, approximately 1:600. In Equation (5.1), n_{epo} is the number of continuously observed epochs, and it is counted per frequency and satellite. $arc_{\max}$ is the number of epochs needed for ambiguities to converge to cm-level or mm-level. In this study, it is empirically set to 300, which is about 5 min with a sampling rate of 1 s. $arc_{\max}$ should be adjust according to different sampling rates and positioning methods, e.g., for PPP-RTK, the parameters converge more quickly, and therefore, $arc_{\max}$ should be smaller.

5.2.1.2 Weighting schemes

Using different indicators to infer the a priori measurement quality results in various weighting schemes. Two major indicators are the satellite elevation angle and SNR. In a geodetic-grade receiver, the measurement quality is more correlated with elevation angle, and one commonly used elevation-dependent weighting function is given as:

$$\sigma_{ele}^2 = (a_{ele}^2 + \frac{b_{ele}^2}{\sin^2 ele}) \tag{5.2}$$

where σ_{ele}^2 is the measurement variance, a_{ele}^2 and b_{ele}^2 are constants which reflect the unit weight mean square error of measurements, el is the satellite elevation angle. Compared to the elevation-dependent weighting used in geodetic-grade receivers, the carrier-to-noise density ratio is proven to perform better in smartphones due to lower correlation between measurement quality and elevation angles with embedded linearly polarized antenna. Two widely applied C/N$_0$-based weightings are (Brunner et al. 1999; Wieser and Brunner 2000; Wang et al. 2023):

$$\sigma_{C/N_0,1}^2 = b_{C/N_0,1}^2 \cdot 10^{\frac{\max(SNR_t - snr, 0)}{10}} \tag{5.3}$$

$$\sigma_{C/N_0,2}^2 = a_{C/N_0,2}^2 + b_{C/N_0,2}^2 \cdot 10^{\frac{-0.5 * snr}{10}} \tag{5.4}$$

where $\sigma_{C/N_0,1}^2$ and $\sigma_{C/N_0,2}^2$ are the C/N$_0$-based weighting variances. $a_{C/N_0,2}^2$, $b_{C/N_0,2}^2$, and $b_{C/N_0,1}^2$ are the unit weight mean square errors. snr is the SNR value from receiver independent exchange (RINEX) format observation file.

Normally, it is preferred to have a common weighting function for all the constellations and frequencies. However, the measurements on the third frequency appear to have better quality than the first frequency (Robustelli et al. 2019). Therefore, the weighting functions on different frequencies are adjusted by, e.g., adjusting the measurement noise parameters (adopted by RTKLib and GAMP (Zhou et al. 2018)), or by proposing different weighting schemes for different frequencies (Wang et al. 2023, Li et al. 2022). The range errors, indicative of the measurement noise level in realistic environments, can be derived using the method in Chapter 3. With these range errors, a constellation and frequency-specific weighting scheme can be fitted using Equation (5.3) or (5.4). However, the fitted function exhibits an over-optimistic problem for GPS L5 and Galileo E5a, which can be briefly described as an over-optimistic weight on L5 and E5a when the SNR values are low. This issue will be discussed in the results section. Whether using multipath or residuals as the metric to fit the functions, this issue must be addressed. A scale factor is applied, and the improved weighting scheme (abbreviated as consFreSpe in the following sections) is given as:

$$\sigma_{conFreSpe} = \alpha \cdot \sigma_{C/N_0,1} + (1-\alpha) \cdot \sigma_{fitted} \tag{5.5}$$

with

$$\alpha = \begin{cases} 0 & , \quad snr \geq SNR_{95} \\ \dfrac{SNR_{95} - snr}{SNR_{95} - SNR_{mean}} & , SNR_{mean} < snr < SNR_{95} \\ 1 & , \quad snr \leq SNR_{mean} \end{cases} \tag{5.6}$$

where $\sigma_{conFreSpe}$ is the improved measurement standard deviation weight, σ_{fitted} is the function fitted using range errors using equation (5.3) or (5.4). α is the scale factor, with SNR_{95} and SNR_{mean} the 95th percentile and average values of frequency-specific SNR values in current epoch. The above weighting function indicates that for SNR values larger than SNR_{95}, the weighting scheme fully depends on the fitted function, and for SNR values less than SNR_{mean}, the conventional weighting scheme is used. This method can avoid the over-optimistic issue, and at the same time, maintain the relationship between SNR and range errors with fitted functions.

5.2.2 A posteriori residual rejection

Solution validation is crucial in data processing, as it specifies whether the solution is with high confidence level. A posteriori residual is used to diagnose the outliers because the residual of an outlier is more likely to have a large value. Once the residual is rejected, the EKF filter is re-run until no residuals exceed the threshold. It is noted that sometimes the residuals are highly correlated, and the current research assumes that the largest residual indicates the most possible outlier. A two-step a posteriori residual rejection method is proposed here, wherein the measurement with lowest SNR value is rejected first, followed by the largest posteriori residual. The detailed algorithm is:

(1) Calculating the standard deviation of the a posteriori residuals (σ_{post}), if exceeds a given threshold κ_{fixed} , then rejecting the measurements with lowest SNR value once the SNR is smaller than the SNR cutoff. The κ_{fixed} is set to 10 m (three times standard derivation of pseudorange post-fit residuals for smartphones suggested in Seepersad et al. (2021)), and the SNR cutoff is set to 30 dBHz in this study. The first step is motivated by the high likelihood of low-SNR measurements being outliers. If it is below the threshold, even with a small weigh, it can still impact the solution.

(2) With derived range errors, the standard deviations of range errors for different SNR values can be calculated, and a second-order polynomial function is utilized to fit the standard deviations, as:

$$\kappa_{fit} = a_{fit} \cdot snr^2 + b_{fit} \cdot snr + c_{fit} \tag{5.7}$$

with a_{fit} , b_{fit} , and c_{fit} the fitting coefficients. The residual rejection threshold tightens as the SNR values increases, because a high-SNR measurement is assigned a high weight, and the presence of an outlier in such a measurement can significantly degrade positioning performance. Therefore, Equation (5.7) is devised to set a tight threshold for high-SNR measurements. Finally, to prevent rejecting too many measurements and ensure solution availability, the number of rejected measurements is considered, as:

$$RJ_{threshold} = \begin{cases} \frac{n_{rejected}}{n_{total}/4}(\kappa_{fixed} - 2\kappa_{fit}) + 2\kappa_{fit} & , n_{rejected} < \frac{n_{total}}{4} \\ \kappa_{fixed} & , n_{rejected} \geq \frac{n_{total}}{4} \end{cases} \tag{5.8}$$

where $n_{rejected}$ and n_{total} are the number of rejected and total measurements in the current epoch, respectively. $RJ_{threshold}$ is the calculated threshold for residual rejection.

5.3 Dataset and processing strategy

Thirteen smartphone datasets with Samsung S21 and Xiaomi Mi8 model phones were collected in suburban environments near York University, Toronto, Canada, on different days. These smartphones can track GPS L1/L5, Galileo E1/E5a, BDS B1, and GLONASS L1 signals. It is worth noting that the number of phase measurements on GPS L5 and Galileo E5a is less than those on L1. Moreover, sometimes the phase measurements are not recorded while there are available pseudorange measurements (Yi et al. 2024). The smartphones were mounted on the car dashboard, and GNSS measurements were recorded using the Geo++ RINEX logger (Wübbena et al. 2018). For a reliable reference solution, a base station was set on the roof of the GNSS lab at York University, and a NovAtel SPAN (OEM7+INS) was mounted on the car roof during data collection, with the lever arm between the smartphone and SPAN antenna pre-measured. The commercial Inertial Explore (IE) software was used to generate the post-processed kinematic (PPK) / (inertial measurement unit) IMU tightly-coupled reference solution with lever arm compensated for further analysis of smartphone positioning performance. The reference trajectory errors (of a few centimetres) can be neglected compared to smartphone positioning accuracy. Data collection trajectory is similar to Figure 4.2, and Table 5.1 summarizes the dataset ID, smartphone brands, and collected dates. The duration of each smartphone dataset is 20-30 minutes. 54% of the data are used as training datasets, and the rest are test datasets. The training datasets are used to calculate the range errors and model fitting, while the test datasets are used as user datasets to conduct PPP processing. The purpose of the divided training and test datasets is to avoid the same datasets used in both model construction and algorithm validation.

Table 5.1 Overview of realistic smartphone datasets used for training and testing

Training datasets				Test datasets			
ID	Brand	Collected date	Duration (min)	ID	Brand	Collected date	Duration (min)
1	S21	2021-08-08	26	8	S21	2021-08-20	25
2	Mi8	2021-07-30	26	9	Mi8	2021-08-08	26
3	S21	2022-10-09	21	10	S21	2022-10-09	22
4	Mi8	2022-10-09	22	11	Mi8	2022-11-08	24
5	S21	2022-11-08	24	12	S21	2022-11-08	23
6	Mi8	2021-07-30	26	13	Mi8	2021-11-30	33
7	S21	2021-11-30	33				

For the code/phase ratio analysis, all the datasets are utilized. To assess the proposed weighting scheme and residual rejection method, all datasets are divided into training and tests sets. The training datasets (4 of S21 and 3 of Mi8) are employed to derive the smartphone range errors and build the weighting and residual rejection functions, while the test datasets (3 of S21 and 3 of Mi8) are used to conduct PPP processing and generate horizontal positioning errors.

To assess the proposed stochastic model and residual rejection method, four different processing schemes were carried out, as outlined in Table 5.2. It can be noted from Table 5.2 that the proposed algorithms were validated step-by-step, and a conventional SNR-based weighting scheme was also applied as a comparison. Using schemes I and II, the performance of proposed adaptive phase/code ratio was assessed. Using schemes II, III, and IV, the new weighting scheme was validated and compared with SNR-based weighting and elevation-based weighting. Schemes IV and V were used to evaluate the residual rejection method.

In all schemes, the coordinates and receiver clocks are estimated as white noise, and ambiguity parameters are estimated as constants unless a cycle slip is detected. The ionospheric parameters are constrained using Klobuchar model (Klobuchar, 1987), and the ionospheric model residuals are estimated to avoid rank deficiency caused by simultaneously estimating ionosphere delays and ambiguities. The a priori code precision is set to 3.5 m, and the default residual rejection threshold is 10 m. In cases where the code measurement is available, but the corresponding phase is not recorded, the code measurement is still used, i.e., incorporating all available GNSS measurements, as suggested in Yi et al. (2024).

Table 5.2 Summary of data processing schemes used to validate the proposed quality control methods step-by-step

Scheme ID	P/L ratio	Weighting	Residual rejection threshold
I	1:100, 1:600	SNR-based (Eq. (5.3))	10
II	Adaptive (Eq. (5.1))	SNR-based (Eq. (5.3))	10
III	Adaptive (Eq. (5.1))	Elevation-based (Eq. (5.2))	10
IV	Adaptive (Eq. (5.1))	consFreSpe (Eq. (5.6))	10
V	Adaptive (Eq. (5.1))	consFreSpe (Eq. (5.6))	Two-step (Eq. (5.7)-(5.8))

5.4 Results, analysis, and discussion

This section introduces the fitted weighting scheme and residual rejection threshold using the training datasets and provides the fitting coefficients. Smartphone users are more interested in horizontal positioning errors than vertical components in applications such as vehicle and pedestrian navigation. Therefore, the horizontal positioning results are analyzed in detail, with statistics including 68th and 95th percentiles, as well as the corresponding root mean square (abbreviated as Per.68, Per.95, rms.68, and rms.98, respectively, in the tables and figures in the following sections). Additionally, the percentages of horizontal positioning errors below 1.5 m and 1 m are summarized for different schemes to validate the potential in lane-level navigation and sub-metre positioning performance, respectively.

5.4.1 Discussion on the fitted weighting scheme

With the derived range errors for each constellation and frequency, median values and standard deviations with respect to each SNR value can be calculated. The corresponding error bars are illustrated in Figure 5.2, where the blue stars represent the median values of range errors, and the error bar line heights are two times standard deviation, inferring that the peak of each error bar is the sum of the median and two times the standard deviations range error. A weighting scheme based on the range errors is fitted using the sum of the median and two times standard deviations. This approach ensures that ~95% of the range errors are properly fitted. The fitting coefficients are provided in Table 5.3.

Table 5.3 Fitting coefficients for frequency and constellation-specific weighting scheme

Band	a_{C/N_0}	b_{C/N_0}	Band	a_{C/N_0}	b_{C/N_0}
GPS L1	2.86	243.37	GAL L1	3.77	160.89
GPS L5	2.11	56.82	GAL L5	1.74	59.77
GLO L1	10.17	288.12	BDS L1	4.64	194.30

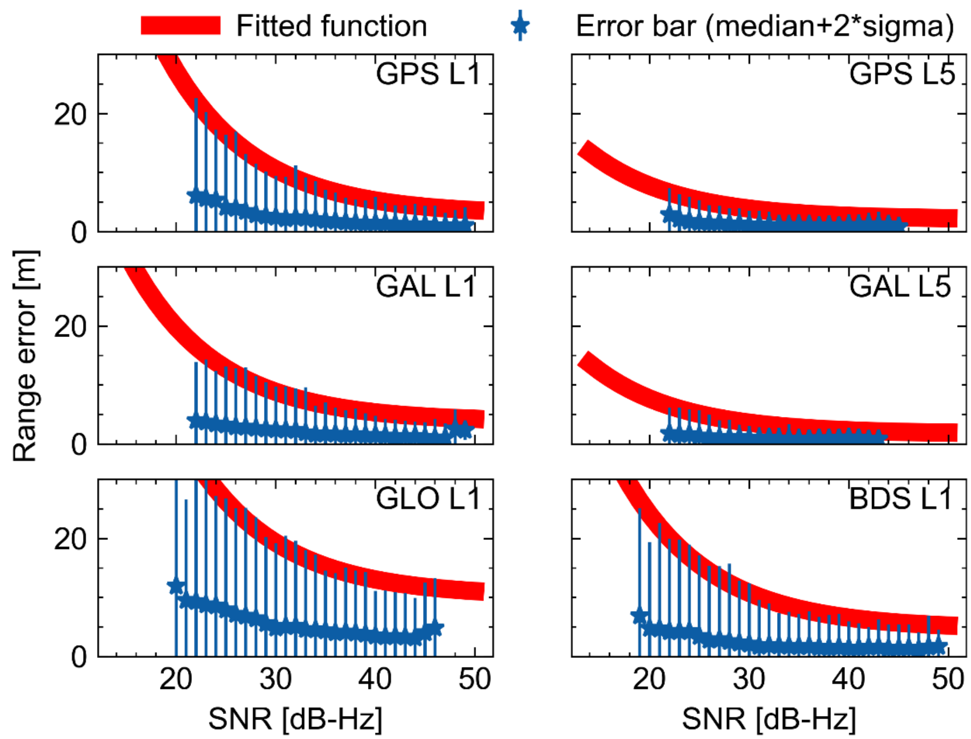

Figure 5.2 Error bars for range errors and fitted functions for each frequency and constellation. The blue stars are the median values, the error bar line heights are two times standard deviation. The red lines are the fitted functions

When using the fitted function from Figure 5.2 as the weighting scheme, assuming similar SNR values for the measurements, GPS L5 and Galileo E5a is approximately 2 times more precise than the first frequency, while GLONASS and BDS measurements are slightly de-weighted. This trend aligns with existing research, as observed Xu et al. (2023). However, the fitted function also raises a problem that the measurements on GPS L5 and Galileo E5a are over-optimistic for low SNR values. For instance, the weight for GPS L5 with an SNR of 18 dBHz is almost equal to that of GPS L1 with 30 dBHz, or even GLO L1 with an SNR value exceeding 40 dBHz. This discrepancy is unexpected and could significantly bias the solution once there is a large noise on L5. Therefore, a scale factor is introduced as given in Equation (5.5). Taken specific values of $SNR_{mean} = 30$ and $SNR_{95} = 40$ as examples, Figure 5.3 illustrates the scaled fitted weighting scheme and the SNR distributions for all experimental datasets. The conventional C/N_0-based weighting scheme is also provided for comparison, as the blue dashed lines. From Figure 5.3, it can be concluded that for lower SNRs, the conventional weighting scheme is applied, and for SNRs larger than 30 dBHz (covering more than 80% of the experimental datasets), the fitted function, which better represents realistic range errors, is utilized.

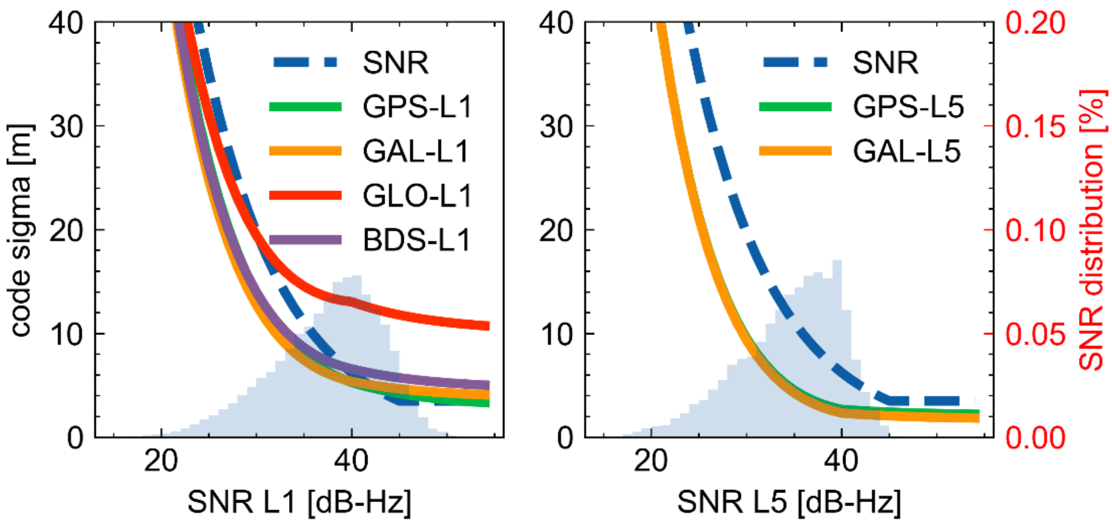

Figure 5.3 Illustration of constellation and frequency-specific weighting and SNR distribution of test datasets. The blue dashed lines are the conventional C/N_0-based weighting schemes.

5.4.2 Discussion on the fitted residual rejection threshold

The correlation between range errors and SNR values infer that the range error and corresponding standard deviation decrease with the increase in SNR. Measurements with large range errors are more likely to have large posteriori residuals. Therefore, the standard deviations at each SNR can serve as an indicator for diagnosing outliers. Table 5.4 gives the fitting coefficients and Figure 5.4 depicts the standard deviations and the fitted function using a second-order polynomial. Notably, for GPS L5 and Galileo E5a, the standard deviations are smaller compared to the first frequencies, while all constellations have similar values on L1.

Table 5.4 Constellation and frequency-specific polynomial fitting coefficients for the residual rejection threshold function

Band	a_{fit}	b_{fit}	c_{fit}	Band	a_{fit}	b_{fit}	c_{fit}
GPS L1	0.011	-1.028	24.760	GAL L1	0.003	-0.387	12.658
GPS L5	0.005	-0.383	8.277	GAL L5	0.006	-0.448	9.486
GLO L1	0.004	-0.578	21.582	BDS L1	0.009	-0.891	22.944

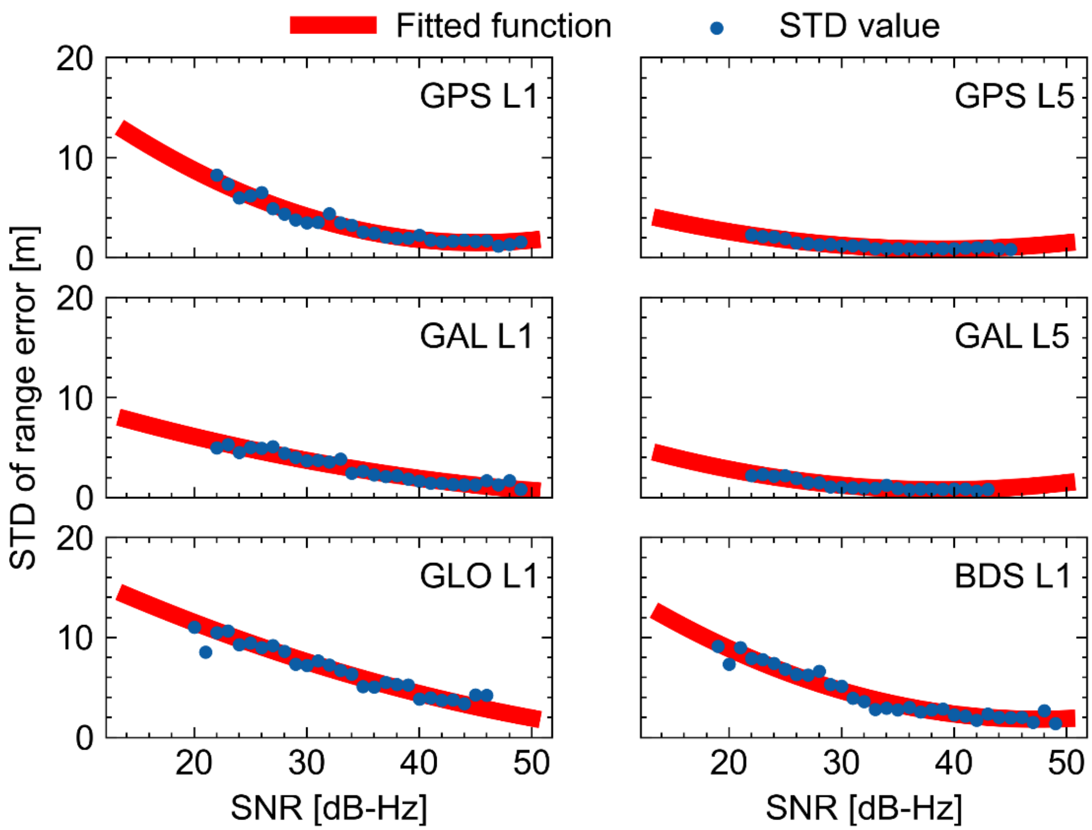

Figure 5.4 Constellation and frequency-specific standard deviation of absolute range errors for each SNR value and the fitted function. The blue dots are the standard deviation, and the red lines are the fitted functions

Treating a posteriori residuals larger than two times of the fitted value (confidence level of 95%) as outliers, constellation and frequency-specific residual rejection threshold functions are proposed, as shown in Figure 5.5. A fixed threshold is provided for comparison, and whenever the calculated threshold exceeds the default fixed threshold ($\kappa_{fixed} = 10$ in this study), the default value is used. It is noteworthy that the thresholds on L5 are tighter than those on L1, and for GLONASS, the thresholds are larger than for other constellations. This strategy aims to balance the higher weights on L5. For example, L5 measurements are assigned more weights in the weighting scheme, and once there is an outlier among the L5 measurements, the negative impact on the positioning results will be more significant compared to the less-weighted L1 measurements.

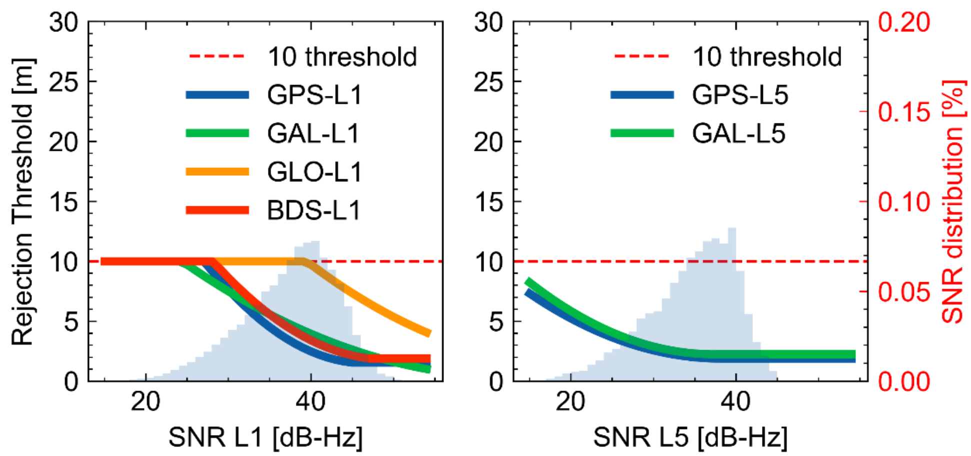

Figure 5.5 Illustration of constellation and frequency specific residual rejection threshold and SNR distribution for test datasets. The red dashed lines are the empirically threshold of 10 m

5.4.3 Analysis of the adaptive phase/code precision ratio

To validate the performance of the proposed adaptive phase/code precision ratio, all datasets are processed. Figure 5.6 illustrates the horizontal positioning errors for dataset 8 in Table 1 as an example.

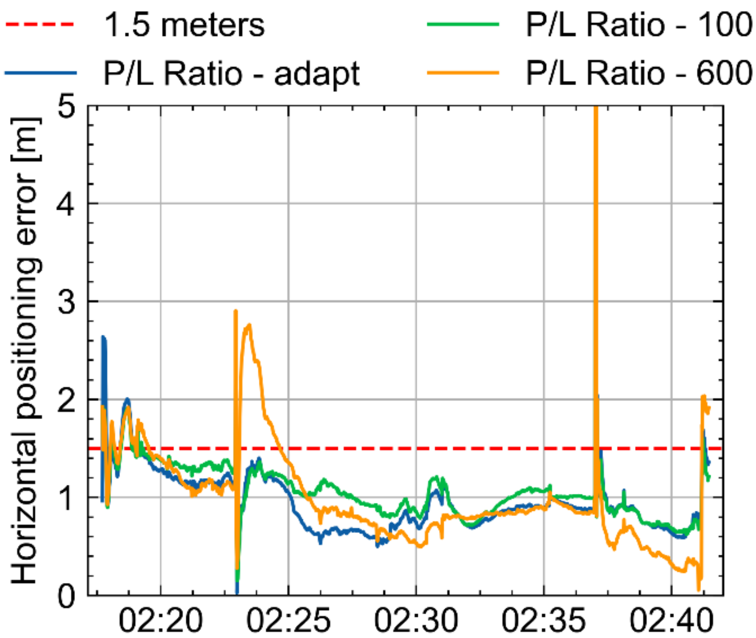

Figure 5.6 Time series of horizontal positioning performance for fixed phase/code ratios of 100, 600, and adaptive phase/code precision ratio for dataset 12. Different colours denote different ratios

The spikes during ~02:23 and ~02:37 are caused by signal loss when vehicle traversed under large overpasses, and therefore, all three schemes have similar spikes. For this dataset, the proposed method outperforms the fixed ratio of 600 during the initialization period of the ambiguity parameters (e.g., during 02:23~02:29), and the horizontal positioning errors are smaller than the fixed ratio of 100 after the convergence (02:25~02:37). This result aligns with expectations, as the proposed method aims to provide a solution that combines the good performance during the initialization for a low ratio, and after the convergence for a high ratio.

Figure 5.7 and Table 5.5 summarize the statistics for all the processed datasets, indicating that the proposed adaptive ratio exhibits the best performance among the three ratios. Compared to the commonly used ratio of 100, it reduces the 68^{th} and 95^{th} horizontal positioning errors by 4 cm and 3 cm, respectively. Furthermore, the percentage of horizontal positioning errors within 1 m can be improved by 8%, with a total of 18,853 epochs. This improvement indicates that the adaptive phase/code ratio has the potential to enhance results to the sub-metre level. Normally in lane-level navigation, considering that the width of a lane is approximately 3 metres, horizontal positioning errors within 1.5 m can be regarded as the capability of providing lane-level navigation. The positioning results with adaptive ratio indicate that the proposed method outperforms a fixed ratio, and is able to provide lane-level navigation solution for longer periods of time.

Table 5.5 Statistics of 68th and 95th horizontal positioning errors, as well as corresponding RMS for different phase/code ratio schemes (units: m)

	Per.68	Per.95	RMS.68	RMS.95	Percent within 1.5 / 1 m
P/L 100	1.18	1.79	0.88	1.05	85% / 50%
P/L 600	1.21	1.84	0.86	1.06	82% / 51%
adaptive	1.14	1.76	0.82	1.00	86% / 58%

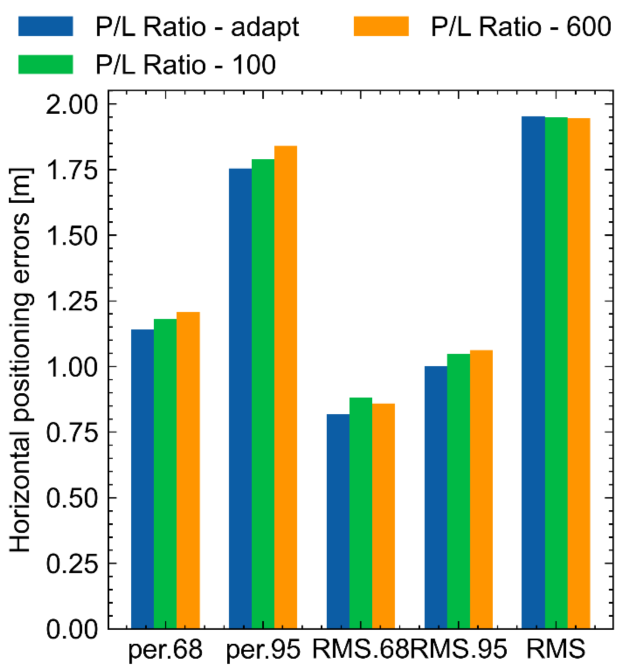

Figure 5.7 Illustration of statistics for horizontal positioning errors when using different phase/code ratio schemes for all datasets. Different colours denote different ratios

5.4.4 Analysis of weighting schemes and a posteriori residual rejection

The assessment of the proposed weighting scheme and a posteriori residual rejection method is conducted with experimental datasets. Figure 5.8 presents the time series of horizontal positioning errors with conventional C/N_0-based weighting (Scheme II, labelled as SNRWeight), proposed weighting (Scheme IV, labelled as consFreSpe), and proposed weighting with proposed residual rejection method (Scheme V, labelled as consFreSpe_Rj). Two large spikes in the time series are primarily caused by signal loss during passages of overpasses. It is evident that the proposed weighting scheme performs better for almost all epochs, and the proposed residual rejection method further improves the performance, especially after the second large spike for datasets 9, 11, and 12. The positioning solution with constellation- and frequency-specific weighting functions has a better stability than conventional C/N_0-based weighting, as seen in dataset 12 during 02:05-02:10. The proposed residual rejection method further improves the positioning performance especially when the observation is at high noise level, which can be obviously noticed after the second spike for each dataset.

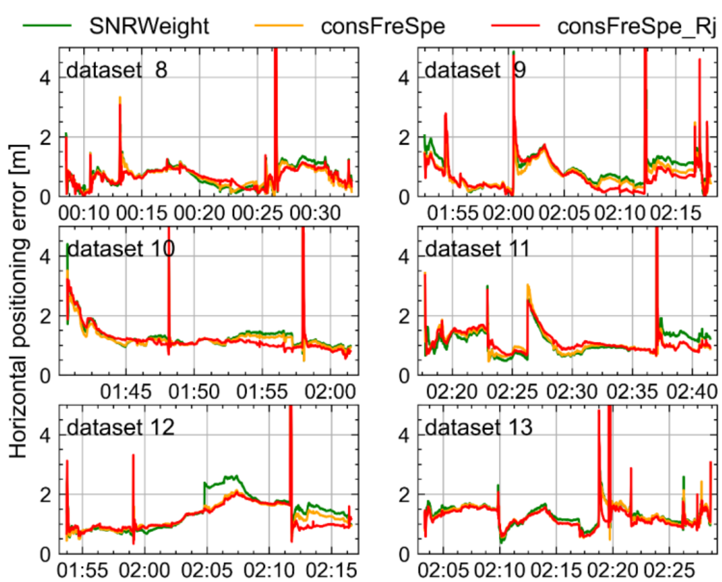

Figure 5.8 Horizontal positioning errors for experiment datasets with conventional C/N_0-based weighting, constellation and frequency-specific weighting, and residual rejection. Green lines are solution for conventional method, while yellow and red lines are for constellation and frequency-specific weighting and residual rejection solutions, respectively

Table 5.6 summarizes the statistics of all schemes, and Figure 5.9 illustrates the cumulative distribution function (CDF) of horizontal positioning errors for experimental datasets. Elevation-dependent weighting is included for comparison. Compared to conventional C/N_0-based weighting, the proposed weighting scheme improves the 68^{th} and 95^{th} percentile horizontal positioning errors by 14 cm and 15 cm, representing improvements of 11% and 8%, respectively. With 8590 epochs (2.4 hours) in total for experimental datasets, the most significant improvement when applying the proposed residual rejection method is the percentage of positioning errors within 1 m, which improves from 42% to 54%. These improvements demonstrate that the proposed stochastic model and residual rejection method outperform the conventional methods and have potential in achieving a stable sub-metre-level positioning accuracy with smartphones in suburban environments. The merging point in Figure 5.9 indicates that, despite the proposed quality control methods always perform better than conventional method in CDF, the fitted weighting function does not fully represent the actual noise levels of measurements in realistic environments, as sometimes, the results from elevation-dependent weighting scheme can be comparable to the proposed method. This finding further motivates potential future research on developing an environment-related weighting scheme.

Table 5.6 Statistics of horizontal positioning errors when using different quality control schemes (units: m)

Schemes	Per.68	Per.95	RMS.68	RMS.95	Percent within 1.5 / 1 m
Elevation	1.34	1.93	0.98	1.19	76% / 38%
SNR	1.30	1.81	0.92	1.11	83% / 42%
consFreSpe	1.16	1.66	0.88	1.04	86% / 49%
consFreSpe_Rj	1.13	1.68	0.84	1.02	87% / 54%

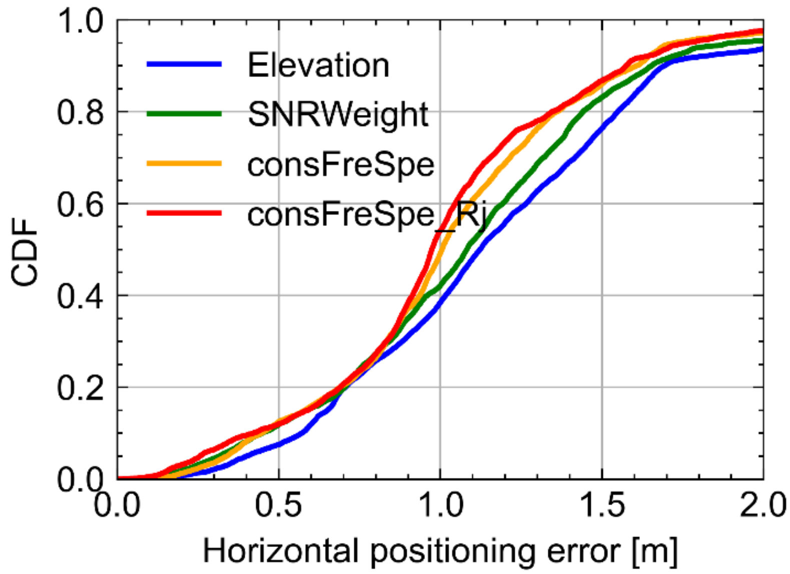

Figure 5.9 CDF of horizontal positioning errors for experiment datasets. Blue line is elevation-dependent weighting, green is conventional C/N_0-based weighting, and yellow and red are constellation and frequency-specific weighting and residual rejection solutions, respectively

5.5 Summary

With the proposed adaptive a priori phase/code ratio, the positioning performance surpasses that of the conventional used fixed ratio of 100. Compared to a ratio of 100, it performs better after the convergence of ambiguities because of a higher precision of equivalent range recovered by phase measurements. At the same time, it integrates good performance during the convergence with a low ratio. Overall, the percentage of horizontal positioning errors within 1 m are improved by 8% compared to a ratio of 100.

A step-by-step improvement can be observed when applying the proposed weighting scheme and residual rejection method to experiment datasets and comparing the results with conventional processing strategies. The new weighting scheme can mitigate the positioning errors by decimetre-level, and with the new residual rejection method, the percentage of positioning errors within 1 m can be improved from 42% to 54% compared to conventional C/N_0-based weighting with a fixed residual rejection threshold of 10 m.

In conclusion, the proposed quality control methods are demonstrated to perform better than conventional processing strategies in suburban environments and have a great potential of reaching a sub-metre level positioning accuracy with smartphones. These improvements contribute to smartphone applications such as pedestrian navigation and lane-level navigation. Noting that the horizontal positioning errors were assessed in this research, the cross-track and along-track errors would be smaller than horizontal errors components for, e.g., lane-level navigation.

However, there is still work to be done. Limited to the data collection area in this study, the performance of the proposed method is worth investigating with smartphone datasets from other regions and from more complex environments. These methods may also work for geodetic-grade receivers, which would potentially benefit convergence and ambiguity resolution. Furthermore, with improved smartphone positioning performance, float ambiguity estimates can be more precise and may benefit smartphone AR in realistic environments.

6 AMBIGUITY RESOLUTION: SUB-METRE POSITIONING ACCURACY WITH SMARTPHONES

Smartphone carrier phase ambiguity resolution has been a challenging topic due to the noisy GNSS measurements collected with embedded antennas and low-cost chipsets, as analyzed in Chapter 3. Fixing ambiguities to integers is necessary in achieving high-precision positioning performance in geodetic receivers (Hu et al. 2020). Therefore, this chapter focuses on investigation the feasibility of conducting ambiguity resolution with smartphone data, aiming to provide sub-metre or decimetre-level positioning accuracy in realistic environments with embedded smartphone antennas. With RTK, PPP, and PPP-RTK, the smartphone raw ambiguities are estimated, and the raw ambiguity availability and stability is analyzed first. Considering the variation in smartphone raw ambiguities, wide-lane partial ambiguity resolution with RTK is proposed. The mathematical model to derive WL ambiguities is introduced, which contains MW combination and subtraction of the estimated raw ambiguities ($N_1 - N_5$). Three AR methodologies, including rounding, LAMBDA, and BIE, are briefly introduced. The proposed partial WL AR ambiguity candidates selection strategy is presented, followed by a discussion of a novel automatic ambiguity hold strategy. A simulated experiment on the effect of fixed WL ambiguities on position precision is carried out. With both static and kinematic actual data, the observation quality, number of available WL ambiguities, as well as the corresponding positioning performance are evaluated. Part of this work has been published in Hu et al. (2023d).

6.1 Introduction and motivation

As discussed in chapter 3, the biggest limitation for smartphone GNSS applications is noisy measurements. The pseudorange measurements typically yield accuracies of approximately 6 metres and 2 metres for GPS L1 and L5 signals, respectively, when using a Xiaomi Mi8 phone in open sky area

(Robustelli et al. 2019). Consequently, smartphones achieve only ten-metre-level SPP performance (Paziewski et al. 2020; Sikirica et al. 2017). In contrast, GNSS carrier phase measurements exhibit higher precision, with an estimated accuracy of approximately 0.04 cycles for a tablet personal computer (PC) placed in a radio frequency (RF) shielding box (Li et al, 2019). Although smartphone phase measurements may be noisier in realistic environments with embedded antenna, they still offer significantly higher accuracy than pseudorange measurements. Therefore, properly resolving the integer wavelength count (aka ambiguity) in phase measurements can effectively treat phase measurement as a high-precision range measurement, leading to a significant improvement in positioning performance (Ge et al. 2008; Laurichesse et al. 2009; Collins et al. 2008).

Early research focused on using external antennas or collecting smartphone data under optimal environments for ambiguity resolution. With an external antenna and zero-baseline setup, the unaligned chipset initial phase biases (IPBs) were calculated and investigated. It was found that IPBs differ randomly among satellites and change unpredictably when phase signals were re-acquired (Geng et al. 2019). The integer characteristics for ambiguities were also assessed by performing zero-baseline experiments, and it was reported that the GPS L1 ambiguities have weak integer characteristics (Gao et al. 2021; Wanninger and Heßelbarth 2020), potentially posing challenges in fixing raw ambiguities. Moreover, the integer properties of DD ambiguities were found to depend on smartphone brands, embedded antennas, operating systems, and smartphone orientation (Li et al. 2022c). In principle, the fractions of raw ambiguities with embedded antennas are significantly larger than those with an external antenna (Miao et al. 2022), presenting a challenge in fixing raw ambiguities with embedded antennas. Most experiments conducted thus far have been carried out in optimal static environments. However, for realistic user applications characterized by severe signal blockage and significant multipath effects, the behavior of ambiguities, as well as their variance and covariance information, may differ, exhibiting less of an integer property. Compared to raw ambiguities, WL ambiguities possess longer wavelengths, approximately 75 cm for GPS L1/L5 and Galileo E1/E5a. This result suggests that fixing WL ambiguities rather than individual frequency ambiguities for smartphones may be more useful.

Different methods can be employed to resolve float ambiguities to integers. Rounding to the nearest integer is the simplest approach but disregards the correlation among the ambiguities. Therefore, the LAMBDA method is usually applied in smartphone AR (Teunissen 1995; Tao et al. 2023), which involves decorrelation, search, and transformation procedures. An improved AR algorithm which uses the search-and-shrink procedure coupled with multi-epoch DD residual test and ambiguity majority tests was proposed to process smartphone data (Jiang et al. 2023). Moreover, the BIE method was applied in processing smartphone data collected in open sky environments with an external low-cost antenna, and the results showed that the BIE solution resembles the float solution when the success rate (SR) is low and is close to the fixed solution when the SR is high (Teunissen 2003; Yong et al. 2022). However, in realistic environments, fixing all ambiguities can be challenging, necessitating the application of partial ambiguity resolution (Li and Zhang 2015). With criteria for selecting ambiguity subsets for fixing, under conditions of a limited number of WL ambiguities and noisy measurements, there might be only one or two candidates. However, whether limited fixed ambiguities will benefit the solution has not been thoroughly investigated in the existing literature.

Considering the above-mentioned progress and concerns in smartphone GNSS AR, the main contributions and novelty of this study are as follows.

(1) Different from most current smartphone AR research in which smartphones are attached to external antennas or under open-sky environments, in this dissertation, smartphone datasets collected in realistic driving environments are used to perform AR, with smartphones mounted on the vehicle dashboard and embedded antenna, to investigate the feasibility of fixing smartphone ambiguities in real-life environments.

(2) While existing research tends to focus on fixing smartphone raw ambiguities, this contribution proposes to fix smartphone WL ambiguities for the first time, and the proposed algorithm is validated with both static and kinematic positioning results.

(3) PAR is adopted in WL AR, and the impact of the number of fixed WL ambiguities on position precision is analyzed, which is further developed to a strategy of fixing every possible WL ambiguity in smartphones. Compared to the conventional AR procedure in which, e.g., at least 4 ambiguities are fixed, the proposed strategy makes full use of every WL ambiguity.

(4) An automatic ambiguity hold strategy is proposed for fully utilizing the correctly fixed ambiguities. The best integer equivariant method is applied in kinematic data to improve the reliability of WL AR solutions.

6.2 Datasets and experimental setup

To validate the proposed smartphone WL PAR algorithm, both static and kinematic datasets were collected and processed. For all datasets, GPS L1/L5, Galileo E1/E5a, BDS B1, and GLONASS L1 signals are processed. The static data were collected with a Xiaomi Mi8 phone on April 14, 2022, atop one of the buildings at Wuhan University, Wuhan, China, for a duration exceeding 3 hours. The experimental setup is illustrated in Figure 6.1, where the smartphone was mounted on a tripod. The base station was a Trimble Alloy receiver equipped with a geodetic-grade antenna (Harxon HX-CGX606A), situated at a baseline distance of ~20 m. From Figure 6.1, the smartphone measurements may suffer from heavier multipath compared to a pure open sky environment due to the wall near the tripod and the surrounding tall buildings. To generate the reference solution, a Trimble Alloy receiver was placed on the tripod both before and after the smartphone data collection, and the solutions were calculated using the IE software. The average coordinates from these two solutions were adopted as the user geodetic receiver position. Therefore, with lever-arm carefully measured and compensated for, the reference coordinates of the smartphone can be obtained.

Figure 6.1 Static smartphone data collection environment with a Xiaomi Mi8 phone on April 14, 2022, atop one of the buildings at Wuhan University, Wuhan, China, for a duration exceeding 3 hours.

Three kinematic datasets (a subset from Table 5.1 in Chapter 5) are used to assess the ambiguities and validate the proposed smartphone ambiguity resolution method. The overview of the kinematic data is summarized in Table 6.1.

Table 6.1 Overview of 3 smartphone kinematic datasets used in the validation of ambiguity resolution

Dataset ID	Smartphone	Collection date	Duration (minutes)
1	S21	2021-08-08	26
2	Mi8	2021-07-30	26
3	S21	2022-10-09	21

6.3 Raw ambiguity assessment

The conventional AR is conducted with raw ambiguities. Therefore, the availability of raw ambiguities is assessed first. With RTK, PPP, and PPP-RTK, the estimated ambiguities are analyzed, and the stability is evaluated. To reduce repetition in analysis, results for dataset #1 are provided.

6.3.1 Ambiguity availability

The raw phase measurement availability is first analyzed and presented in Figure 6.2, from which it can be concluded that with the observed 27 satellites, only single-frequency GLONASS and BDS satellite measurements can be tracked for S21 smartphone GNSS chip, while dual-frequency observations for all Galileo satellites are available. For some GPS satellites such as G12, G21, G22, and G31, only single-frequency data are recorded. The assessment of phase measurement availability indicates that for BDS and some GPS satellites, the conventional AR procedure, which first fixes WL ambiguity and then narrow-lane (NL) ambiguity, is not applicable at all. At the same time, even the ambiguities can be fixed at one time, it would be challenging to use "fix and hold" mode due to the dual-frequency discontinuity caused ambiguity re-initialization.

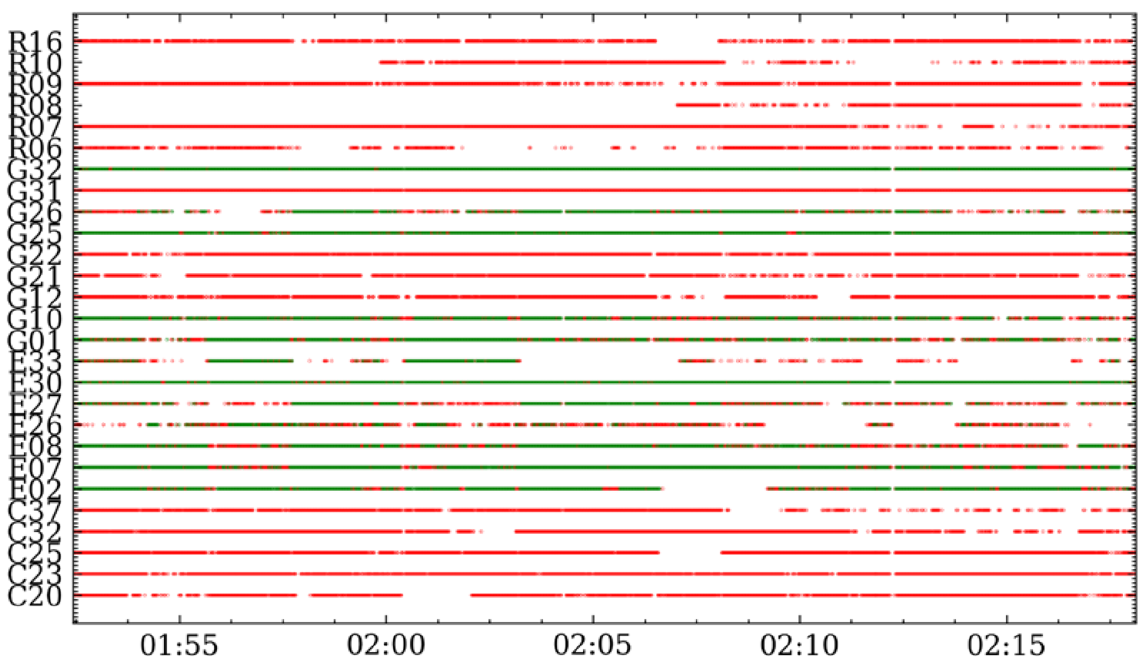

Figure 6.2 Time series of phase measurement availability for observed satellites. Red dots represent single-frequency data, and green dots denote dual-frequency data.

Figure 6.3 provides a different aspect of phase measurement availability from the percentage of missing phase measurements and dual-frequency observations. During the data collection period, measurements from most satellites suffer phase loss. The worst case is for satellite E33, with a signal loss of 60%.

Satellites E02, E30, G25, G31, and G32 have the highest phase measurement availability, representing a signal loss of less than 5%. For satellites such as E26, E27, and E33, almost half of the recorded measurements are single frequency, resulting in the decreased number of available WL ambiguities, and further impacting the possibility of realizing WL AR.

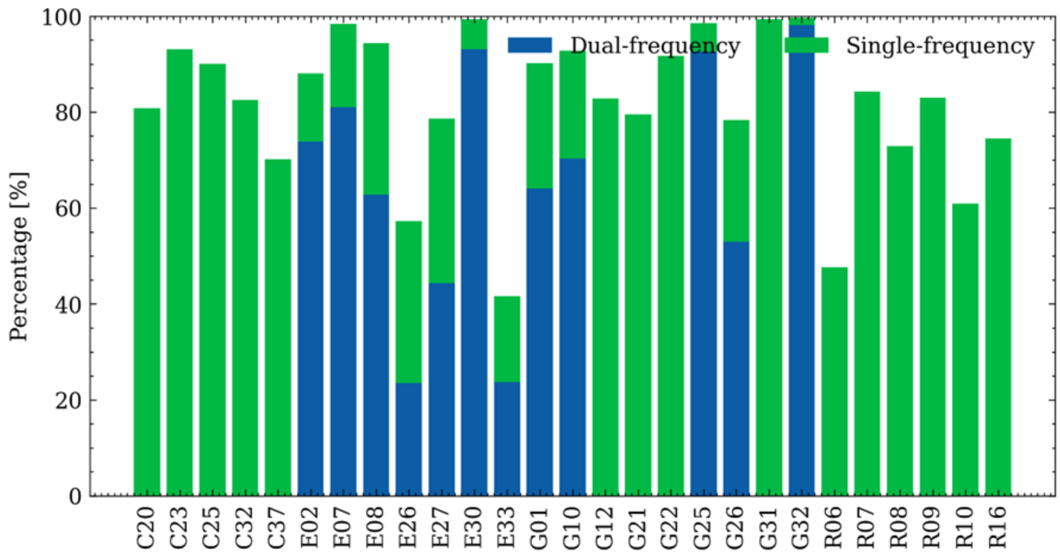

Figure 6.3 Percentage of available single- and dual-frequency measurements for each satellite. Green is the percentage for single-frequency observations, while blue is for dual-frequency measurements

6.3.2 Ambiguity stability

Ambiguity time series and the corresponding variance information for RTK, PPP, and PPP-RTK are analyzed in this section. The purpose of evaluating ambiguity estimates from different methods is to assess whether there is different ambiguity stability with these methods. If so, the method with a more stable ambiguity estimates can be used for further ambiguity resolution. Figure 6.4 depicts the L5 ambiguity estimates for satellite G25, in which the ambiguity variance information is the same for all modes because of the same cycle slip detection methods. The ambiguity variance can be obtained from the corresponding diagonal element in the estimated variance-covariance matrix.

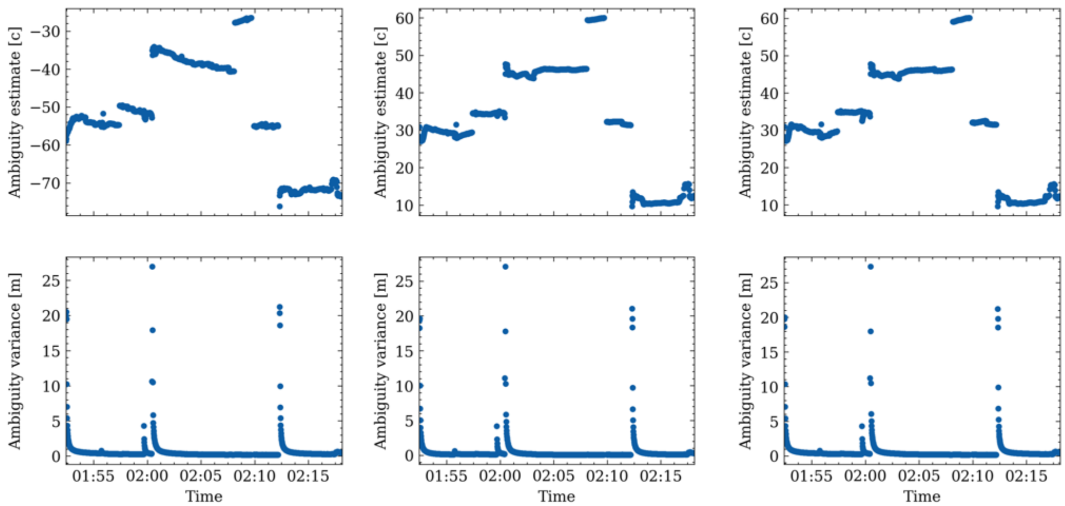

Figure 6.4 Raw ambiguity time series and the corresponding variance information of G25 L5 for RTK (left), PPP (middle), and PPP-RTK (right)

The ambiguity estimates for PPP and PPP-RTK have similar values and trends. However, for RTK ambiguity terms, the values are different because the estimated ambiguities are double-differenced. The DD ambiguity trends are also similar to PPP and PPP-RTK, but it makes the ambiguities correlated through the common reference satellite.

For a time period without cycle slips and signal blockage, a stable estimated ambiguity time series usually indicates a well-modelled mathematical model. Therefore, the stability of ambiguities is then assessed. Figure 6.5 displays the PPP-derived ambiguities and the corresponding variance information for C20, C32 and G25, respectively. There is a jump in ambiguity estimation while no similar trend is noted on variance information for C20 at some epochs (e.g., around 02:05, as highlighted in red box), which means that a cycle slip occurs but is not detected. This case indicates that the cycle slip detection with smartphone GNSS data needs to be further improved.

Two sets of statistics are calculated to characterize ambiguity stability: average value of ambiguity standard deviations for each continuously observed arc, and time-differenced ambiguity standard deviations (TD_STD). When calculating standard deviations for each continuous ambiguity arc, it should at least contain 10 epochs, and when assessing TD_STD, a threshold of 0.5 m is adopted to reject the time-differenced value larger than this threshold to avoid the influence of ambiguity jumps on the statistic. A constellation and frequency specific evaluation is carried out, as given in Figure 6.6. Results show that the smartphone GLONASS ambiguities have the poorest stability in both time series and time-differenced series, GPS L5 outperforms GPS L1, while Galileo L1 has a better stability compared to Galileo L5. Noting that the variation of raw ambiguities can reach to one cycle, it would be difficult to fix the NL ambiguities in a realistic environment.

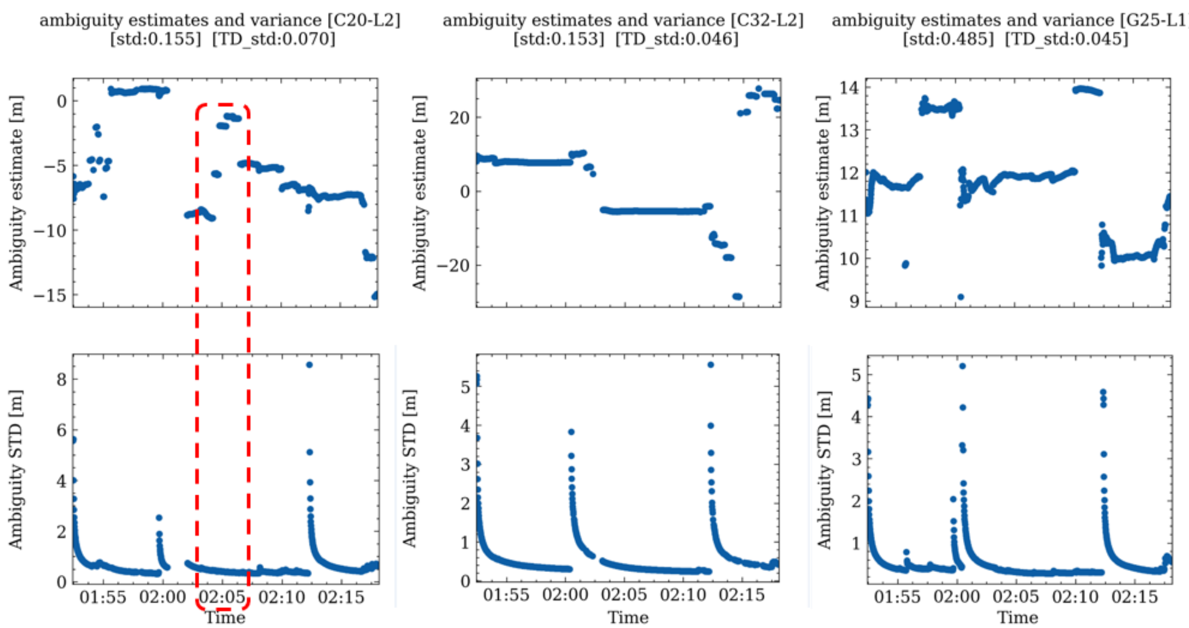

Figure 6.5 Time series of PPP-derived ambiguity and corresponding variance information. The red box indicating undetected cycle slips

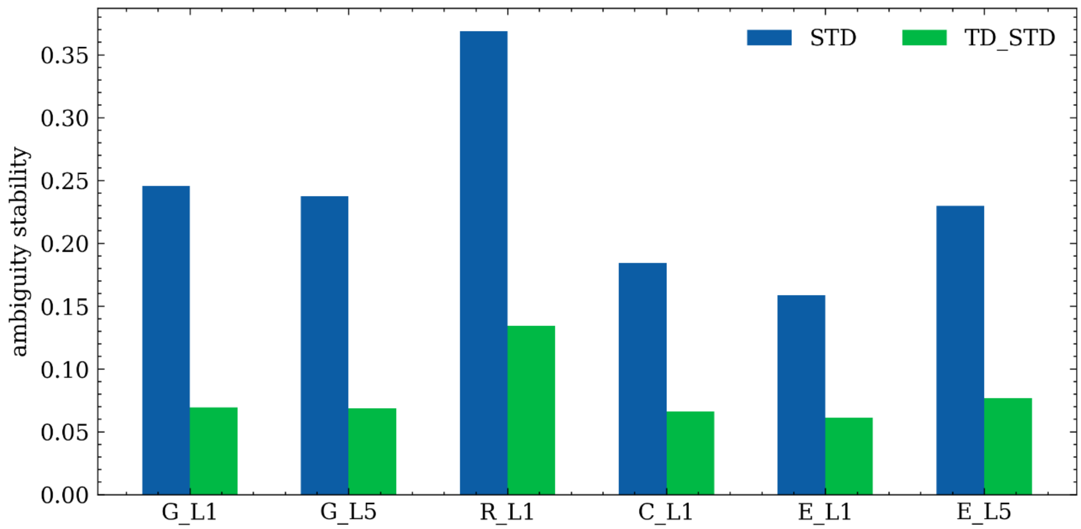

Figure 6.6 Constellation and frequency specific ambiguity estimates stability, the blue bars denote standard deviations of ambiguity time series, and the green bars are time-differenced standard deviations

6.4 Smartphone wide-lane ambiguity resolution methodology

The PPP, RTK, and PPP-RTK mathematical models were introduced in Chapter 2. In this section, methodologies for deriving WL ambiguities from MW combinations and raw ambiguities are described. Three WL AR methods are introduced: rounding, LAMBDA, and BIE. Considering the tracking ability of smartphones, the first frequency denotes GPS L1 and Galileo E1, and the third frequency represents GPS L5 and Galileo E5a unless otherwise specified.

6.4.1 Wide-lane ambiguity resolution

Given that it is not realistic to fix raw DD ambiguities for smartphones under typical user environments, it is proposed to fix DD WL ambiguities whose wavelengths are ~75 cm for GPS L1/L5 and GAL E1/E5a. The WL ambiguities can be derived from the Melbourne-Wübbena combination, or by subtracting the estimated raw ambiguities ($N_1 - N_5$).

The MW combination (Blewitt 1990) can be formed as:

$$MW_{15}^{s} = (f_1 L_1^s - f_5 L_5^s)/(f_1 - f_5) - (f_1 P_1^s + f_5 P_5^s)/(f_1 + f_5) \tag{6.1}$$

Hence, with a base station *b*, the between-receiver single-differenced (SD) MW ambiguity can be formed as:

$$\nabla WL_{MW}^{s} = MW_{15,r}^{s} - MW_{15,b}^{s} \tag{6.2}$$

where r and b denote rover (smartphone) and base station, respectively. With assumptions that: (i) the measurement noise level of the base station which is usually a geodetic-grade receiver is neglected compared to smartphone measurements; and (ii) the precision of smartphone phase measurements is significantly higher than that of pseudoranges. By applying error propagation law, the variance of Equation (6.2), which neglects base station observation noise and phase noise of smartphone, can be derived as:

$$\sigma_{\nabla WL_{MW}^{sk}}^{2} \approx \frac{f_1^2}{(f_1 + f_5)^2}\sigma_{P1}^2 + \frac{f_5^2}{(f_1 + f_5)^2}\sigma_{P5}^2 \tag{6.3}$$

where σ_{P1} and σ_{P5} are the noise for smartphone pseudorange measurements and can be determined using weighting scheme functions. For instance, in smartphone positioning, a C/N_0-based weighting scheme is demonstrably better than elevation-dependent weighting used for geodetic receiver measurements (Banville et al. 2019; Zangenehnejad and Gao 2021). One widely applied C/N_0-based weighting scheme is:

$$\sigma_{C/N_0}^{2} = a_{C/N_0}^{2} + b_{C/N_0}^{2} \cdot 10^{\frac{-0.5 \cdot snr}{10}} \tag{6.4}$$

where σ_{C/N_0}^{2} is calculated weighting variances. a_{C/N_0}^{2} , b_{C/N_0}^{2} are the unit weight mean square errors. snr is the SNR value from RINEX format observation file.

The single-epoch MW WL ambiguity is easily affected by noisy measurements. Fortunately, MW WL ambiguities can be filtered for continuously observed epochs. For satellite s with a total of n epochs without cycle slip detected, the filtered between-receiver SD MW WL ambiguity can be given as:

$$\nabla WL_{MW}^{s}\_filtered = \frac{\sum_{i=0}^{n}(\nabla WL_{MW}^{s}(i))}{n} \tag{6.5}$$

and the filtered MW WL ambiguity noise level can be derived via the error propagation law. By selecting a reference satellite, the DD MW-derived WL ambiguities can be calculated for fixing.

Aside from filtered DD MW-derived WL ambiguities, the WL ambiguities can be calculated using estimated raw DD ambiguities for each epoch. The DD $N_1 - N_5$ WL ambiguities and the corresponding variance are formulated as:

$$\nabla\Delta WL_{N1N5} = AN_{est} \tag{6.6}$$

$$\sigma^2_{\nabla\Delta WL_{N1N5}^{sk}} = AQ_{NN}A^T \tag{6.7}$$

with

$$A = \begin{bmatrix} 1 & -1 & 0 & 0 & \cdots & 0 & 0 \\ 0 & 0 & 1 & -1 & \cdots & 0 & 0 \\ & & & \ddots & & & \\ 0 & 0 & 0 & 0 & \cdots & 1 & -1 \end{bmatrix} \tag{6.8}$$

$$N_{est} = \begin{bmatrix} \nabla\Delta N_1^{1k} & \nabla\Delta N_5^{1k} & \nabla\Delta N_1^{2k} & \nabla\Delta N_5^{2k} & \cdots & \nabla\Delta N_1^{sk} & \nabla\Delta N_5^{sk} \end{bmatrix}^T \tag{6.9}$$

where Q_{NN} is the variance-covariance matrix of the filtered estimates, and the elements in Q_{NN} can be directly obtained from the filter outputs, $\nabla\Delta N_1^{sk}$ and $\nabla\Delta N_3^{sk}$ are the estimated DD ambiguities.

With either MW-derived or $N_1 - N_3$ WL ambiguities, the integer WL ambiguities can be obtained by rounding, LAMBDA, or BIE methods. For rounding procedure, the float MW WL ambiguities can be directly fixed to the nearest integers, and the validation of rounded integers can be presented by rounding success rate (Teunissen 1998):

$$P_0 = 1 - \sum_{i=1}^{\infty}[erfc(\frac{i - |\tilde{B} - b|}{\sqrt{2}\sigma}) - erfc(\frac{i + |\tilde{B} - b|}{\sqrt{2}\sigma})] \tag{6.10}$$

where $erfc(x) = \frac{2}{\sqrt{\pi}}\int_x^{\infty} e^{-t^2} dt$, $\tilde{B}$ is the rounded integer value, b is the float value, and σ is the corresponding variance. In LAMBDA, considering the correlation among the estimated ambiguities, decorrelation is first conducted, and the integer ambiguity candidates $\hat{B}$, which meets the following criteria, are searched and fixed:

$$\min \|\hat{B} - b\|^2_{Q_{NN}^{-1}} , \hat{B} \in Z^n \tag{6.11}$$

Different from rounding and LAMBDA which fix the ambiguities to integers, BIE is a method known for its superior performance in minimizing mean square error, and it can be regarded as an integration of weighted integer candidates (Yang et al. 2024). The BIE estimates $\breve{B}$ is given as:

$$\breve{B} = \sum_{z \in Z} z \frac{\exp(-\frac{1}{2}\|z - b\|^2_{Q_{NN}^{-1}})}{\sum_{z \in Z} \exp(-\frac{1}{2}\|z - b\|^2_{Q_{NN}^{-1}})} \tag{6.12}$$

where z is an arbitrary set of n-dimensional integer vectors and can be obtained from LAMBDA. Z is a set which depends on the hyper ellipsoidal region around the float solution with radius correlated to variance and covariance information. In the estimation procedure, the integer vector falls within a given region, as:

$$\|z-b\|^2_{Q^{-1}_{NN}} < \lambda^2 \tag{6.13}$$

where the threshold value λ^2 can be determined with a given confidence level of α, as:

$$P(\|\hat{B}-b\|^2_{Q^{-1}_{NN}} < \lambda^2) = 1-\alpha \tag{6.14}$$

In this chapter, α is set to 10^{-9} to balance the computation burden and the optimal characteristics of BIE (Odolinski and Teunissen 2020).

6.4.2 Partial WL AR

To address the presence of "poor quality" WL ambiguities, several ambiguity candidate selection strategies are proposed and applied to perform partial WL AR in this dissertation. These strategies aim to mitigate the inclusion of noisy candidates in WL AR procedure, thereby reducing the likelihood of erroneous fixes or failures to fix. The thresholds used in these strategies are empirically determined.

(1) Number of continuously observed epoch. In principle, as the number of continuously observed epochs increases, the accuracies of filtered MW-derived WL ambiguity, corresponding variance information, as well as the filtered raw ambiguities will be improved. Therefore, WL ambiguities are fixed only if the number of continuously observed epoch exceeds a predetermined threshold (30 epochs in this study). It should be noted that once a cycle slip is detected, the count for the observed epochs will reset.

(2) SNR check. This process has two parts: SNR cut-off and SNR difference check. The smartphone observation quality is highly correlated with SNR values; therefore, for one satellite, if the SNR values on the first and third frequencies are lower than a given value (e.g., empirical value of 35 dBHz in this study), they will not be involved in PAR. Aside from SNR cut-off, the SNR differences are also checked. A large SNR difference between

two frequencies may lead to an incorrect correlation among the estimates and even a biased solution. Thereby SNR differences larger than 5 dBHz in kinematic datasets will be rejected in PAR in this study.

(3) Elevation angle check. Although elevation angle is less correlated with smartphone range errors, it can somehow represent the atmospheric residuals. Hence, satellite with elevation angle of lower than 30^0 will not be fixed.

(4) Ambiguity consistency check. Ideally, the rounded WL ambiguity should be consistent with the LAMBDA estimated ambiguity. Therefore, for a rounded WL ambiguity with a high rounding success rate (e.g., 0.9 in this study), the ambiguity consistency check is performed. Ambiguities which pass the consistency check will be fixed.

6.4.3 States updating strategy for WL AR solution

After PAR, the successfully fixed WL ambiguities are constrained as virtual observations to update the float solution to fix solution. An automatic ambiguity hold mode is applied, aiming to make full use of correctly fixed ambiguities. When the number of continuously fixed epochs exceeds a specified threshold (set as 5 epochs in this study), and simultaneously, the number of fixed WL ambiguities at the current epoch equals or exceeds that of the previous epoch (as described in Equation (6.15)-(6.16)), then the updated fixed solution is used as a priori information for the subsequent epoch. Conversely, if these conditions are not met, the float solution from the current epoch serves as approximate values for the next epoch.

$$n_{fixedEpoch} \geq threshold1 \tag{6.15}$$

$$n_{fixedAmb}(t) \geq n_{fixedAmb}(t-1) \tag{6.16}$$

Equation (6.15) is introduced to ensure that accidental fix case is not considered as a correct fix. By requiring a certain number of consecutive fixed epochs, the algorithm reduces the risk of occasional and random fix. Equation (6.16) is formulated to maintain the stability of the fixed solution over successive epochs. When a WL ambiguity is correctly resolved, it indicates a favourable condition for subsequent epochs. By mandating that the number of fixed WL ambiguities does not decrease from one epoch to the next, the algorithm ensures that any successful fixes are retained and utilized to support future positioning solutions. Considering the limited number of WL ambiguities available for smartphone AR, even the correct resolution of a single ambiguity can significantly benefit subsequent epochs. Thus, it is crucial to "hold" any correctly fixed ambiguities to the next epoch to capitalize on their positive impact on positioning accuracy and reliability. It should be mentioned that the thresholds used in this study are set empirically, and may differ under very different environment conditions.

A simplified flowchart of the proposed states updating strategy is illustrated in Figure 6.7, in which X denotes the estimated parameter vector. For epoch 1, $X(0)$ is used as a priori information for EKF, and the float solution is $X(1)$, the corresponding fixed solution is $Xa(1)$. If the WL ambiguities are fixed and pass the automatic ambiguity hold check, then the fixed solution is applied as a priori information for the next epoch. Otherwise, the float solution will be adopted.

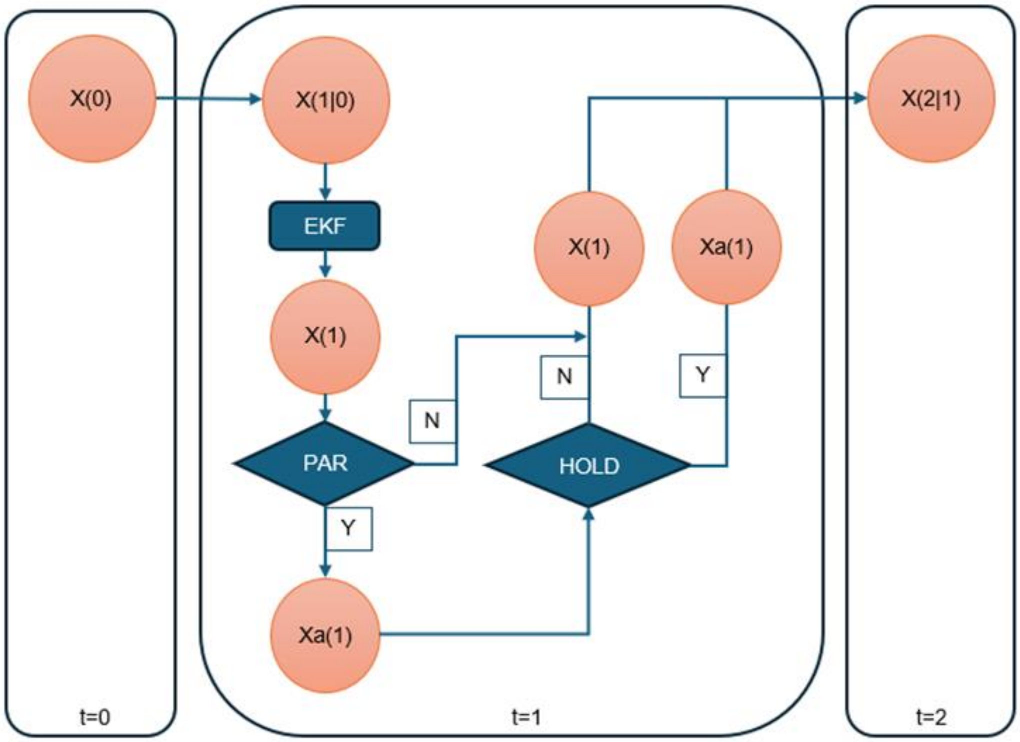

Figure 6.7 Simplified flowchart of states updating strategy for three adjacent epochs. X is the parameters to be estimated. With validation of PAR and HOLD, the ambiguity fixed solution can be used as a priori information for next epoch

6.4.4 Simulated results of correlation between position precision and number of fixed WL ambiguities

For geodetic-grade receivers, the number of ambiguity candidates is significantly larger than that of smartphones. Normally, for a case where the number of ambiguities is smaller than a given value (e.g., minimum of 4 ambiguities in Hu et al. (2020)), AR will not be conducted. However, due to the limited number of WL ambiguities in smartphone observations, it is worth trying to fix even a single WL ambiguity. Therefore, the single-epoch position precision values are calculated when fixing different numbers of WL ambiguities with simulated results using the methods suggested in Hu et al (2023c). The estimated variance and covariance matrix can be derived as (Zhang and Li 2016; Banville and Langley 2013):

$$Q_{yy} = [H^T Q_{\delta y} H]^{-1} \tag{6.17}$$

$$Q_{\delta y} = diag[\ \delta_P^1 \quad \delta_L^1 \quad \cdots \quad \delta_P^s \quad \delta_L^s \quad \delta_{N_{WL}}^1 \quad \delta_{N_{WL}}^2 \quad \cdots \quad \delta_{N_{WL}}^s\ ] \tag{6.18}$$

with H a combination matrix of design matrix from Equation (2.5) and the fixed ambiguity constraints design matrix. The code and phase measurement precisions are set to the usual 1 m and 1 cm, respectively, to simulate the smartphone measurements. The constraints of fixed ambiguities are set to 0.001 m. In Equation (6.17), the upper left 3×3 submatrix of Q_{yy} is the position precision which is utilized for analyzing the position precision.

The geodetic-grade receiver pair P539-P602 with a baseline distance of ~5 km is used to calculate the line-of-sight vectors for 9 GPS satellites, and the satellites are fixed in a sequence of elevation angles. There are 9 GPS satellites in total, and thereby 8 DD WL ambiguities in maximum. Figure 6.8 summarizes the relationship between the number of fixed WL ambiguities and the resulting position precision values. Each scheme, labeled WL-1 through WL-8, corresponds to fixing 1 to 8 DD WL ambiguities, respectively. The figure illustrates that as more WL ambiguities are fixed, the position precision decreases, indicating improved positioning accuracy. Interestingly, even with one WL ambiguity fixed, the single-epoch positioning performance can be improved. This finding underscores the significance of attempting to fix every available WL ambiguity in smartphones. Moreover, the extent of improvement in positioning accuracy varies depending on the number of WL ambiguities fixed, suggesting that each fixed WL ambiguity contributes to the overall enhancement of positioning accuracy to varying degrees. It is worth mentioning that different fixing sequences of WL ambiguities would affect the performance improvement while fixing limited number of WL ambiguities.

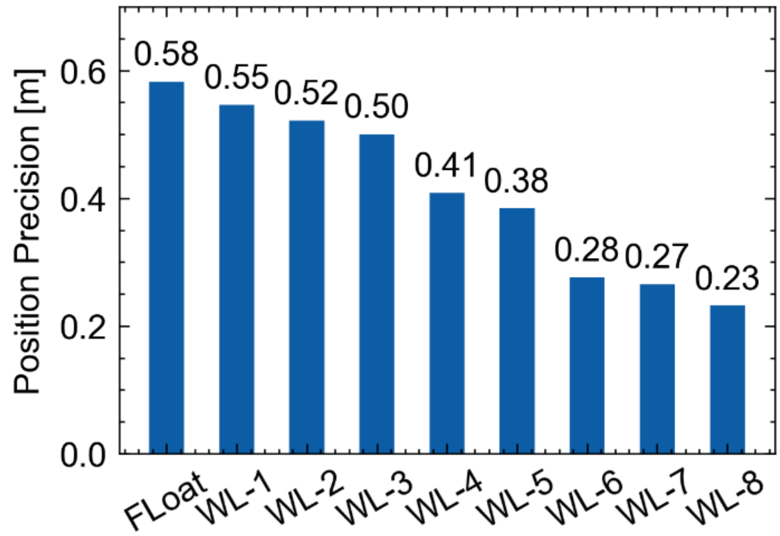

Figure 6.8 Simulated results of effect of number of fixed WL ambiguities on position precision. WL-i denotes fixing a number of i WL ambiguities.

6.5 WL PAR Results

The static and kinematic datasets were processed, and the results were analyzed. The static dataset was processed in both static and simulated kinematic modes. In the static processing mode, the smartphone position remains constant throughout, while in simulated kinematic and kinematic modes, processing noise is introduced to user coordinates. For the static mode analysis, positioning accuracy is defined as the positioning error of the last epoch. And for kinematic positioning performance analysis, the positioning errors at 95th and 50th percentiles, as well as the corresponding rms values, are assessed, as suggested in Google Smartphone Decimetre Challenges (Fu et al. 2020). Additionally, time to first fix (TTFF) is evaluated. In the positioning performance validation, the RTK float ambiguity solution is also produced for comparison purposes. It is worth noting that, in the data processing, when applying LAMBDA to raw DD ambiguities in the experimental data, the ambiguity validation failed (e.g., the ratio value is slightly larger than 1.0). Hence, the conventional narrow-lane AR solution is the same as float solution. Therefore, the float solution is used as a benchmark to validate the proposed method.

6.5.1 WL PAR with static dataset

The static data was processed in both static and simulated kinematic modes. Figure 6.9 shows the time series of the number of satellites with available dual-frequency code and phase measurements for GPS and Galileo, respectively. The number of GPS satellites are slightly more stable than Galileo satellites, and for most time, there are 3-4 GPS dual-frequency satellites available, while an average of 5 Galileo satellites is observed. Considering that between-satellite differencing is performed when fixing the WL ambiguities, and a reference satellite is selected per constellation, the average DD WL ambiguities are 3 and 4 for GPS and Galileo, respectively, which is significantly smaller than those of a geodetic receiver.

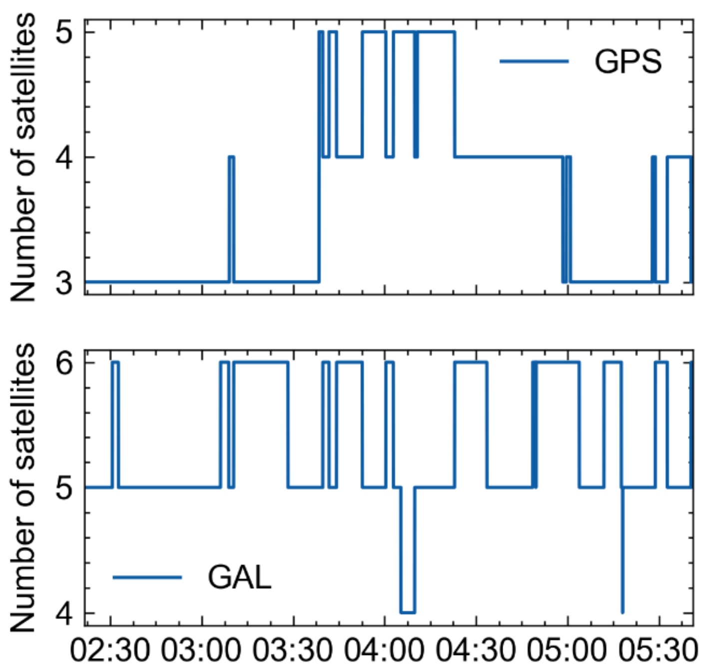

Figure 6.9 Time series of the number of dual-frequency satellites from GPS and Galileo for static data

Figure 6.10 provides insights into the quality of dual-frequency measurements by displaying the distributions of SNR on the first and third frequencies, along with the distributions of SNR differences for all available dual-frequency measurements. The two peaks on the SNR distribution indicate that SNRs on the third frequency are generally several dB-Hz smaller than those on the first frequency. The reason could be that the smartphone antenna is designed for the first frequency and may not be optimized for other frequencies. Consequently, under optimal conditions, such SNR differences might arise because of a smaller noise level compared to realistic driving environments.

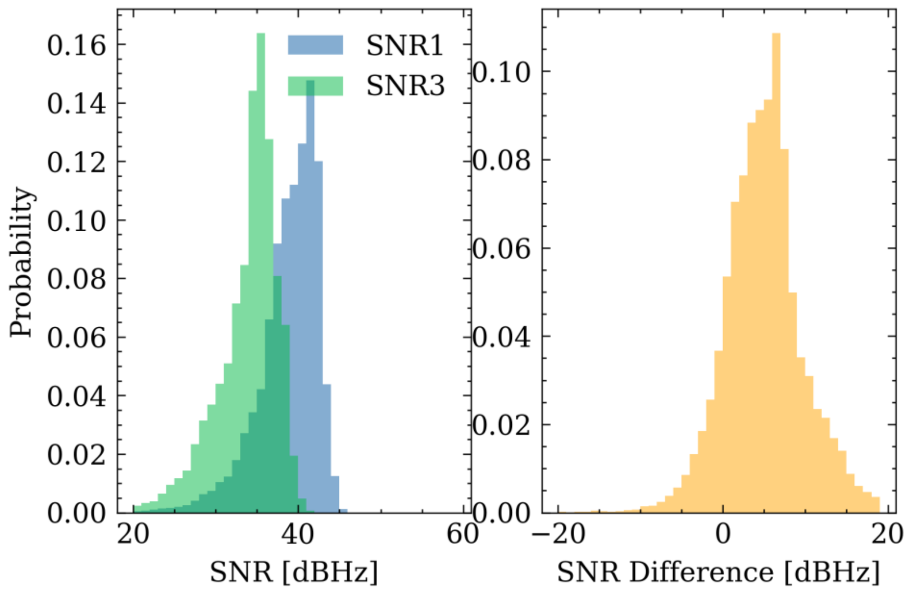

Figure 6.10 C/N_0 (left) and C/N_0 difference (right) distributions for dual-frequency measurements for static data. SNR1 represents SNR values on GPS L1 and Galileo E1, and SNR3 represents those on GPS L5 and Galileo E5a.

The LAMBDA method and PAR are applied to fix WL ambiguities in the static experiment. Figure 6.11 shows the time series of the number of fixed WL ambiguities and the horizontal positioning errors for both float and WL AR solutions. It can be noticed from Figure 6.11 that even when only 2 WL ambiguities are fixed around 02:25, the horizontal positioning performance can be improved from 3 decimetres to the centimetre level. This improvement demonstrates that correctly fixing and holding the ambiguities enhances the overall WL AR solution. These findings validate the effectiveness of the proposed method to fix every possible WL ambiguity.

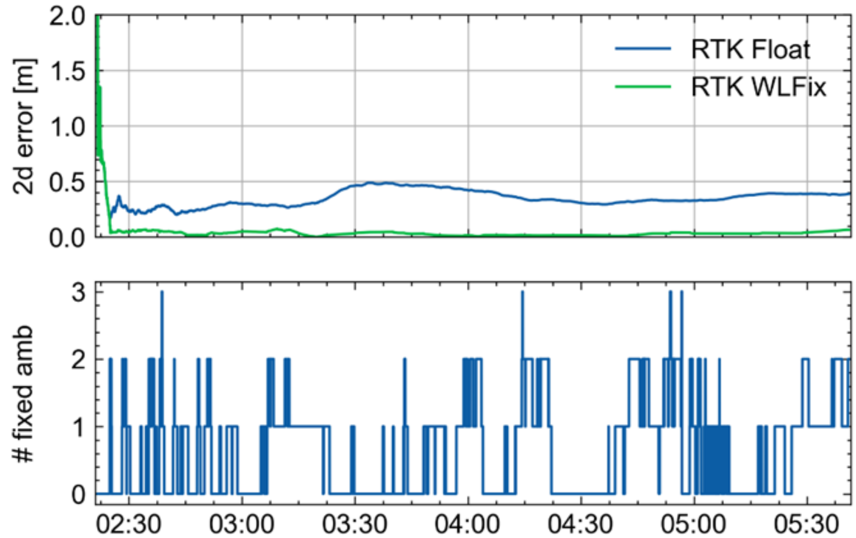

Figure 6.11 Time series of horizontal positioning errors for RTK float (blue) and WL AR (green) solutions and number of fixed WL ambiguities in static mode

Figure 6.12 provides an in-depth investigation of the smartphone static positioning performance in the east (E), north (N), and up (U) components, respectively. Additionally, Table 6.2 summarizes the statistics of the static experiment. The results show that with WL AR, the positioning accuracy improves from 38.8 cm to 6.5 cm in horizontal positioning errors, representing an improvement of 83%. Specifically, the positioning errors reach 3.8, 2.9, and 11.5 cm in E, N, and U components, respectively, for WL AR solution, with a TTFF of 3.3 min. The static WL AR solution shows the potential of smartphone hardware achieving comparable performance as higher-grade receivers.

Table 6.2 Statistics for RTK float and WL AR solution for static experiment

	Positioning errors (cm)				TTFF (min)
	E	N	U	Horizontal	
Float	31.0	23.4	52.4	38.8	-
Static WL AR	6.8	2.9	11.5	6.5	3.3

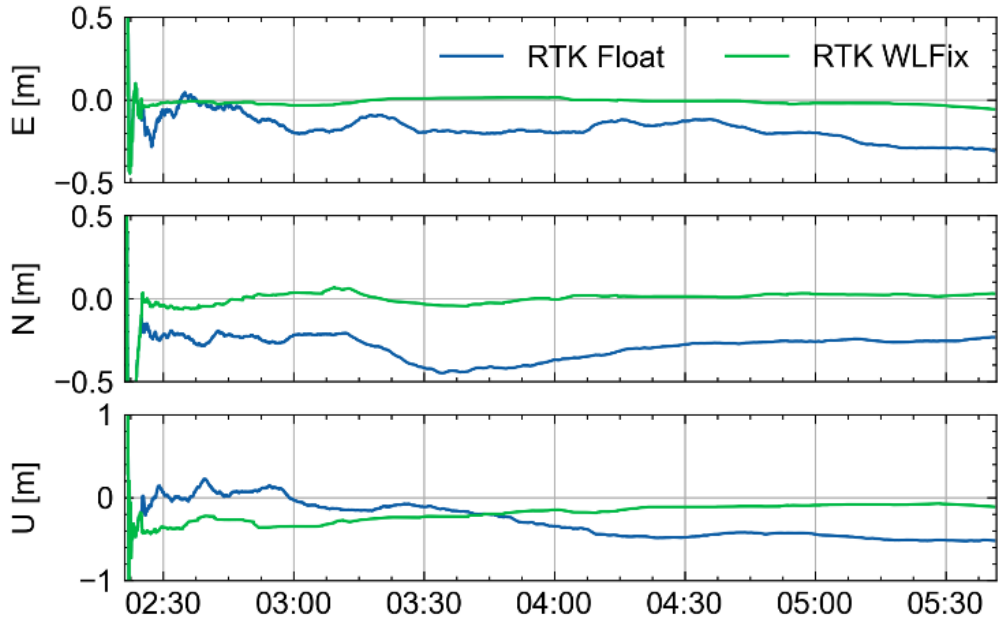

Figure 6.12 Time series of positioning errors in east, north, and up, respectively, for RTK float (blue) and WL AR (green) solutions

Comparing with the static mode, daily life applications often focus more on kinematic user cases such as vehicle positioning and navigation. Therefore, simulated kinematic processing was performed, and the corresponding positioning results are shown in Figure 6.13 and Table 6.3. The WL AR solution in simulated kinematic mode appears to be more stable than the float solution, with the most significant improvements observed after 05:00, resulting in an average improvement of 5 decimetres. For epochs where no WL ambiguity is fixed, the results gradually converge to the float solution, as evidenced during 03:45-04:30. Due to the processing noise applied to user coordinates, the TTFF for the simulated kinematic results is longer than static mode, taking 14.3 min. The 95th percentile horizontal positioning error shows the most obvious improvement, reducing from 1.1 m to 0.7 m for the WL AR solution, while the 50th percentile positioning error can be reduced by 5 cm. These simulated kinematic results indicate that a more stable sub-metre or decimetre horizontal positioning accuracy can be achieved with the proposed method.

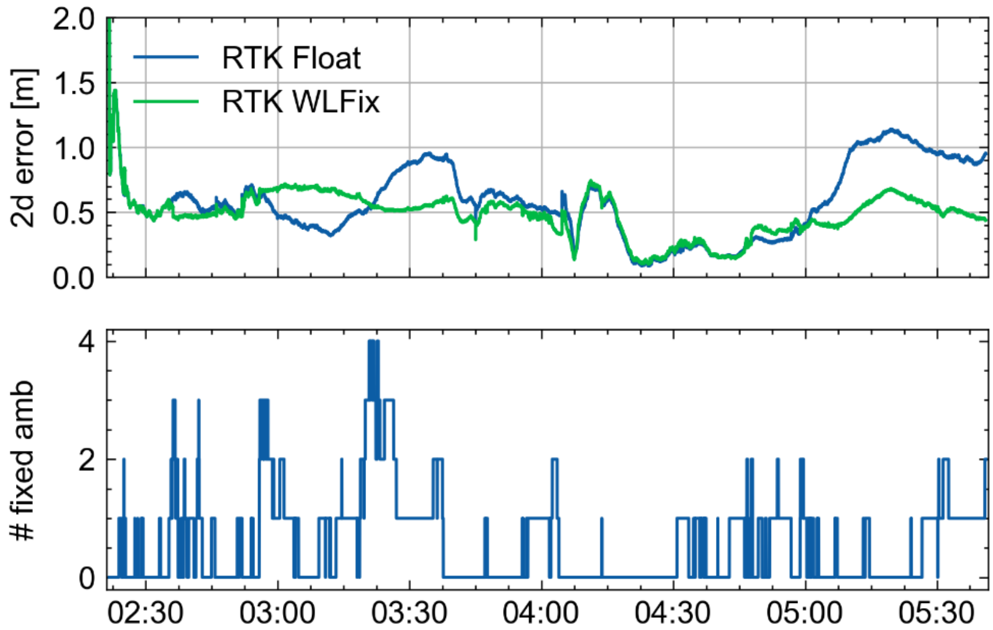

Figure 6.13 Time series of horizontal positioning errors for RTK float (blue) and WL AR (green) solutions and number of fixed WL ambiguities in simulated kinematic mode

Table 6.3 Statistics for RTK float and WL AR horizontal positioning errors, as well as time to first fix for simulated kinematic experiment (units: m)

	95^{th} per.	50^{th} per.	95^{th} per. rms	50^{th} per. rms	TTFF (min)
Float	1.06	0.56	0.61	0.39	-
WL AR	0.69	0.51	0.49	0.38	14.3

6.5.2 WL PAR with kinematic dataset

For realistic driving datasets, the positioning performance of all three datasets is evaluated, and only dataset #1 is selected for measurement quality analysis for the conciseness. The number of available dual-frequency satellites for dataset #1 is first assessed in Figure 6.14. Compared to static data, the variations in the number of dual-frequency satellites are more obvious in driving data, posing a challenge to the continuity of dual-frequency measurements and further affecting the accuracy of filtered MW ambiguity and filtered raw ambiguity estimates. With such variability in dual-frequency measurements, selecting reliable WL ambiguity candidates for fixing becomes important.

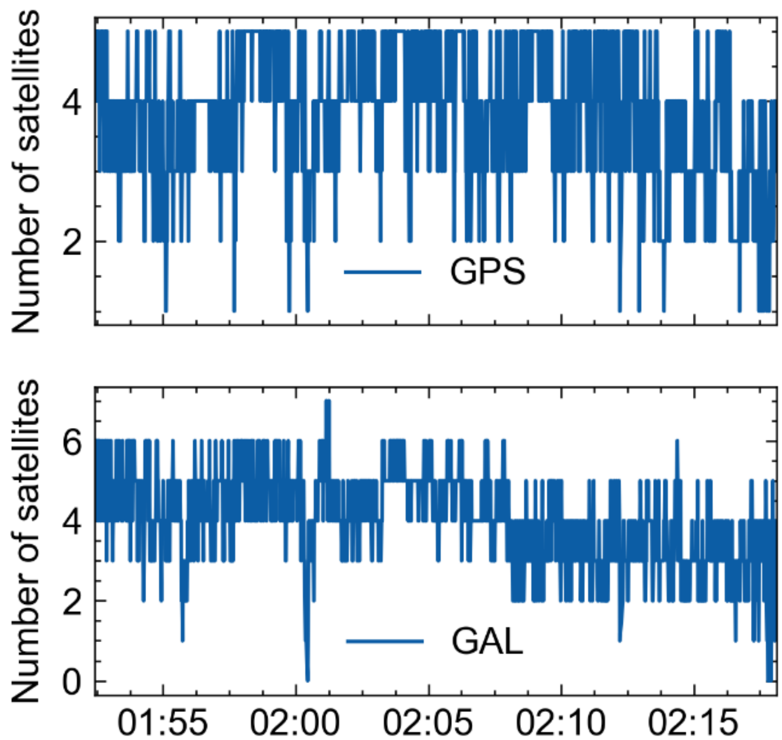

Figure 6.14 Time series of the number of dual-frequency satellites from GPS and Galileo for smartphone dataset #1

Different from static data, the SNR distributions on the first and third frequencies seem to be more consistent. The reason might be that in the driving environment, where smartphones are placed in cars and mounted on dashboards, the noise level becomes larger. Therefore, the antenna design plays less role in receiving signals from different bands compared to multipath and noise. Hence, in kinematic data processing, the SNR difference check is performed when selecting WL ambiguity candidates for PAR.

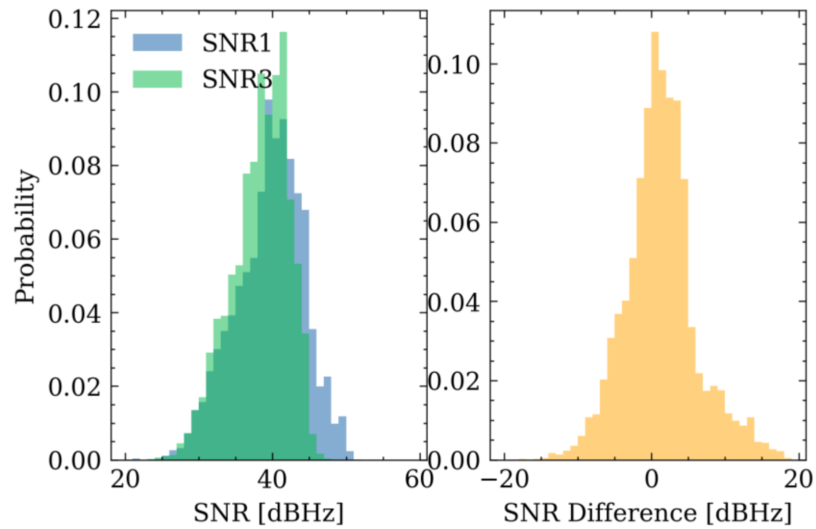

Figure 6.15 SNR (left) and SNR difference (right) distributions for dual-frequency measurements for dataset #1

When applying the LAMBDA method in the kinematic datasets, the WL AR solution cannot pass the ratio test (3 is used) for most of the epochs. Combining the integer candidates and the float solution, BIE solution can be regarded as a weighted solution and is expected to be more robust in realistic and noisy driving data. Figures 6.16-6.18 show the time series of horizontal positioning errors for datasets #1-3, respectively, with BIE applied. For all the results, two significant spikes observed, which are caused by two overpasses mentioned before. The positioning results show that the WL ambiguities can be correctly fixed for different periods in different datasets. For dataset #1, correct fixes can be observed before the first spike (~02:01) and after the second spike (~02:12), with an average improvement of 2 decimetres. However, after the first spike, due to the poor float solution, the BIE does not work well, resulting in the incorrectly fixed WL ambiguities and decreased positioning performance for about 3 minutes. Notable improvements can be observed in dataset #2, in which after correctly fixing the WL ambiguities from 00:59, the WL AR solution outperforms the float solution with a maximum improvement of half a metre. The kinematic results indicate that the WL ambiguities can be fixed in a realistic driving environment, and the AR validation needs to be carefully conducted, especially when the smartphone is in obstructed environments such as suburban areas.

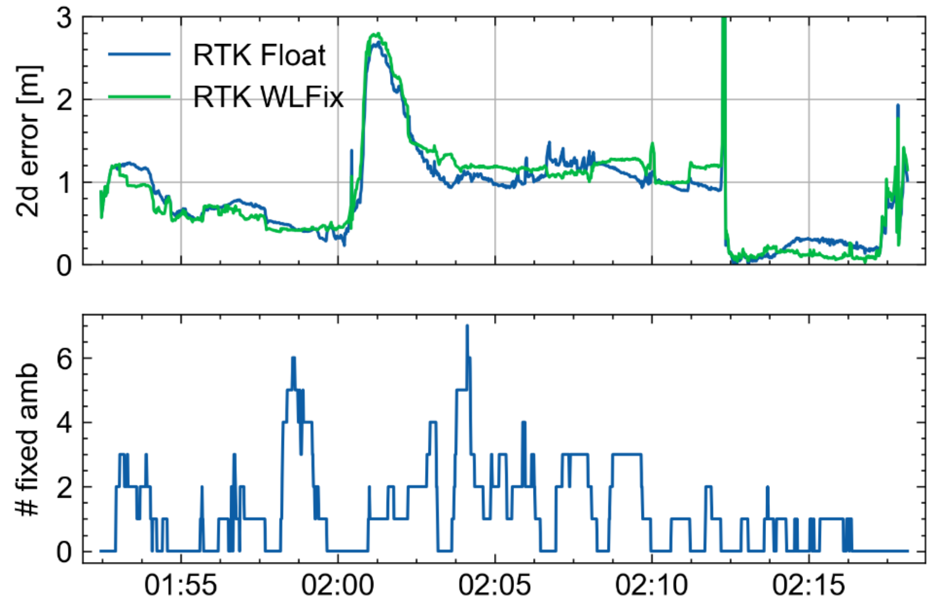

Figure 6.16 Time series of horizontal positioning errors for RTK float (blue) and WL AR (green) solutions and number of fixed WL ambiguities for dataset #1

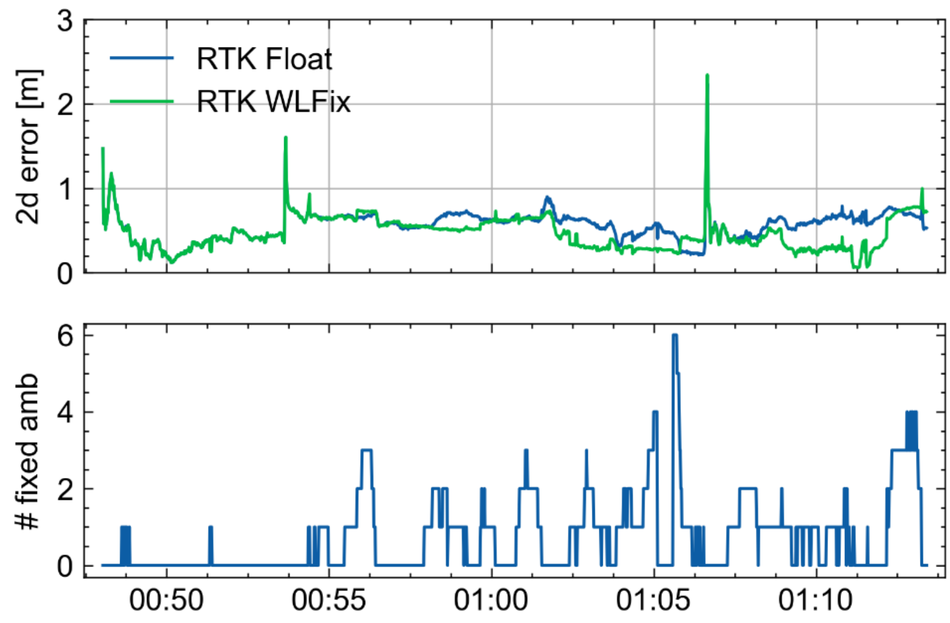

Figure 6.17 Time series of horizontal positioning errors for RTK float (blue) and WL AR (green) solutions and number of fixed WL ambiguities for dataset #2

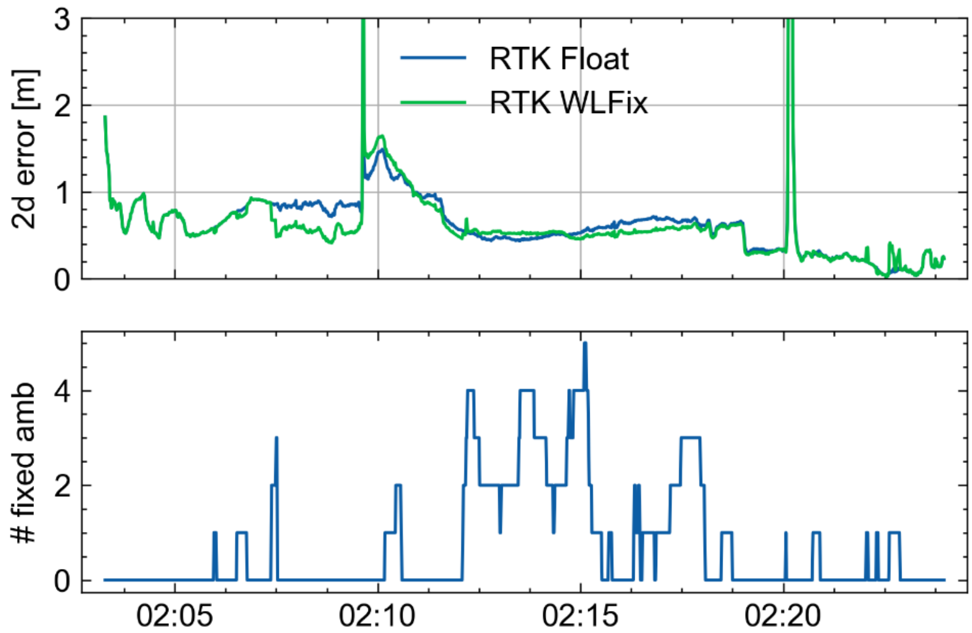

Figure 6.18 Time series of horizontal positioning errors for RTK float (blue) and WL AR (green) solutions and number of fixed WL ambiguities for dataset #3

Table 6.4 Summarizes the statistics for all kinematic datasets with RTK float and WL AR solutions. To validate the performance of the proposed WL AR solution under different environments, the data collection regions are divided into suburban and other regions. From the statistics it is obvious that the most significant improvements are in regions except suburban, representing positioning performance enhancements of decimetre-level. It is challenging to validate the fixed WL ambiguities in suburban conditions; however, at the same time, the biggest improvement of 0.79 m can also be noticed for 95th percentile horizontal positioning errors in dataset #2 under suburban environments. The results further infer that once the WL ambiguities are correctly fixed, there is a great potential of achieving sub-metre and decimetre-level positioning accuracy even under obstructed environments.

Table 6.4 Statistics for 3 smartphone kinematic datasets with RTK float and WL AR solutions under suburban environment and other regions (units: m)

Dataset ID	Scheme	Other regions				Suburban			
		50th per.	95th per.	50th per. rms	95th per. rms	50th per.	95th per.	50th per. rms	95th per. rms
1	Float	0.47	1.19	0.28	0.57	1.08	2.44	0.51	0.62
	WL AR	0.45	1.07	0.25	0.52	1.19	2.61	0.54	0.57
2	Float	0.64	0.91	0.34	0.61	0.60	1.22	0.32	0.63
	WL AR	0.53	0.91	0.33	0.54	0.54	0.43	0.34	0.56
3	Float	0.52	0.75	0.38	0.51	0.62	0.73	0.45	0.51
	WL AR	0.38	0.77	0.28	0.41	0.55	0.73	0.36	0.39

6.6 Summary

Resolving integer ambiguity in GNSS carrier phase measurement for smartphones is problematic for a long time due to noisy observations. With a longer wavelength for wide-lane ambiguities, which are ~75 cm for GPS L1/L5 and Galileo E1/E5a, a wide-lane ambiguity resolution with partial fixing and automatic ambiguity hold strategy is proposed to improve smartphone positioning accuracy. Three AR methods including rounding, LAMBDA, and BIE are introduced first, and the proposed algorithm is validated with both static data collected in an open sky environment and kinematic data collected in realistic driving environments.

Firstly, with simulated results, the relationship between position precision and the number of fixed WL ambiguities is assessed. The correlation infers that even with one WL ambiguity correctly fixed, the positioning performance can be improved compared to float solution, this result motivates the proposed strategy of fixing every possible WL ambiguity in smartphone GNSS measurements.

The static data were processed in both static and simulated kinematic modes. The static experiment indicates an improvement of 83% in horizontal positioning accuracy when WL AR is performed compared to float solution, and the WL AR solution can reach positioning accuracy of 6.8, 2.9, and 11.5 cm in E, N, and U, respectively, with TTFF of 3.3 min. The simulated kinematic results show that, the positioning errors with WL AR are more stable than those of float solution, and once the WL ambiguities are correctly fixed, the 95th percentile horizontal poisoning accuracy can be improved by ~4 decimetres.

For data collected under realistic driving environments, the continuity of dual-frequency measurements becomes worse. However, the positioning results show that the WL ambiguities can still be fixed for some periods. The improvements of WL AR solution compared to float solution vary from several centimetres to half a metre. The most significant improvement is for dataset #2, and the 95th percentile horizontal positioning error is reduced from 1.2 m to 0.4 m in suburban environment. This further demonstrates the feasibility of fixing WL ambiguities with smartphone GNSS measurements in realistic environments.

7 CONCLUSIONS AND RECOMMENDATIONS

Based on the work described in Chapters 3-6 in this dissertation, conclusions are first drawn. Moreover, some extended research can be conducted based on the research topics in this dissertation, and therefore, corresponding recommendations are presented.

7.1 Conclusions

Access of smartphone raw GNSS measurements enables academic and industrial fields to enhance smartphone positioning accuracy by utilizing pseudorange and carrier phase observations. Unlike measurements from a geodetic receiver, smartphone observables suffer higher multipath, higher noise level, and frequent cycle slips, due to the embedded linearly polarized antenna, especially in obstructed urban environments. Therefore, research has been carried out in aspects of, e.g., measurement assessment, measurement quality optimization, cycle slip detection, stochastic modelling, outlier detection and rejection, and ambiguity resolution. While some published research was conducted under optimal environments such as open sky areas, as well as using external antennas, this dissertation focuses on enhancing smartphone positioning accuracy in driving environments considering a more realistic application where the smartphones are mounted on the car dashboard. Works including smartphone range error characteristics, cycle slip detection, stochastic modelling, outlier detection, and wide-lane partial ambiguity resolution were carried out in this dissertation. Smartphone sub-metre positioning accuracy in realistic environments in achieved by addressing research questions proposed in Chapter 1.

7.1.1 Smartphone range error characteristics

A comprehensive understanding of GNSS measurement quality is the premise of further utilizing these observations in positioning. While most quality assessments were carried out by analyzing the zero-baseline pre-fit residuals, or by investigating the post-fit residuals after positioning, this dissertation uniquely proposes to derive smartphone range errors under realistic environments with a collocated geodetic-grade receiver and pre-measured lever arm parameters. The following research questions were answered in Chapter 3.

(1) *How does the smartphone range error distribution behave on different signal frequencies and constellations?*

A constellation- and frequency-specific analysis of derived range errors indicates that measurement quality on different signal frequencies and constellations behave differently. For both smartphones and geodetic receivers, the range error standard deviations for the third frequency (GPS L5 and Galileo E5a) are smaller than the first frequency (GPS L1 and Galileo E1), inferring that measurements on the third frequency may have higher precisions. As for the differences among constellations, for the test dataset, the range errors for GLONASS satellites are the biggest, exhibiting standard deviation of 11.8 m, while range error standard deviations for GPS, Galileo, and BDS are 5.4, 4.5, and 3.4 m, respectively, showing similar measurement quality. The results are similar to the results in Liu et al. (2019).

(2) *What is the relationship among range errors, satellite elevation angles, and C/N_0 values?*

Significant range error decreasing trends are observed when C/N_0 increases for both smartphone and geodetic receiver, whereas an elevation angle-related trend is observed only for geodetic receiver. Moreover, different correlation strengths are noticed for different frequencies. For smartphone GNSS measurements, the range errors are more correlated with C/N_0, especially for the first frequency, while almost no elevation angle correlation is noticed. With fitting functions between range errors and C/N_0, smaller range errors are observed for the third frequency again. This result indicates that a frequency-specific measurement weighting function can be fitted to improve smartphone positioning performance. The high correlation between range errors and C/N_0 is reported in reported in Banville et al. (2019) and Zangenehnejad and Gao (2021), however, the different trends in correlation have not been investigated in existing research.

(3) *How does range error vary under different multipath profiles in real driving environments? Do any differences exist with different mounting location?*

Different multipath profiles would have various influences on the received signals. The data collection region is divided into open sky, suburban, and vegetated areas. Results show that the buildings and trees limited sky visibility and blocked GNSS signals. In suburban environments, range errors are the biggest even for signal azimuths without building blockage. While driving in the vegetated area, the signal blockage by the tree has limited impacts on range errors of other tracked satellites. The mean values of range errors are 0.8, 2.2, and 1.5 m on the first frequency when the smartphone is under open sky, suburban, and vegetated areas, respectively, while those are 0.9, 1.2, and 1.4 m for the third frequency. Moreover, a clearer and higher distribution centralization for the range errors when smartphone was placed on the roof is observed compared to those on the dashboard. There have been descriptions on how the environment affects the smartphone GNSS measurement quality, this contribution, for the first time, provides a comprehensive and detailed analysis on the quantitative range errors under complex GNSS obstructed environments.

(4) *What is the correlation between smartphone pre-fit residuals and range errors?*

The double-differenced RTK pre-fit residuals are used to assess the correlation. It is found that the range errors and pre-fit residuals for the first frequency have a higher correlation than the third frequency. GLONASS satellites have the higher correlation coefficients despite larger range errors. It should also be noted that the pre-fit residuals are software and algorithm dependent, but can still serve as an indicator for measurement quality.

7.1.2 Smartphone cycle slip detection

The introduction of carrier phase measurements in smartphone data processing provides for improved positioning performance, but at the same time, possible cycle slips in phase measurements can also degrade solution accuracy. The crucial role of cycle slip detection in precise positioning motivated the work in Chapter 4, in which the MW combination, GF combination, CMP, as well as the conventional Doppler cycle slip detection methods are investigated, analyzed, and assessed. A novel modified Doppler detection method was proposed to deal with the clock inconsistency issue in TDCP and Doppler measurements for phones such as the Xiaomi Mi8 and Samsung S20. The following research questions were answered in Chapter 4.

(1) Are commonly used cycle slip detection methods applicable to smartphones? And what are the mathematical form of their test values?

For smartphone kinematic datasets, conventional polynomial fitting method and high-order differencing method are not applicable because they are mainly used in static data. The limitation of CMP and MW methods in smartphone is the large code noise level. Moreover, MW method cannot detect the cycle slips when they are the same for both frequencies, and GF method is not sensitive when $\lambda_1 N_1^s = \lambda_5 N_5^s$. Besides, the TDCP and Doppler clocks are not synchronized for specific smartphones, resulting in the non-applicable of conventional Doppler cycle slip detection method. The mathematical forms of test values are derived from raw GNSS observation equations, which further provides information for sensitivity analysis.

(2) What are the noise levels of different cycle slip detection methods and how sensitive they are for smartphone measurements?

With derived mathematic forms of different CS detection methods, one cycle change in N_1 would lead to test value changes of 0.2 m, 0.7m, 0.2 m, and 1 cycle for CMP, MW, GF, and Doppler methods, respectively. While one cycle of N_5 can result in changes of 0.3 m, 0.7 m, 0.3 m, and 1 cycle for those methods. Depending on the use of pseudorange and phase measurements, the noise levels of CMP, MW, GF, and Doppler methods are $\sqrt{2}\sigma_P$, $0.714\sigma_P$, $2\sigma_L$, and $\Delta t\sigma_D$, respectively.

(3) If the cycle slip detection methods are not applicable, what is the solution, and how does the improved method perform?

MW and GF methods only work for dual-frequency measurements. For two situations that (i) many of smartphone GNSS measurements are single-frequency, and (ii) measurements from one frequency suffer frequent loss, cycle slip detection method which work for single-frequency is necessary to be improved. Based on conventional Doppler cycle slip detection method, a novel modified method is proposed which regards the test value as a mean shift model which follows normal distribution, with median constellation and frequency-specific test values the means of the Gaussian distribution. Results show that, the noisy pseudorange measurements result in the insensibility of MW and CMP methods for small cycle slips. The GF method can detect small cycle slip which is only one cycle. Compared to conventional cycle slip detection methods, the proposed Doppler cycle slip detection method has the best performance, with all the simulated cycle slips settings vary from 1-67 cycles detected.

7.1.3 Smartphone stochastic modelling and outlier detection

Smartphone GNSS measurements in suburban environments suffer from severe multipath and noise, posing a challenge in dealing with the potential outliers. Using the range errors derived from smartphones, the characteristics of range errors can be further utilized to optimize the stochastic model and improve outlier detection in user environments, which is detailed discussed in Chapter 5. Compared to existing algorithms, a new adaptive phase/code precision ratio scheme has been developed. Furthermore, a scale factor is utilized to deal with over-optimistic in the fitted weighting scheme functions, and an adaptive a posteriori residual rejection method that considers the number of rejected measurements is proposed. The following research questions were answered in Chapter 5.

(1) How does the measurement precision ratio between phase and code affect the solution?

Current research on stochastic modelling usually focuses on building weighting functions based on measurements from different satellites, however, measurement precision ratio between phase and code is also an important factor. According to the positioning results, a higher weight on the phase measurements sometimes has larger positioning errors during convergence time. In contrast, it performs better when the ambiguities converge. Therefore, an adaptive phase/code precision ratio which is a function of continuously observed epochs is proposed. With 13 datasets processed, the proposed ratio scheme can reduce the 68th and 95th horizontal positioning errors by 4 cm and 3 cm, respectively, compared to a fixed ratio of 100. The percentage of horizontal positioning errors within 1 m can be improved by 7% (from 50% to 58%).

(2) Whether the weighting scheme based on range errors perform better than conventional SNR-based weighting scheme, and what is the corresponding improvement?

With range errors derived from 7 training datasets, constellation- and frequency-specific weighting functions are fitted using the sum of the median and two times standard deviations. An over-optimistic issues is observed in the fitted functions, in which the measurements on the third frequency have been put over-high weights especially for smaller SNRs. Hence, a scale factor as a function of SNR is introduced. With 6 experiment datasets processed, the fitted weighting scheme outperforms conventional C/N_0-based and elevation-dependent weighting schemes, representing horizontal positioning accuracy improvements of 1.4 dm and 1.5 dm for 68th and 95th percentiles, respectively, compared to conventional SNR-based weighting scheme. While existing research usually use the same smartphone for weighting function fitting and position validation, this contribution utilizes different datasets for fitting and positioning, improving the universality of the fitted weighting scheme.

(3) How does post-fit residual rejection contribute to the solution? Is a fixed rejection threshold value better than an adaptive threshold?

In GNSS data processing, post-fit residual rejection is normally applied to filter out outliers, as a correlation between post-fit residuals and range errors was observed in Yi et al. (2024). Post-fit residual rejection threshold is fitted as a function of SNR, and with considering the rejected number of measurements, the calculated threshold is further adapted. With proposed method, the number of positioning epochs that falls into 1 m horizontal positioning accuracy increases by 5% compared to a fixed rejection threshold of 10 m.

7.1.4 Smartphone ambiguity resolution

The noisy smartphone GNSS measurements prevent user from obtaining decimetre-level positioning performance in realistic environments. Recovering the integer property of ambiguity shows a great potential in achieving high accuracy solution. Nevertheless, the inaccurate ambiguity estimates, and short wavelengths are the main barriers in conducting ambiguity resolution. To realize AR, detailed analysis were carried out in Chapter 6. Smartphone raw GNSS ambiguities are assessed, and a WL PAR strategy is proposed. The following research questions were answered in Chapter 6.

(1) What is the ambiguity availability and stability for datasets in realistic driving environments? Do they vary with different positioning methods?

With RTK, PPP, and PPP-RTK, smartphone GNSS raw ambiguities are estimated and analyzed. Results show that only single-frequency GLONASS and BDS satellite measurements can be tracked for a S21 smartphone GNSS chip, while dual-frequency observations for all Galileo satellite are available. Moreover, realistic environments pose challenge in the continuity of the dual-frequency measurements. The estimated ambiguities with different positioning methods exhibit similar trends, among which the variations of ambiguity parameters can even reach one cycle.

(2) Whether the raw ambiguity estimates stable enough to be fixed? And if the raw ambiguities are hard to fix, what about the wide-lane ambiguities?

Due to the large variations in raw ambiguities, it would be more realistic to fix the WL ambiguities rather than narrow-lane ones. With a wavelength of ~75 cm (GPS L1/L5, Galileo E1/E5a), WL ambiguities can be derived from MW combination or by directly subtracting estimated ambiguities on the first and third frequencies. A simulated results indicate that, even with one WL ambiguity correctly fixed, the position precision can be improved. The more WL ambiguities been fixed, the lower the positioning errors.

(3) *What ambiguity resolution methods are more suitable in fixing smartphone ambiguities? Are there differences in AR strategies for smartphones compared to geodetic-grade receivers?*

There are three commonly used AR methods: rounding, LAMBDA, and BIE. Rounding to the nearest integer is unreliable especially for the noisy smartphone measurements. With a correct validation of LAMBDA-derived ambiguities, AR solution with LAMBDA is expected to have the best performance. However, in smartphone realistic applications, the validation of LAMBDA remains a challenge, therefore, BIE is adopted as it can be regarded as a weighting float and fixed solution. The AR strategies are different for smartphones compared to geodetic-grade receivers, as suggested in the simulated results, it is worth trying to even fix one WL ambiguity in smartphones. Moreover, detailed PAR strategies which contains number of continuously observed epoch, SNR check, elevation angle check, and ambiguity consistency check are proposed, as well as a novel automatic parameter update strategy is introduced.

(4) *How accurate are the solutions when fixing ambiguities compared to float solutions?*

With both static and kinematic smartphone data, the proposed WL PAR algorithm is assessed and validated. Static results show an improvement of 83% in horizontal when RTK WL AR is conducted, and the positioning accuracies can reach 6.8, 2.9, and 11.5 cm in E, N, and U, respectively. For kinematic data collected in realistic driving environments, the WL AR solutions exhibit higher stability than float solutions, and with the fixed WL ambiguities, the solutions can be improved to different extents, reducing positioning errors by several centimetres to half a metre. The most significant improvement is for dataset #2, and the 95th percentile horizontal positioning error is reduced from 1.2 m to 0.4 m in suburban environment.

7.2 Recommendations

Despite the significant progress made in achieving smartphone decimetre-level positioning performance with native embedded antennas, some extended research can be developed based on the contributions and ideas proposed in this dissertation.

7.2.1 In-depth signal characterization

Correctly characterizing GNSS signals allows user to reject or de-weight the potential bad-quality measurements in their own software. Although there is a comprehensive investigation of range errors under different environments in this dissertation, in which the buildings and trees have different influences on the measurement quality for satellite from different directions, it raises potential research on in-depth signal characterization. To be specific, the surrounding environments may cause non-line-of-sight (NLOS) signals, and by investigations such as, e.g., range errors from NLOS and LOS signals, signal strength change when a signal turns from a LOS to NLOS signal, one may be able to differentiate the signals in real-time applications. Moreover, for applications where smartphones are placed in the car, quality of signals that come from different directions may differ. For instance, the materials of a car roof and windshield are different, which may impact the signal quality differently. Thereby, how the range errors behave when a signal comes from heading direction compared to signal from zenith direction is also worth investigation. With these assessments, when there are redundant measurements, one would be more flexible when selecting proper measurements to process.

7.2.2 Smartphone cycle slip detection combination

The proposed cycle slip detection method in this dissertation is validated with simulated cycle slips, as it would be difficult to find specific cycle slips in real data. Moreover, an 100% detection cannot be guaranteed using the existing detection methods. Therefore, the first potential research topic regarding CS detection would be the performance validation with realistic datasets, and different combinations of existing methods may have various efficiencies in different grades of datasets. When processing smartphone datasets, it was found that the detection thresholds are hard to determine because it is highly measurement quality dependent. Therefore, in the future research, different cycle slip detection thresholds can also be applied to adapt the change of environments.

7.2.3 Environmental-related stochastic modelling

Based on the range errors derived from realistic environments, constellation- and frequency-specific weighting functions are fitted in this dissertation. The fitted functions use range errors from all environments. However, it was found in Chapter 3 that the range errors are also environment-dependent, which raises a potential research topic on environmental-related stochastic modelling for advanced smartphone applications where users are expecting a higher accuracy. With the development of artificial intelligence (AI), AI-aided context-awareness becomes possible. Through natural language processing and computer vision, smartphones can identify user's surroundings (Bisnath and Aggrey 2024; Pichler et al. 2004). With combination of environmental-related stochastic modelling and context-awareness, smartphone GNSS precise positioning performance is expected to be further improved.

7.2.4 Ambiguity resolution optimization

Fixing WL ambiguities in smartphones shows significant improvement in positioning performance especially for the static experiment in this dissertation. However, in data processing, it was found that the kinematic WL AR solutions were sensitive to the ambiguity candidate selecting strategy and AR validation. Therefore, in the future research of smartphone AR, attentions should be paid. Moreover, due to the smartphone chipset limitations, only limited number of WL ambiguities is available in this dissertation, with the upgrading of smartphone chipsets, more dual-frequency measurements would further improve the WL AR solution. Last but not least, nowadays BDS triple-frequency measurements can be observed in some regions such as mainland China with smartphones, with an extra constellation, the WL AR solution can be further improved and may thereby benefit the fixing of raw ambiguities.

7.2.5 Positioning with varied datasets

Noting that the positioning results are based on the datasets collected in and around York University, Canada, it would be interesting to explore whether the developed algorithm is applicable to datasets in other areas. For instance, the data trajectory environments would change in a different region, and therefore, the range error behaviour would be different. How the range errors change when the overpass is longer, and the surrounding building is higher, is worth investigating. Moreover, whether the fitted weighting functions still perform better than the conventional weighting scheme needs to be evaluated, to what extent and how the fitted coefficients will change when introducing datasets from different areas is worth investigation. The public Google smartphone datasets provide different trajectories with different brands of phones, therefore, future research could focus on processing these Google datasets to further validate and evaluate the proposed algorithms.

REFERENCES

Banville S, Lachapelle G, Ghoddousi-Fard R, Gratton P (2019) Automated processing of low-cost GNSS receiver data. *Proc. ION GNSS 2019*, Institute of Navigation, Miami, Florida, USA, September 16-20, 3636-3652.

Banville S, Langley R (2013) Mitigating the impact of ionospheric cycle slips in GNSS observations. *Journal of Geodesy*, 87, 179-193.

Bisnath S (2000) Efficient, automated cycle-slip correction of dual-frequency kinematic GPS data. *Proc. ION GNSS 2000*, Institute of Navigation, Salt Lake City, UT, September, 145-154.

Bisnath S, Aggrey J (2024) Current Limitations and Prospects for Smartphone GNSS Precise Positioning. *Proc. ION ITM 2024*, Institute of Navigation, Long Beach, California, USA, January, 1-24. https://doi.org/10.33012/2024.19560

Boehm J. Niell A. Tregoning P. Schuh H (2006) Global mapping function (gmf): a new empirical mapping function based on numerical weather model data. *Geophysical Research Letters*, 25.

Blewitt G (1990) An automatic editing algorithm for GPS data. *Geophys. Res. Lett*, 17, 199-202.

Brunner F, Hartinger H, Troyer L (1999) GPS signal diffraction modelling: the stochastic SIGMA-Δ model. *J Geodesy*, 73, 259-267.

Brodie K (2001) Improved Chi-square fault detection for GPS Navigation. *Proc. ION NTM 2001*, Institude of Navigation, Long Beach, California, USA, January 22-24, 438-441.

Cai C, Liu Z, Xia P, Dai W (2013) Cycle slip detection and repair for undifferenced GPS observations under high ionospheric activity. *GPS Solutions*, 17, 247-260, doi:10.1007/s10291-012-0275-7.

Cui B, Wang J, Li P, Ge M, Schuh H (2022) Modeling wide-area tropospheric delay corrections for fast PPP ambiguity resolution. *GPS Solutions*, 26, 56. https://doi.org/10.1007/s10291-022-01243-1.

Collins P, Lahaye F, Heroux P, Bisnath S (2008) Precise point positioning with ambiguity resolution using the decoupled clock model. *Proc. ION GNSS 2008*, Institute of Navigation, Savannah, GA, USA, September 16-19, 1315-1322.

de Ponte Müller F, Steingass A, Strang T (2013) Zero-baseline measurements for relative positioning in vehicular environments. *Proceedings of the 6th EuropeanWorkshop on GNSS Signals and Signal Processing*, Neubiberg, Germany, December 2013, 5-6.

Everett T, Taylor T, Lee D K, Akos D M (2022) Optimizing the Use of RTKLIB for Smartphone-Based GNSS Measurements. *Sensors*, 22(10): 3825.

Fu G, Khider M, Van Diggelen F (2020) Android raw GNSS measurement datasets for precise positioning. *Proc. ION GNSS 2020*, Institute of Navigation, September 21-25, 1925-1937.

Gao R, Xu L, Zhang B, Liu T (2021) Raw GNSS observations from Android smartphones: Characteristics and short-baseline RTK positioning performance. *Measurement Science and Technology*, 32(8), 084012.

Geng J, Li G, Zeng R, Wen Q, Jiang E (2018) A comprehensive assessment of raw multi-GNSS measurements from mainstream portable smart devices. *Proc. ION GNSS 2018*, Institute of Navigation, Miami, Florida, USA, September 24-28, 392-412.

Geng J, Li G (2019) On the feasibility of resolving Android GNSS carrier-phase ambiguities. *Journal of Geodesy*, 93(12), 2621-2635.

Ge M, Gendt G, Rothacher M, Shi C, Liu J (2008) Resolution of GPS carrier-phase ambiguities in precise point positioning (PPP) with daily observations. *Journal of geodesy*, 82, 389-399.

Hauschild A, Montenbruck O, Sleewaegen J, Huisman L, Teunissen P (2012) Characterization of compass M-1 signals. *GPS Solutions*. 2012;16:117–126. doi: 10.1007/s10291-011-0210-3.

Hu J, Li P, Bisnath S (2024) Enhancing smartphone precise point positioning to sub-meter accuracy in suburban environments: a new stochastic model and outlier diagnosis. *GPS Solutions*, 28, 112.

Hu J, Li P, Zhang X, Bisnath S, Pan L (2022) Precise point positioning with BDS-2 and BDS-3 constellations: ambiguity resolution and positioning comparison. *Adv. Space Res*. 2022, 70, 1830-1846.

Hu J, Yi D, Bisnath S (2023a) A Comprehensive Analysis of Smartphone GNSS Range Errors in Realistic Environments. *Sensors*, 23(3), 1631.

Hu J, Bisnath S (2023b) Preliminary Assessment of Improved Smartphone GNSS Quality Control Methods Based on Range Errors. *Proc. ION GNSS 2023*, Institute of Navigation, Denver, Colorado, USA, 11-15 Sept, pp 85-98.

Hu J, Cui B, Li P, Bisnath S, Zheng K (2023c) Exploring the Role of PPP-RTK Network Configuration: A Balance of Server Budget and User Performance. *GPS Solutions*, 27, 184. https://doi.org/10.1007/s10291-023-01518-1.

Hu J, Li P, Bisnath S (2023d) Towards GNSS Ambiguity Resolution for Smartphones in Realistic Environments: Characterization of Smartphone Ambiguities with RTK, PPP, and PPP-RTK. *Proc. ION GNSS 2023*, Institute of Navigation, Denver, Colorado, USA, 11-15 Sept, pp 2698-2711.

Hu J, Zhang X, Li P, Ma F, Pan L (2020) Multi-GNSS fractional cycle bias products generation for GNSS ambiguity-fixed PPP at Wuhan University. *GPS Solutions*, 24, 1-13.

Jiang Y, Gao Y, Ding W, Liu F, Gao Y (2023) An improved ambiguity resolution algorithm for smartphone RTK positioning. *Sensors*, 23(11), 5292.

Joerger M, Pervan B (2016) Fault detection and exclusion using solution separation and chi-squared ARAIM. *IEEE Transactions on Aerospace and Electronic Systems*. 52 (2), 726-754. doi: 10.1109/TAES.2015.140589.

Kouba J, Héroux P (2001). Precise Point Positioning Using IGS Orbit and Clock Products. *GPS Solutions*, 2001,5(2):12-28.

Kouba J (2009) A guide to using International GNSS Service (IGS) products. https://igscb.jpl.nasa.gov/igscb/resource/pubs/UsingIGSProductsVer21.pdf

Kouba J (2008) Implementation and testing of the gridded vienna mapping function 1 (vmf1). *Journal of Geodesy*, 82, 193-205.

Kleusberg A, Georgiadou Y, van den Heuvel F, Heroux P (1993) GPS data preprocessing with DIPOP 3.0. *Internal Technical Memorandum*, Department of Surveying Engineering, University of New Brunswick, Fredericton, NB, Canda, 1993.

Klobuchar J (1987) Ionospheric time-delay algorithm for single-frequency GPS users. *IEEE Transactions on aerospace and electronic systems*, (3), 325-331.

Lachapelle G, Gratton P, Horrelt J, Lemieux E, Broumandan A (2018) Evaluation of a low cost hand held unit with GNSS raw data capability and comparison with an android smartphone. *Sensors*, 18, 4185.

Langley R, Teunissen P, Montenbruck O (2017) Ionosphere Monitoring. In: Teunissen PJG, Montenbruck O (eds) *Springer Handbook of Global Navigation Satellite Systems*. Springer International Publishing, 3-24.

Laurichesse D, Rouch C, Marmet F, Pascaud M (2017) Smartphone applications for precise point positioning. *Proc. ION GNSS 2017*, Institute of Navigation, Portland, Oregon, September 25-29, 171-187

Laurichesse D, Mercier F, Berthias J, Broca P, Cerri L (2009) Integer ambiguity resolution on undifferenced GPS phase measurements and its application to PPP and satellite precise orbit determination. *Navigation*, 56, 2, 135-149.

Li X, Wang H, Li X, Li L, Lv H, Shen Z, Xia C, Gou H (2022a) PPP rapid ambiguity resolution using Android GNSS raw measurements with a low-cost helical antenna. *J Geodesy*, 96, 65. https://doi.org/10.1007/s00190-022-01661-6

Li Y, Cai C, Xu Z (2022b) A Combined Elevation Angle and C/N0 Weighting Method for GNSS PPP on Xiaomi MI8 Smartphones. *Sensors*, 22(7): 2804.

Li B, Miao W, Chen G, Li Z (2022c) Ambiguity resolution for smartphone GNSS precise positioning: effect factors and performance. *Journal of Geodes*y, 96(9), 63.

Li G, Geng J (2019) Characteristics of raw multi-GNSS measurement error from Google Android smart devices. *GPS Solutions*, 23, 1-16.

Li P, Zhang X (2015) Precise point positioning with partial ambiguity fixing. *Sensors*, 15, 6, 13627-13643.

Lichtenegger H, Hofmann-Wellenhof B (1990) GPS-data preprocessing for cycle-slip detection. *In Global Positioning System: An Overview*. Springer: Berlin/Heidelberg, Germany, 57-68.

Liu W, Shi X, Zhu F, Tao X, Wang F (2019) Quality analysis of multi-GNSS raw observations and a velocity-aided positioning approach based on smartphones. *Adv. Space Res*. 2019, 63, 2358-2377

Malkos S (2016) User location takes center stage in new Android OS: Google to provide raw GNSS measurements. *GPS World*, 27, 36, https://www.gpsworld.com/google-to-provide-raw-gnss-measurements/.

Miao W, Li B, Gao Y (2022) The superiority of multi-GNSS L5/E5a/B2a frequency signals in smartphones: stochastic modeling, ambiguity resolution, and RTK positioning. *IEEE Internet of Things Journal*,10 (8): 7315-7326. DOI:10.1109/JIOT.2022.3228769

Miao Y, Sun Z, Wu S (2011) Error analysis and cycle-slip detection research on satellite-borne GPS observation. *J. Aerosp. Eng*, 24, 95-101, doi:10.1061/(ASCE)AS.1943-5525.0000056.

Montenbruck O, Steigenberger P, Hauschild A (2018) Multi-GNSS signal-in-space range error assessment–Methodology and results. *Advances in Space Research*, 61(12), 3020-3038

Niell A. E. (1996) Global mapping functions for the atmosphere delay at radio wavelengths. *Journal of Geophysical Research Atmospheres*, 101(B2), 3227-3246.

Odolinski R, Teunissen P (2020) Best integer equivariant estimation: Performance analysis using real data collected by low-cost, single-and dual-frequency, multi-GNSS receivers for short-to long-baseline RTK positioning. *Journal of Geodesy*, 94, 9, 91.

Odijk D, Verhagen S (2007) Recursive detection, identification and adaptation of model errors for reliable high-precision GNSS positioning and attitude determination. *In 2007 3rd International Conference on Recent Advances in Space Technologies* (pp. 624-629). IEEE.

Paziewski J (2020) Recent advances and perspectives for positioning and applications with smartphone GNSS observations. *Meas. Sci. Technol*. 2020, 31, 091001.

Paziewski J, Sieradzki R, Baryla R (2019) Signal characterization and assessment of code GNSS positioning with low-power consumption smartphones. *GPS Solut*. 2019, 23, 98.

Paziewski J, Pugliano G, Robustelli U (2020) Performance assessment of GNSS single point positioning with recent smartphones. *In IMEKO TC-19 International Workshop on Metrology for the Sea*. Naples, Italy.

Pichler M, Bodenhofer U, Schwinger W (2004) Context-awareness and artificial intelligence. *In OGAI Journal (Oesterreichische Gesellschaft fuer Artificial Intelligence)*, 23(1).

Realini E, Caldera S, Pertusini L, Sampietro D (2017) Precise GNSS positioning using smart devices. *Sensors*, 17, 2434.

Riley S, Lentz W, Clare A (2017) On the path to precision-observations with android GNSS observables. *Proc. ION GNSS 2017*, Institute of Navigation, Portland, Oregon, September 25-29, 116-129.

Robustelli U, Baiocchi V, Pugliano G (2019) Assessment of dual frequency GNSS observations from a Xiaomi Mi 8 Android smartphone and positioning performance analysis. *Electronics*, 8(1), 91.

Robustelli U, Pugliano G (2019) Code multipath analysis of Galileo FOC satellites by time-frequency representation. *Appl. Geomat*. 2019, 11, 69-80.

Schmid R, Rothacher M, Thaller D, Steigenberger P (2005) Absolute phase center corrections of satellite and receiver antennas: Impact on global GPS solutions and estimation of azimuthal phase center variations of the satellite antenna. *GPS solutions*, 9, 283-293.

Seepersad G, Hu J, Yang S, Yi D, Bisnath S (2021) Changing Lanes with Smartphones Technology. *Proc. ION GNSS 2021*, Institute of Navigation, St. Louis, Missouri, USA, 20-24 Sept, pp 3021-3036.

Seepersad G, Hu J, Yang S, Yi D, Bisnath S (2022) Performance Assessment of Tightly Coupled Smartphone Sensors with Legacy and State Space Corrections. *Proc. ION GNSS 2022*, Institute of Navigation, Denver, Colorado, USA, 19-23 Sept, pp 2235-2255.

Shinghal G, Bisnath S (2021) Conditioning and PPP processing of smartphone GNSS measurements in realistic environments. *Satellite Navigation*, 2, 10. https://doi.org/10.1186/s43020-021-00042-2

Sikirica N, Malić E, Rumora I, Filjar R (2017) Exploitation of Google GNSS measurement API for risk assessment of GNSS applications. *In 2017 25th Telecommunication Forum* (TELFOR) (pp. 1-3). IEEE.

Sui M, Gong C, Shen F (2022) An optimized stochastic model for smartphone GNSS positioning. *Frontiers in Earth Science*, 10: 1018420.

Tao X, Liu W, Wang Y, Li Y, Zhu F, Zhang X (2023) Smartphone RTK positioning with multi-frequency and multi-constellation raw observations: GPS L1/L5, Galileo E1/E5a, BDS B1I/B1C/B2a. *J Geodesy* 97, 43. https://doi.org/10.1007/s00190-023-01731-3

Teunissen P (1995). The least-squares ambiguity decorrelation adjustment: a method for fast GPS integer ambiguity estimation. *Journal of Geodesy*, 70: 65-82.

Teunissen P (2003) Theory of integer equivariant estimation with application to GNSS. *J Geod* 77(7-8):402-410. https://doi.org/10.1007/s00190-003-0344-3

Teunissen P (1998) Success probability of integer GPS ambiguity rounding and bootstrapping. *Journal of Geodesy*, 72 (1998): 606-612.

Teunissen P (2017) Batch and recursive model validation. In: Teunissen PJG, Montenbruck O (eds) *Springer Handbook of Global Navigation Satellite Systems*, 687-720.

Thomas H and Norbert J (2017) Atmospheric signal propagation. In: Teunissen PJG, Montenbruck O (eds) *Springer Handbook of Global Navigation Satellite Systems*. Springer International Publishing, 3-24.

Wang L, Li Z, Wang N, Wang Z (2021) Real-time GNSS Precise Point Positioning for Low-Cost Smart Devices. *GPS Solutions* 25, 69. https://doi.org/10.1007/s10291-021-01106-1

Wang J, Zheng F, Hu Y, Zhang D, Shi C (2023) Instantaneous Sub-meter Level Precise Point Positioning of Low-Cost Smartphones. *Navigation*, 70(4).

Wen Q, Geng J, Li G, Guo J (2020) Precise point positioning with ambiguity resolution using an external survey-grade antenna enhanced dual-frequency android GNSS data. *Measurement*, 2020, 157, 107634.

Wanninger L, Heßelbarth A (2020) GNSS code and carrier phase observations of a Huawei P30 smartphone: Quality assessment and centimeter-accurate positioning. *GPS Solutions*, 24(2), 64.

Wieser A, Brunner F K (2000) An extended weight model for GPS phase observations. *Earth, Planets and Space*, 52(10): 777-782.

Wu Q, Sun M, Zhou C et al (2019) Precise point positioning using dual-frequency GNSS observations on smartphone. *Sensors* 19(9):1-17

Wu J, Wu S, Hajj G, Bertiger W, Lichten S (1993) Effects of antenna orientation on GPS carrier phase. *Manuscr Geod*, 18(2):91–98

Wübbena T, Darugna F, Ito A, Wübbena J (2018) Geo++'s Experiments on Android GNSS Raw Data. *GNSS Raw Measurements Taskforce Workshop*, GSA Headquarters, 30th May 2018, Prague.

Xu P, Ng H F, Zhong Y, Zhang G, Wen W (2023) Differentiable Factor Graph Optimization with Intelligent Covariance Adaptation for Accurate Smartphone Positioning. *Proc. ION GNSS 2023*, Institute of Navigation, Denver, Colorado, USA, September 11-15, 2765-2773.

Xu X, Nie Z, Wang Z, Zhang Y (2020) A modified TurboEdit cycle-slip detection and correction method for dual-frequency smartphone GNSS observation. *Sensors*, 2020, 20, 5756.

Yang Y, Zhou F, Song S (2024) Improving precise point positioning (PPP) performance with best integer equivariant (BIE) estimator. *GPS Solutions*, 28.1: 50.

Yi D, Hu J, Bisnath S (2024) Improving PPP smartphone processing with adaptive quality control method in obstructed environments when carrier-phase measurements are missing. *GPS Solutions*, 28, 56. https://doi.org/10.1007/s10291-023-01596-1.

Yi D, Bisnath S, Naciri N, Vana S (2021) Effects of ionospheric constraints in Precise Point Positioning processing of geodetic, low-cost and smartphone GNSS measurements. *Measurement*, 183, 109887. 10.1016/j.measurement.2021.109887

Yong C, Harima K, Rubinov E, McClusky S, Odolinski R (2022) Instantaneous best integer equivariant position estimation using Google Pixel 4 smartphones for single-and dual-frequency, multi-GNSS short-baseline RTK. *Sensors*, 22.10: 3772.

Zumberge J, Heflin M, Jefferson D, Watkins M, Webb F (1997) Precise point positioning for the efficient and robust analysis of GPS data from large networks. *Journal of Geophysical Research: Solid Earth*, 1997,102(B3):5005-5017.

Zangenehnejad F, Gao Y (2021) GNSS smartphones positioning: advances, challenges, opportunities, and future perspectives. *Satellite Navigation*, 2(1), 24. https://doi.org/10.1186/ s43020-021-00054-y

Zangenehnejad F, Jiang Y, Gao Y (2022) Improving Smartphone PPP and RTK Performance Using Time-Differenced Carrier Phase Observations. *Proc. ION GNSS 2022*, Institute of Navigation, Denver, Colorado, USA, September 19-23, 2287-2300.

Zhang X, Tao X, Zhu F, Shi X, Wang F (2018a) Quality assessment of GNSS observations from an Android N smartphone and positioning performance analysis using time-differenced filtering approach. *GPS Solutions*, 22(3), 70. http://dx.doi.org/10.1007/s10291-018-0736-8

Zhang X, Li P (2016) Benefits of the third frequency signal on cycle slip correction. *GPS solutions*, 20: 451-460.

Zhang K, Jiao F, Li J (2018b) The assessment of GNSS measurements from android smartphones. *In Proceedings of the China Satellite Navigation Conference*, Harbin, China, 23-25 May 2018; Springer: Singapore, 2018, 147-157.

Zhou F, Dong D, Li W, Jiang X, Wickert J, Schuh H (2018) GAMP: An open-source software of multi-GNSS precise point positioning using undifferenced and uncombined observations. *GPS Solutions*, 22, 33.

Zheng K, Zhang X, Li P, Li X, Ge M (2019) Multipath extraction and mitigation for high-rate multi-GNSS precise point positioning. *Journal of Geodesy*, 93, 2037–2051 (2019).